UNIVERSIDADE DE LISBOA
FACULDADE DE CIÊNCIAS
DEPARTAMENTO DE ENGENHARIA GEOGRÁFICA, GEOFÍSICA E DE ENERGIA

Development of a sample holder for electrochemical capacitance-voltage dopant profiling in silicon wafers

Ricardo Miguel Couto Soares Vareiro

Mestrado Integrado em Engenharia da Energia e Ambiente

Dissertação orientada por:
Professor Doutor Killian Lobato (FCUL)
Doutor Guilherme Gaspar (FCUL)

2020

− BLANK PAGE −
− PÁGINA EM BRANCO −

Acknowledgement

First, to my advisors Professor Killian Lobato and Doctor Guilherme Gaspar, for the amazing opportunity, the trust, dedication, and availability, without whom this dissertation would not be possible.

To all the members of the S-LoTTuSS research project, for all the time and support, especially Afonso Guerra, whose help was invaluable.

To Doctor Hadi Esmeailsabzali, Doctor Ivo Costa and Barrel Technologies, for the information made available.

To my family, especially my parents and brothers, for all the support in the last 26 years.

To Raquel Samuel, for always being by my side.

To all my friends who shared the adventure of University education with me. Rafael Palma, Cláudia Gomes, Ana Antunes, Frederico Matos, Jhon Ramos, Bianca Lage, Carlos Alves, Paulo Fernandes, Rita Costa, Carolina Gonçalves, Pedro Cecília and Beatriz Abrantes for everything, be it in good or bad times.

Lastly, but not less important, to all the UL community, from the youngest freshmen to the oldest employee, for the acceptance.

This dissertation was supported by the S-LoTTuSS project through the grant agreement PTDC/CTM-CTM/28962/2017, financed by national funds FCT/MCTES (PIDDAC).

Abstract

By creating a tandem solar cell, it is theoretically possible to almost double the solar cell's power conversion efficiency. The current most promising materials for the tandem solar cells are crystalline silicon for the bottom cell and perovskite for the top cell. Perovskite is an ideal material for the top cell, due to its wide, tuneable bandgap and low level of parasitic absorption.
To create tandem solar cells, the two sub-cells must be connected through a layer. One such layer is the tunnel junction. The recombination layer generated by the tunnel junction provokes an alignment of the valence and conduction bands of the two sub-cells, allowing the transfer of electrons from one sub-cell to another, with no variation of the energy of the electron. To create the tunnel junction, the doping of the layers must be very high in a very narrow depth, and with different signs, meaning that one cell must be n-type while the other must be p-type.
To guarantee a functioning tunnel junction, the doping profile must be carefully controlled and characterized.
The dopant profiling can be done through the Electrochemical Capacitance-Voltage (ECV). The ECV technique measures the electrically active charge carriers in the surface of the wafer, alternating the measurements with the etching of the surface, to reach bigger depths.
Therefore, the objective of this dissertation is the development of an ECV system, through the use of the AutoCAD® computer-assisted design software. The proposed system design has four main parts: the electrochemical cell, the vacuum chuck, the piston, and the chamber. The electrochemical cell consists of a PTFE reservoir, where an electrolyte will be introduced. This electrolyte permits the measurement and etching of the silicon wafers. The cell has orifices for light, waste and input electrolyte reservoirs, electrical electrodes, pump, and sample contact. The vacuum chuck is used to keep the sample in place during the measurements by the action of vacuum. The piston serves as a holder for the vacuum chuck, so the measurements can be done in the vertical position. Finally, the chamber is used to house all the different reservoirs connected to the electrochemical cell.

Keywords: Electrochemical Capacitance-Voltage, Tunnel Junctions, AutoCAD

Resumo

Devido ao baixo custo da tecnologia fotovoltaica, é necessário aumentar a sua eficiência. Uma maneira de cumprir este objetivo é através da introdução de impurezas nas bolachas de silício que melhoram as suas características elétricas, denominado por dopagem. Através da dopagem das bolachas de silício, a conversão de energia é facilitada, sendo necessário menos energia luminosa para excitar um eletrão.
Outra maneira de aumentar a eficiência de células solares, é unir duas células com características diferentes, criando uma célula solar *tandem*. A criação de células solares *tandem* aumentou a eficiência de células solares até quase o dobro de uma célula solar com apenas uma junção. Os materiais mais comuns para células solares *tandem* são silício cristalino para a célula inferior e perovskita para a célula superior. Perovskita é um material ideal para este tipo de utilização devido ao seu hiato de banda variável e a sua baixa absorção parasita.
Para criar uma célula *tandem* é necessária uma camada que liga ambas as sub-células. Um exemplo para esta camada é a junção de efeito túnel. Este tipo de junção cria uma camada de recombinação que provoca o alinhamento das bandas de valência e de condução das sub-células. Este alinhamento permite a transferência de eletrões de uma camada para outra sem variação da energia do eletrão. Para criar as junções de túnel, a dopagem presente nas sub-células tem de ser muito elevada, numa camada muito fina da célula, com símbolos diferentes, ou seja, uma célula tem de ser de tipo N, enquanto a outra tem de ser do tipo P.
Para garantir que a dopagem das células permite a formação de uma camada de túnel, a criação de perfis de dopagem das células é recomendada.
A criação de perfis de dopagem pode ser feita através da técnica de Capacitância-Tensão Eletroquímica (ECV). A técnica ECV mede os portadores de cargas eletricamente ativas à superfície da bolacha de silício, alternando as medições com a dissolução da superfície da bolacha, de modo serem feitas medições em profundidades maiores.
Portanto, esta dissertação tem como objetivo o desenvolvimento de um sistema ECV, assistido com o programa de desenho assistido por computador AutoCAD.
O sistema ECV projetado tem quatro partes principais: a célula eletroquímica, um sistema de vácuo, o pistão e a câmara.
A célula eletroquímica consiste num reservatório onde vai ser introduzido um eletrólito. Este eletrólito permite a medição e dissolução das bolachas de silício, sendo que o eletrólito mais comum contém na sua constituição ácido fluorídrico (HF). Este ácido é extremamente nocivo para a saúde humana. Deste modo, a célula é constituída em PTFE. A célula tem orifícios para luz, reservatórios para introdução do eletrólito novo e para retirar o eletrólito usado, para elétrodos elétricos, bomba e contacto com a amostra.
O orifício de luz é necessário para amostras de tipo N, devido à necessidade de cargas positivas para a dissolução química. Na técnica de ECV são necessários três elétrodos, um de carbono, um de calomelanos saturados e um de platina. O elétrodo de carbono é utilizado para o controlo da dissolução química e de medição, através de uma corrente DC. O elétrodo de calomelanos saturados é utilizado como referência para o sobrepotencial para a medição. O elétrodo de platina é utilizado para fazer as medições e para diminuir a impedância do eletrólito. Serve também para alternar entre medições e a dissolução química através de uma corrente AC. A bomba tem como objetivo a remoção de bolhas de hidrogénio que se formam durante a dissolução química. O hidrogénio formado provoca uma diminuição na velocidade do desbastamento devido à baixa concentração de eletrólito no local. No contacto para a amostra existe um o-ring que delimita a área de medição da amostra. Para que o o-ring suporte o ataque químico do HF, pode ser constituído de PTFE ou PVC.
O sistema de vácuo é utilizado para manter a amostra estável durante as medições, através do efeito de vácuo. O sistema de vácuo foi projetado de modo a ser compatível com amostras de diferentes tamanhos.

Para este propósito, o sistema de vácuo contém quatro canais de vácuo os quais podem ser abertos ou fechados de acordo com a necessidade. Para amostras mais pequenas, apenas os canais interiores são abertos, por outro lado, se as amostras são de maior dimensão, os canais mais exteriores podem ser abertos, desde que a amostra suporte estes canais.
O pistão serve de suporte para o sistema de vácuo, de modo que as medições sejam feitas na vertical. Consiste em uma haste vertical, suportada por um pé, onde o sistema de vácuo é acoplado. No local onde é colocado o sistema de vácuo, existe uma ranhura para ser colocada uma mola, que tem a função de comprimir o o-ring da célula eletroquímica de forma uniforme e constante ao longo de várias medições.
Finalmente, a câmara tem a função de alojar os vários reservatórios que estão ligados à célula eletroquímica. Durante as medições o reservatório de remoção de eletrólito encontra-se fechado com uma válvula e o de introdução encontra-se abertos. É espectável que no fim das medições, o reservatório de introdução é fechado e o de remoção aberto, de modo a remover todo o eletrólito que foi utilizado durante as medições. Este eletrólito foi contaminado através das reações químicas que ocorreram durante a dissolução química que ocorreu durante o procedimento.

Palavras-chave: Capacitância-tensão Electroquímica, Junções de Túnel, AutoCAD

Contents

Table of Figures

Table of Tables

Abbreviations and Acronyms

AC	Alternating Current
BIPV	Building Integrated Photovoltaics
C	Carbon
DC	Direct Current
ECV	Electrochemical Capacitance-Voltage
GILD	Gas Immersion Laser Doping
HIT	Heterojunction with Intrinsic Thin Layer
IR	Infra-Red
PCE	Power Conversion Efficiency
Pt	Platinum
PTFE	Polytetrafluoroethylene
SCE	Saturated Calomel Electrode
SIMS	Secondary Ion Mass Spectroscopy
UV	Ultraviolet

List of Symbols

A	Area (cm^2)
C	Capacitance (F)
E_c	Energy of the conduction band (eV)
E_F	Fermi level (eV)
E_r	Etch Rate (nm/s)
E_v	Energy of the valence band (eV)
F	Faraday's constant ($9.64x10^4$ C)
I	Current (A)
M	Molecular weight (g)
n	Net donor concentration (cm^{-3})
N	Number of charged carriers (cm^{-3})
q	Electronic charge (C)
V_i	Contact potencial difference (V)
V_s	Band bending of the semiconductor
W_d	Width of the depletion layer (nm)
W_r	Thickness of the material removed by dissolution (nm)
ε	Relative Permittivity of the semiconductor
ε_0	Permittivity of free space
ρ	Density of the semiconductor (g/cm^3)
Φ	Work function (eV)
χ	Electron affinity (eV)
Ψ	Barrier height potencial (V)

1. Objectives and Structure

1.1. Objectives

This dissertation is part of a research project called S-LoTTuSS (Scalable Low-cost Tandem Tunnel Junctions for Silicon Solar Cells). The project's goal is to develop scalable, low-cost tunnel junctions for tandem solar cells. The Gas Immersion Laser Doping (GILD) technique is used to create a tunnel junction by doping a very thin layer in the solar cell with high concentrations of boron. Later, the Electrochemical Capacitance-Voltage (ECV) technique is used to measure the doping profiles of the solar cell, with respect to the depth.

The dissertation has the objective of developing an ECV system through computer assisted technical design. The sampler consists of an electrochemical cell, electrodes, lamp, and wafer holder with vacuum chuck.

1.2. Structure

This dissertation will be structured in four chapters: Introduction, Doping Profiles Measurements, ECV System Design and Development and Conclusions.

The Introduction consists of the relevant information for the development of the dissertation. This is information about solar cells, including tandem solar cells, tunnel junctions and doping methods.

In the Doping Profiles Measurements, two doping profile measurement techniques are discussed, with higher emphasis in the ECV technique, since it is the technique focused.

In the ECV System Development chapter, the AutoCAD® designs for the low cost ECV measurement system is explained.

In the Conclusions section, some considerations about the dissertation are made while future work will be discussed.

2. Introduction

The development of the photovoltaic technology in the last decades lowered its costs to competitive levels. Therefore, the best way to develop the technology is to increase the efficiency. According to Shockley and Queisser [1], in 1961, the upper theoretical limit of efficiency for a silicon cell with a bandgap of 1.1 electro-volt (eV) is 30%. This limit was later revised by Richter *et al* [2], resulting in an Auger recombination limited efficiency of 29.43%, for a 110 µm thick solar cell.

Solar cell technology is based on the photovoltaic effect, discovered by Edmond Becquerel, in 1839. He discovered that the conductance increased with illumination, during an experiment using metal electrodes and electrolytes. When a semiconducting material is exposed to light, a photon is absorbed by an electron which gets excited, separating it from the atom, resulting in a free charge carriers in the conduction and valence bands.

Solar cells are devices that, when exposed to light, vary their current, voltage and resistance. The maximum power of the solar cell can be accessed by its fill factor (FF). This parameter is characterized by the short circuit current (I_{sc}), the open circuit voltage (V_{oc}) and the maximum power current and voltage (I_{mp} and V_{mp}), through the equation:

$$FF = \frac{V_{\mathrm{mp}} I_{\mathrm{mp}}}{V_{\mathrm{oc}} I_{\mathrm{sc}}} \tag{1}$$

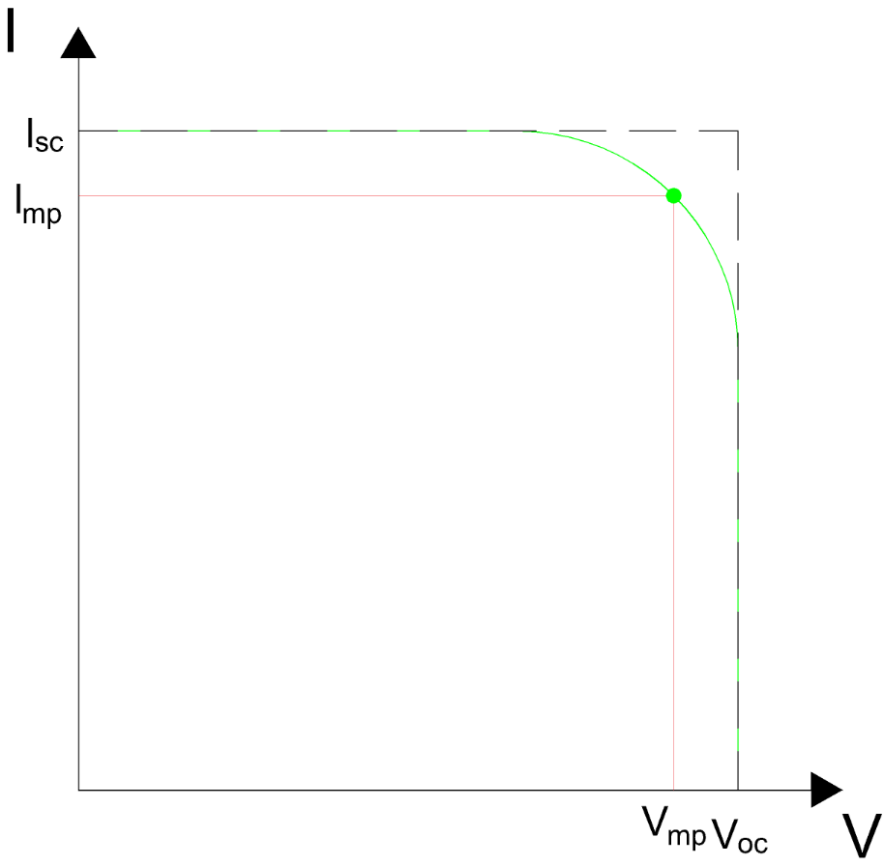

Figure 2.1 - Typical IV curve of a solar cell. The green point represents the maximum power point.

The I_{sc} and V_{oc} are the maximum current and voltage of the solar cell. The I_{mp} and V_{mp} are the current and voltage of the cell when its power is maximum, respectively. The closer the I_{mp} and V_{mp} are to I_{sc} and V_{oc} the bigger the FF is. Therefore, the solar cell performance is higher. This can be seen in Figure 2.1.

For the solar cell to produce electrical energy it must absorb energy from photons. If the electrons in the valence band, called valence electrons, absorb energy superior to the semiconductor's bandgap energy, then the electrons move to the conduction band [3]. In Figure 2.2, the band diagram of a semiconductor is represented. The dashed line corresponds to the Fermi Level. The Fermi Level represents a hypothetical energy level of an electron where there is 50% probability that this level is occupied. If the energy from the absorbed photon is higher than the semiconductor's bandgap, the extra energy is lost through thermalization. On the other hand, photons with less energy are not absorbed.

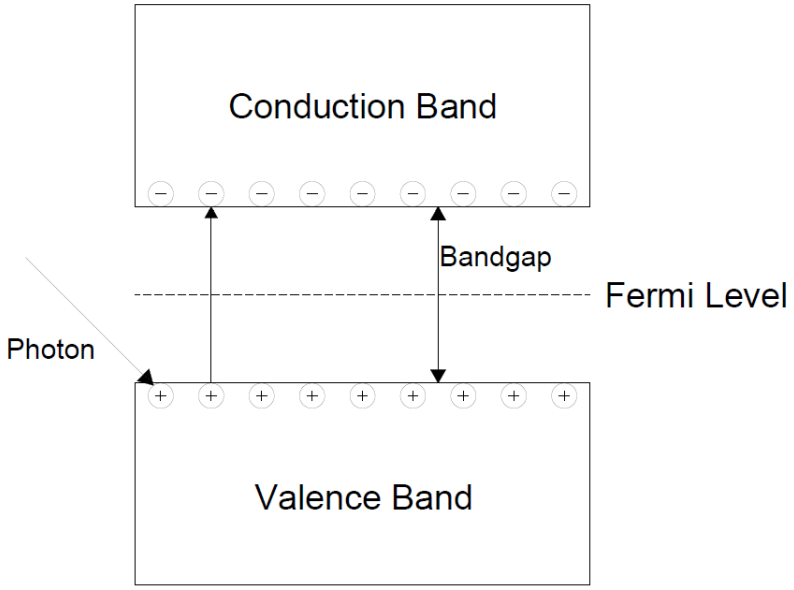

Figure 2.2 - Band diagram of a semiconductor. The dashed line corresponds to the Fermi Level. The bandgap is the necessary energy for the promotion of the electron to the conduction band from the valence band. The vertical one-sided arrow corresponds to the excitation of the electron from the valence band to the conduction band when absorbing photons.

2.1. Solar Cells

The American Society for Testing and Materials defined a terrestrial spectral irradiance distribution, called AM 1.5G. This distribution considers the direct sunlight and the scattered light from the atmosphere. For the AM 1.5G distribution, the best semiconductor bandgap is of 1.34 eV [4]. The most used material for photovoltaic systems is crystalline silicon. Its bandgap is 1.12 eV, which makes it an almost perfect candidate for single bandgap solar cells.

The most used material for photovoltaic applications, in 2019, was mono-crystalline silicon [5]. There are other types of cells which use different materials. Amorphous silicon is an example, although it is not as efficient, reaching around 10.2% efficiency. These cells, although less efficient, have a lower cost [6]. Another type is multi-crystalline silicon cells with a lower efficiency than the mono-crystalline silicon, but higher than the amorphous silicon.

Nowadays, 90% of the solar cells are single-junction silicon cells [7]. These have a simple architecture, being formed by two layers of the same material, but with different doping, to create the p-n junction [8]. An example of this type of solar is presented in Figure 2.3.

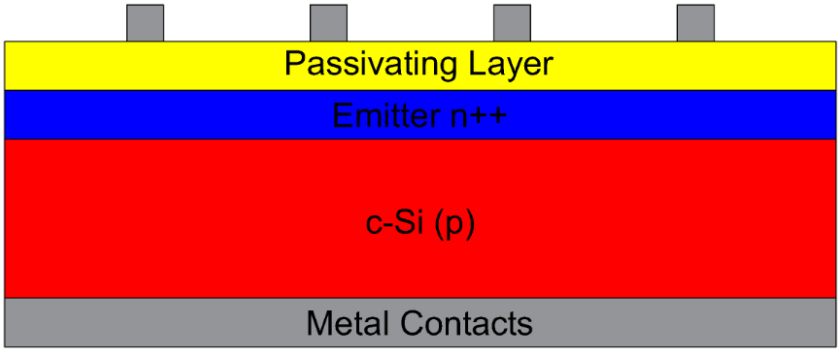

Figure 2.3 - Example of an homojunction solar cell. It has a p-doped crystalline silicon layer, a heavily doped n-type emitter, a passivating layer and metal contacts on the back.

Another type of solar cell is the heterojunction solar cell. This cell has different semiconductors forming the p-n junction. It can be formed, for example, by a layer of crystalline silicon between two layers of amorphous silicon. These types of cells obtain higher open-circuit voltages when compared with homojunction solar cells. Nevertheless, the interface between the layers of amorphous silicon and crystalline silicon have a high density of defects, which reduce the performance of the solar cell [9]. A schematic example of a heterojunction solar cell is presented in Figure 2.4.

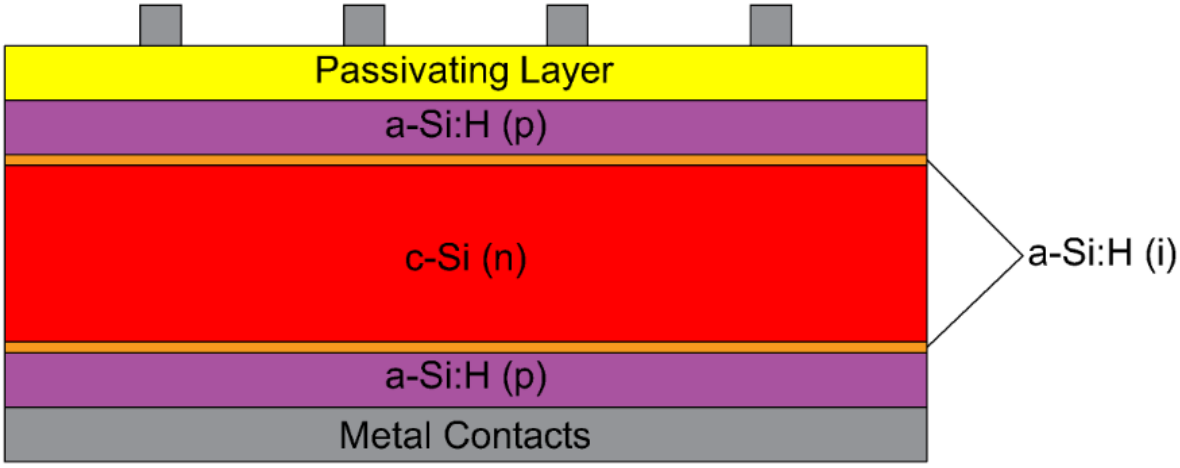

Figure 2.4 - Example of a heterojunction solar cell. It contains a n-doped crystalline silicon layer, interfacing with two hydrogenated amorphous silicon thin films. It also has two p-doped hydrogenated amorphous silicon layers.

One way to increase the efficiency of solar cell is by stacking another solar cell on top of the silicon cell. This type of solar cell is a tandem solar cell. The two different solar cell present different characteristics, meaning that they absorb different parts of the solar spectrum [10].

Tandem Solar Cells

A tandem solar cell consists of stacking different solar cells on top of each other. By stacking the solar cells, a broader spectrum of light can be absorbed. The top cell has a wider bandgap; therefore, it absorbs higher energy photons, leaving the lower energy photons undisturbed. The bottom cell has a lower bandgap and absorbs lower energy photons. This allows for a wider spectrum of light to be absorbed, and the loss of energy through thermalization to be lessened.

Depending on the way the tandem solar cell is fabricated it can have three different architectures, monolithically integrated, mechanically stacked and spectral splitting [11]. The monolithic solar cell is produced by growing the top sub-cell directly on the bottom sub-cell, with a recombination layer connecting the two. The mechanically stacked is a solar cell where the two sub-cells are created separately and then connected. Finally, the spectral splitting, where the two cells are apart from each other. They use an optical system to split the solar spectrum, so that the correct energy photons reach the adequate sub-cell.

A monolithic tandem solar cell consists of a solar cell where two sub-cells are processed directly one on top of the other. For a two-terminal solar cell they are electrically connected in series through a recombination contact. The connection allows for the electrons that are generated on the n-type sub-cell to pass to the p-type sub-cell, or the inverse if the doping is inverted. If this is achieved, the photocurrent (current induced by the absorption of light) of both sub-cells should be the same. If not, then the overall tandem current is the same as the limiting sub-cell, and the Power Conversion Efficiency (PCE) of the cell diminishes [12]. An example of these cells is in Figure 2.5.

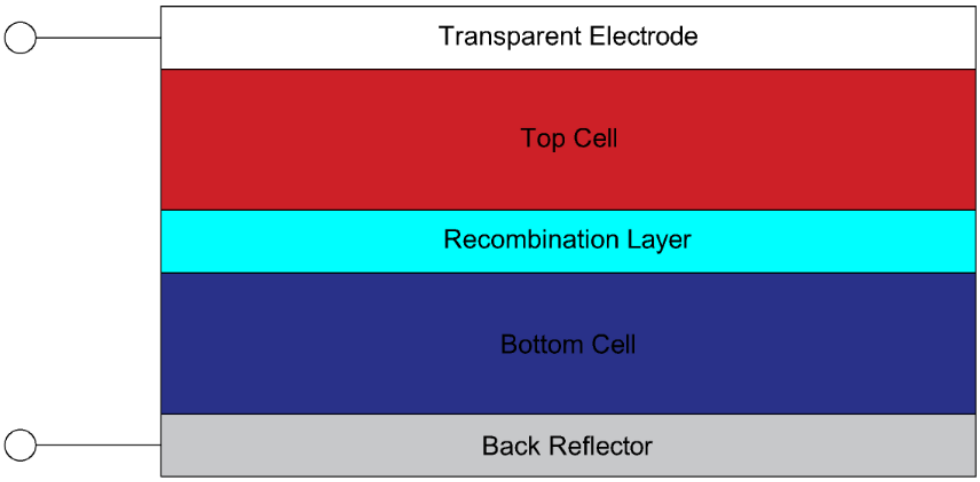

Figure 2.5 - Two terminal solar cell. It consists in a top cell on top of a bottom cell, connected through a recombination layer. It is used in monolithically integrated solar cells.

One of the materials that can be used for the top cell is perovskite. Perovskite is an organic-inorganic lead halide. Although it is recent technology, it has seen a rapidly increase in its efficiency, from around 4% to 22% in about 7 years[13]. It has excellent charge-carrier transport, wide, tuneable bandgap from 1.2 to 2.2 eV and low level of parasitic absorption, making it an almost ideal material for the top -sub cell in tandem solar cells [13]. Nevertheless, some problems exist with perovskite, including the decomposition of the perovskite due to moisture and the shorter lifetime when compared to other solar cells [14]. The bottom sub-cell can be silicon, or another material.

A tandem solar cell can achieve a theoretical maximum efficiency of 68.2% for an infinite number of solar cells, at 1 sun illumination. For a tandem solar cell with two solar cells, where the top cell has a bandgap of 1.9 eV and the bottom cell has a bandgap of 1.0 eV, the theoretical efficiency is 42.3%. [15] For a tandem cell with a perovskite top cell and a Si bottom cell, the theoretical efficiency is 35% [16]. An efficiency of 27.6% was recently achieved for a single junction solar cell under one sun illumination [17], meaning that the tandem cell with two sub-cells almost doubles this efficiency.

2.2. Doping

The efficiency of an individual solar cell can be increased by the process of doping. In this process, elements with different number of valence electrons are introduced in the semiconductor. By introducing dopants in the crystalline wafer, its atomic structure changes, existing more electron donors for n-type dopants or less electrons acceptors for p-type dopants. This structure change is displayed in Figure 2.6.

The most used dopants are boron, as a p-type dopant, and phosphorus, as a n-type dopant, for silicon wafers. By using a n-type dopant, the Fermi level approaches the conduction band, while for p-type doping, the Fermi level is closer to the valence band. The approximation of the Fermi level depending on the type of dopant used can be seen in Figure 2.7. The charges that contribute to the doping of the wafer are called electrically active charges, while the charges that do not contribute are called electrically inactive charges. One example of inactive charges are precipitates such as phosphorus silicate.

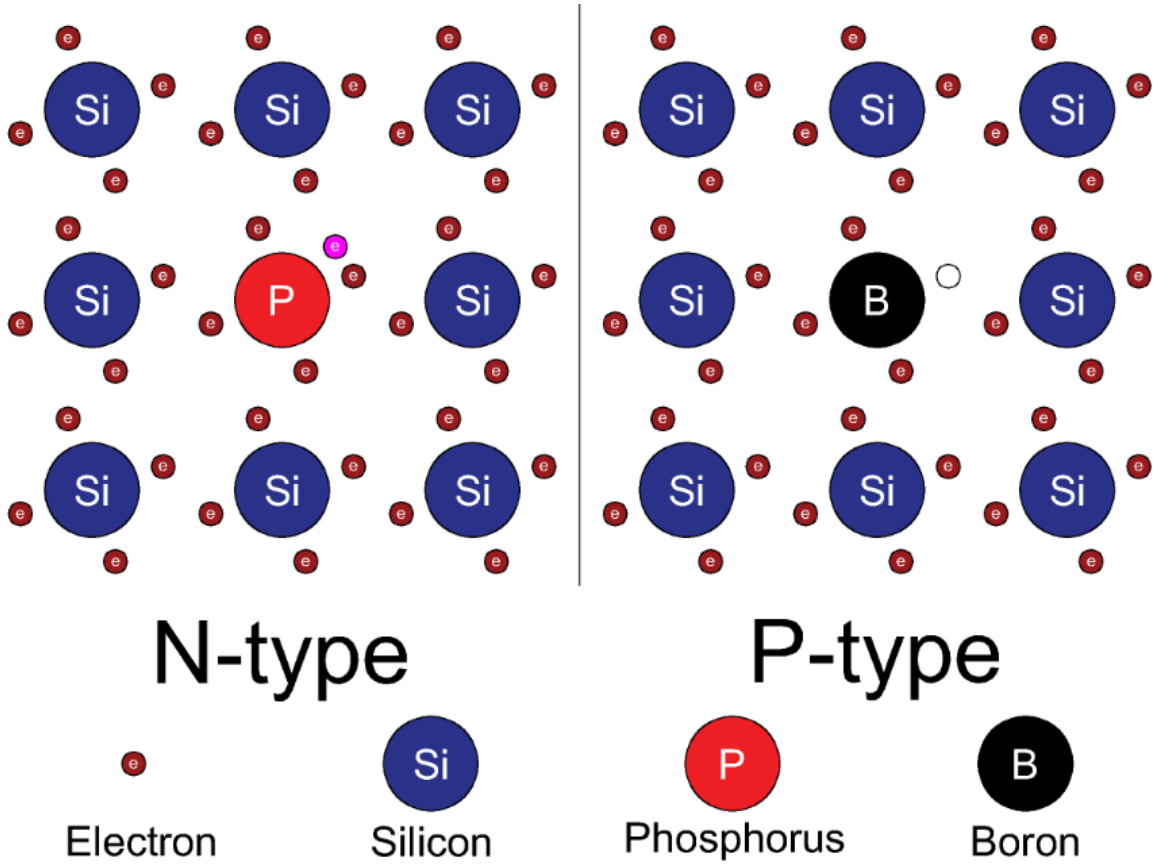

Figure 2.6 - Silicon atomic structure, with n-type doping and p-type doping. The phosphorus atom (in bright red) has an aditional electron (pink) compared to the silicon atom (dark blue), while the boron atom (black) has one more hole (white).

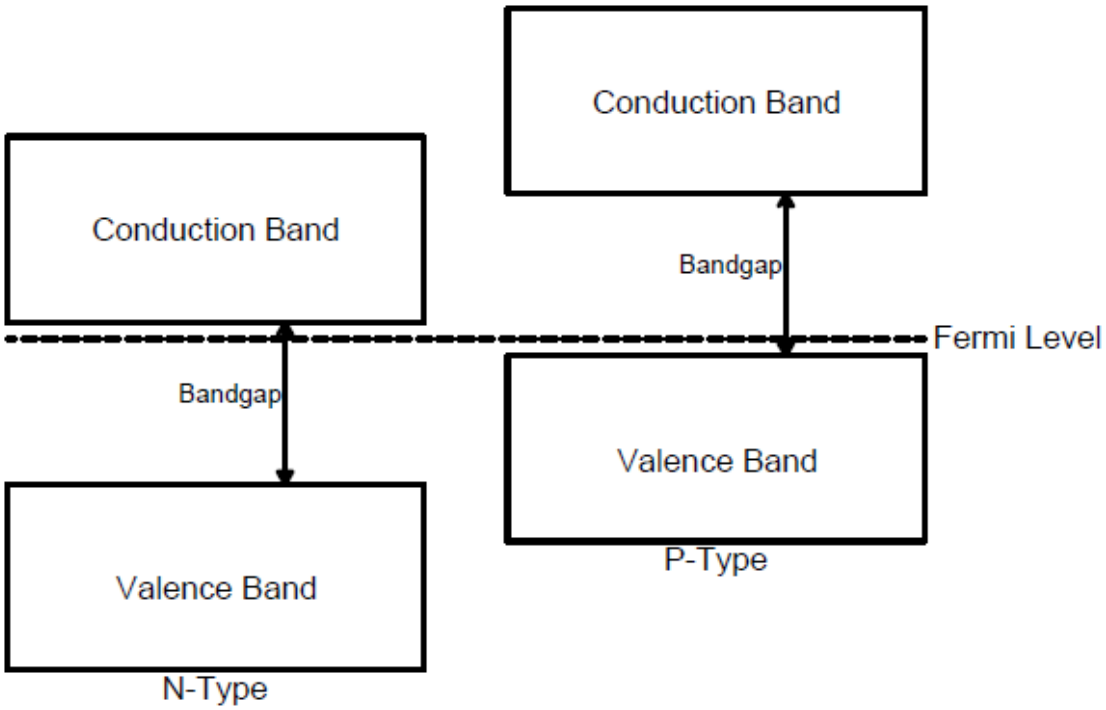

Figure 2.7 - Band diagram for (left) n-type and (right) p-type doped wafers. When a n-type dopant is used, the Fermi level is closer to the conduction band. On the other hand, the Fermi level is closer to the valence band, when p-type dopants are used.

Other ways to increase the efficiency of a solar cell, is through tandem cells and tunnel junctions. The tunnel junction creates a recombination layer where the bandgaps of the different cells align. This allows the electron to move from the conduction band of a sub-cell to the valence band of the other, without altering the electron's energy. These systems will be better explained further.

Nevertheless, some specific characteristics are necessary to use these techniques. One of these characteristics is a highly doped layer at the surface of the junction. The doping in this layer rapidly decreases in a few nanometres. These characteristics can be monitored through doping profiles.

2.3. Tunnel Junction

In tandem solar cells, a transparent and conductive layer is required to connect both sub-cells. The most common of these layers is tunnel junctions [18]. This type of structure occurs in degenerately doped p-n junctions [19]. Shown in the top of Figure 2.8 is a tunnel junction with no voltage being applied. When a small voltage which permits the natural flow of the current, called a forward bias voltage, is applied, it creates an alignment of the conduction band and the valence band, and in turn, a very narrow depletion layer. This layer is a region where the mobile carrier charges are removed by an electric field. When this alignment is present, an electron from the n-type conduction band can tunnel through the depletion layer into the p-type valence band without gaining or losing energy, since the bands are in the same energy level, as seen in the bottom part of Figure 2.8. This tunnelling effect is possible due to a small forward bias being applied and a very thin depletion layer. If the forward bias is increased, then the tunnel effect is no longer possible [20]. This motion is also possible due to the movement of the electrons. The electron does not have a linear motion, but it based in probabilistic events. When an electron moves, there is a probability that it will appear in a location around its initial position [21].

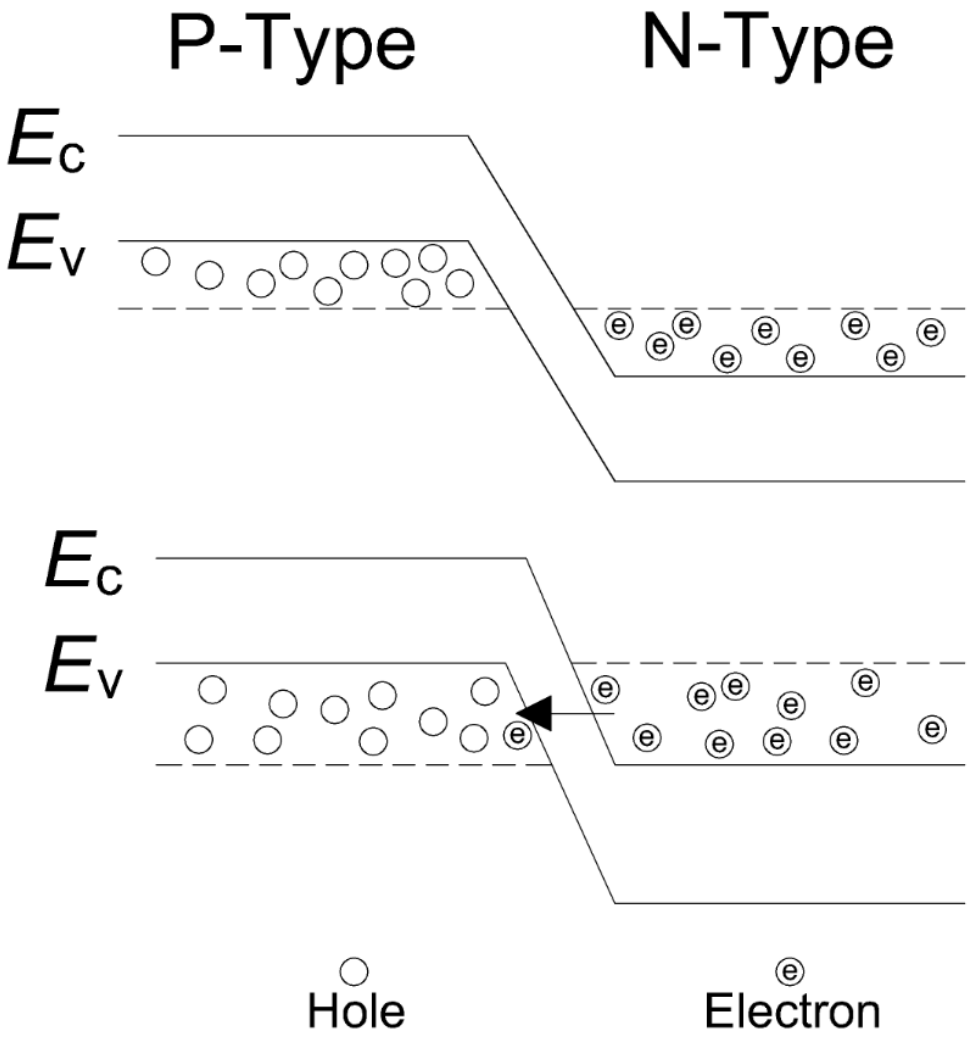

Figure 2.8 - Tunnel junction where no voltage is being applied (top), and with a voltage being applied (bottom). In the top junction, the valence and conduction bands are not alligned, and no electrons are moving through the depletion layer. In the bottom junction, the valence and conduction bands are aligned and electron can tunnel through the depletion layer from the conduction band to the valence band.

The tunnel junctions are created through highly doped layers, where the valence and conduction band align. To create these highly doped layers several techniques exist, among others, Thermal Diffusion or Gas Immersion Laser Doping (GILD) exist.

Thermal Diffusion

The Thermal Diffusion technique is used for wafer doping. It depends on various characteristics, of which the most important are the temperature and the gaseous environment. It is conducted in two steps: pre-deposition and drive-in.

Pre-deposition consists in the evaporation and deposition of the dopant over the surface of the wafer which forms a small depth junction with a high superficial concentration.

The drive-in is the introduction of the already doped wafer in a quartz tube. In this tube, the wafers will heat up and allow for a deeper junction to be formed, which promotes the formation of a deeper emitter with lower superficial dopant concentration. The wafer must be heated slowly or there can be high temperature gradients or deformation [22].

Gas Immersion Laser Doping

The research project has as objective the creation of low-cost tunnel junctions in tandem solar cells. For this purpose, the monolithic two-terminal tandem solar cell, with crystalline silicon as the bottom sub-cell, proves the most adept system. To build these solar cells, the creation of a tunnel junction is necessary. A technique that creates the highly doped p-n junctions needed for the tunnel junctions is the Gas Immersion Laser Doping (GILD). The project aims to create the tunnel junctions by doping silicon wafers with phosphorus, using $POCl_3$ as the gaseous dopant source.

In the GILD technique, a laser is used to incorporate large concentrations of dopants during the moments when the wafer's surface is fused. Depending on the characteristics of the laser, such as, the power and the number of pulses, the depth of the incorporation and the concentration of the active dopants is altered, respectively.

The GILD technique uses a low-pressure chamber, where the sample is placed in a platform that moves in two dimensions (x-y). The chamber has an inert atmosphere, where the dopant is continuously introduced, until the desired concentration is achieved. After the atmosphere reaches the desired characteristics, the laser is used. After each laser pulse, dopant can be injected in the chamber, to keep its concentration constant.

The most used dopants are boron and phosphorus. Their sources for GILD doping are BF_3, BCl_3 or B_2H_6 for boron and PCl_3 for phosphorus [21].

3. Doping Profiles Measurements

There are various techniques which can measure doping profiles, such as Secondary Ion Mass Spectroscopy (SIMS) and ECV.

3.1. SIMS

The Secondary Ion Mass Spectroscopy technique consists in an analysis technique for solid surfaces and thin films. Its basis is the sputtering concept. Sputtering consists in using an ion beam to bombard the surface of the wafer so that the ions composing the surface are ejected. These secondary ions are then analysed, and the composition of the wafer's surface is known. This technique can analyse any chemical element, distinguish isotopes, and has high depth resolution. Nevertheless, the high cost of production, its complexity and the target of its analysis makes this technique inappropriate for the objectives of this dissertation [23].

3.2. ECV

This method is based in the Capacitance-Voltage technique of doping profiling, in which the measurement is made by creating a metal-semiconductor junction, called a Schottky barrier. The Schottky barrier is created during the contact between the metal and the semiconductor. Before the contact is made (Figure 3.1) the semiconductor does not contain any charges at its surface. This means that the band diagram for the surface of the semiconductor is the same as the band diagram for the bulk of the semiconductor. The work function (defined as the amount of energy required by the electron to be raised from the Fermi level to the vacuum level, which is defined as the energy level of an electron just outside the metal with zero kinetic energy) of the metal (Φ_m) is constant, while the work function of the semiconductor (Φ_s) is variable with its doping. The electron affinity of the semiconductor (χ_s) is the energy difference between the vacuum level and the lower edge of the conduction band.

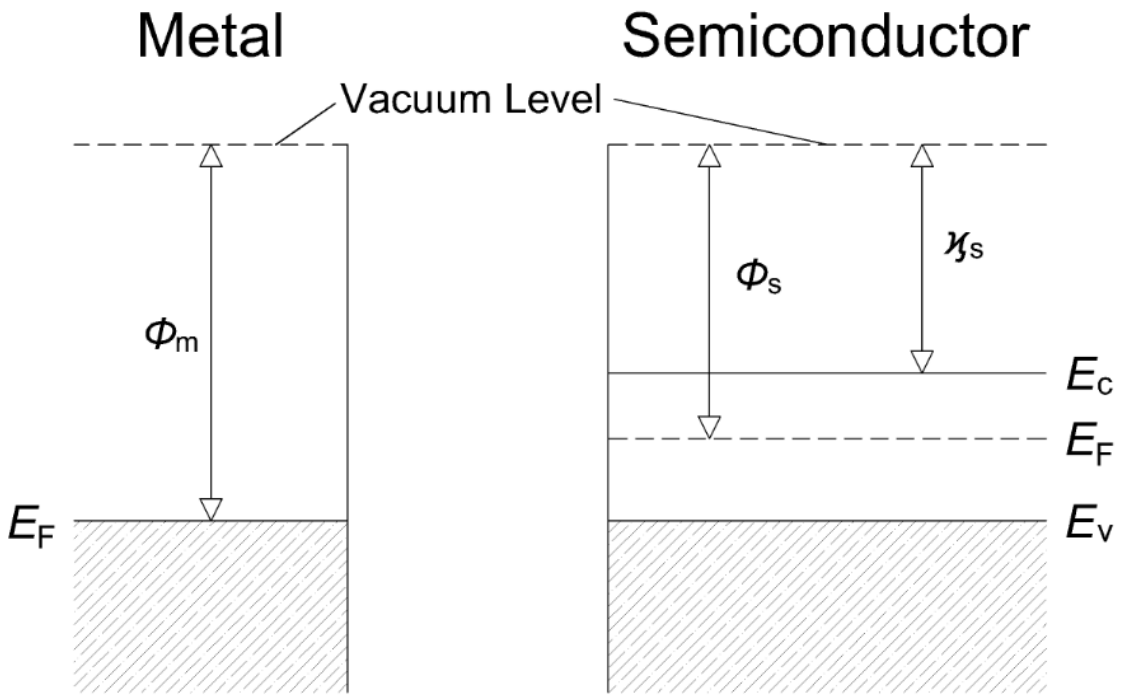

Figure 3.1 - Band diagram for the metal-semiconductor junction. In the metal, the work function (Φ_m), is constant. In the semiconductor, the work function depends on the doping of the semiconductor. χ_s is the electron affinity of the semiconductor.

When there is contact between the metal and the semiconductor, the Fermi level in the semiconductor is higher than in the metal. Therefore, the electrons with higher energy present in the conduction band of the semiconductor, flow into the metal. This flow brings the Fermi level of the semiconductor and the metal into equilibrium. The flow of electrons from the semiconductor into the metal, decreases the concentration of free electrons in the semiconductor region of the interface. This decrease will then increase the separation between the conduction band and the Fermi level. This separation will cause the conduction band edges to bend as shown in Figure 3.2. The lack of electrons on the semiconductor, creates a positive charge in the semiconductor side of the interface, and the electrons that crossed to the metal, create a thin sheet of negative charge within 0.5 Å[1] of the interface. Since the donor concentration is several orders of magnitude smaller than the electron concentration in the metal, the width of the depletion layer is considerable. [24]

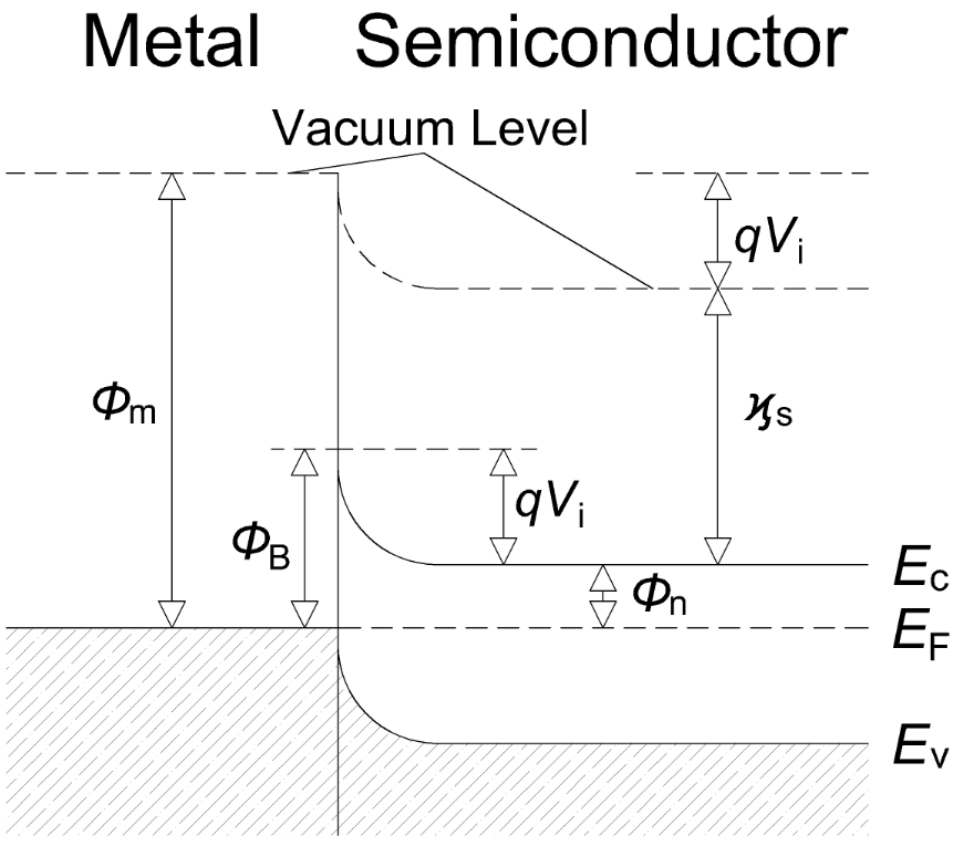

Figure 3.2 - Schottky contact between the metal and a n-type semiconductor. The band bending is evidenced by the bending of the valence and conduction band. The vacuum band also suffers bending. The amount of bending (qV_i) is determined by the difference between the vacuum levels of the metal and the semiconductor.

The band bending of the junction can be seen in the edges of the valence and conduction bands. Since the vacuum level depends on the lower side of the conduction band, it also suffers bending. Therefore, the band bending can be determined by the difference of the vacuum levels of the metal and the semiconductor, which is the same as the difference between the work functions of the substances. The band bending is determined by the expression:

$$qV_i = \Phi_m - \Phi_s \quad (2)$$

[1] This distance is inside the Thomas-Fermi screening distance. It occurs when the wavevector is much smaller than the Fermi wavevector. The screening distance is a theoretical approximation to the screening effect in solids.

where V_i is the contact potential difference, in volts, and qV_i, the potential energy barrier that an electron moving from the semiconductor to the metal must overcome.

From the metal to the semiconductor, the barrier is different, and is given by:

$$\Phi_B = \Phi_m - \chi_s \quad (3)$$

$$\Phi_s = \chi_s + \Phi_n \quad (4)$$

Therefore:

$$\Phi_B = qV_i - \Phi_n \quad (5)$$

where, $\Phi_n = (E_c - E_F)$. It represents how much of the bandgap of the semiconductor the Fermi level penetrates. In the case of n-type semiconductor-metal junction, the band bending is upwards, as depicted in Figure 3.2. In the case where the semiconductor is p-type, the bending is downwards. [24]

In the case of the electrolyte-semiconductor junction the situation is somewhat different. In the electrolyte, the energy levels of the electron are characterized by the redox potential E_{redox}. This is considered as the effective Fermi level of the electrolyte.

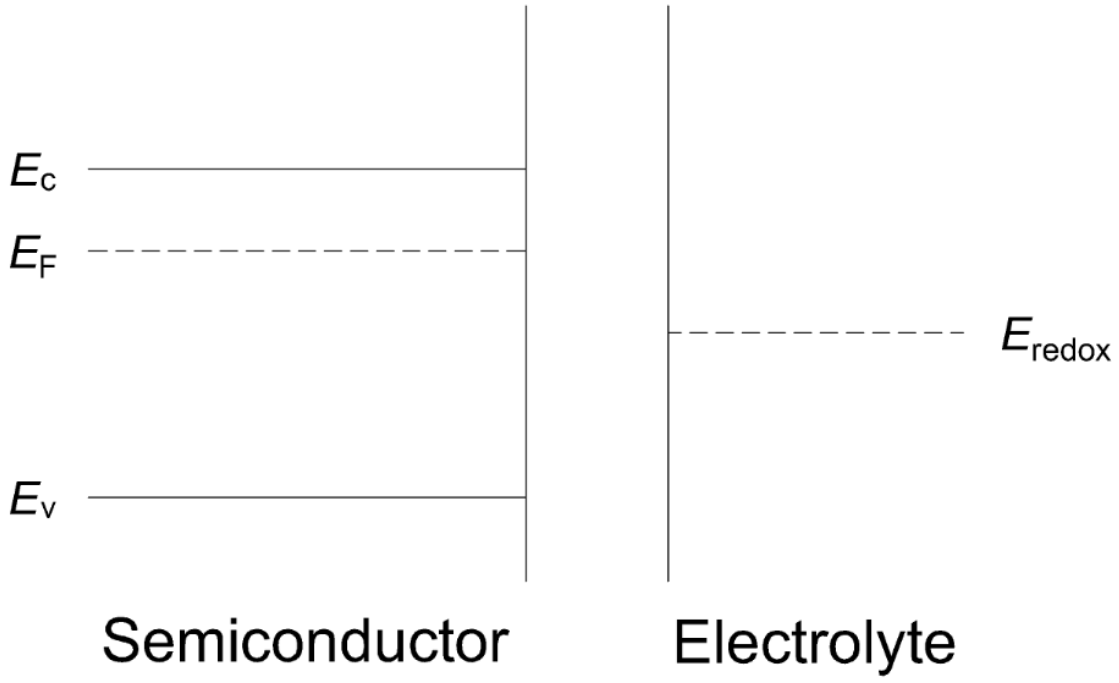

Figure 3.3 - N-type Semiconductor-electrolyte junction before any contact is made. There is no band bending of the conduction and valence bands of the semiconductor.

For a n-type semiconductor, where the E_F is higher than E_{redox} (seen in Figure 3.3), the electrons flow from the semiconductor into the electrolyte, but instead of staying at the surface, as in a metal, a region called the space charge region is created. The electric field in this region can be seen because of the upwards band bending (V_s), in a n-type semiconductor.

On the side of the electrolyte, an ionic layer creates an electric double layer. This ionic layer can be divided more times. The charged layer is located between the solid and the plane with the closest

approach of mobile ions, called the outer Helmholtz plane. The Helmholtz layer is formed by the ions that are attracted to the surface of the electrode by the excess charge in the space charge layer and the polar water molecules. The potential drop that occurs in the Helmholtz layer is determined by the adsorption of H^+ and OH^- ions present in the electrolyte (Figure 3.4).

The charge layer that extends further into the electrolyte is the Gouy-Chapman layer, where an excess of ions of one sign exists. The thickness of the layer depends on the concentration of the electrolyte. Equilibrium between the semiconductor and the electrolyte is achieved when the Fermi level of the semiconductor is the same as the redox potential of the electrolyte ($E_{\mathrm{F}} = E_{\mathrm{redox}}$). [25]

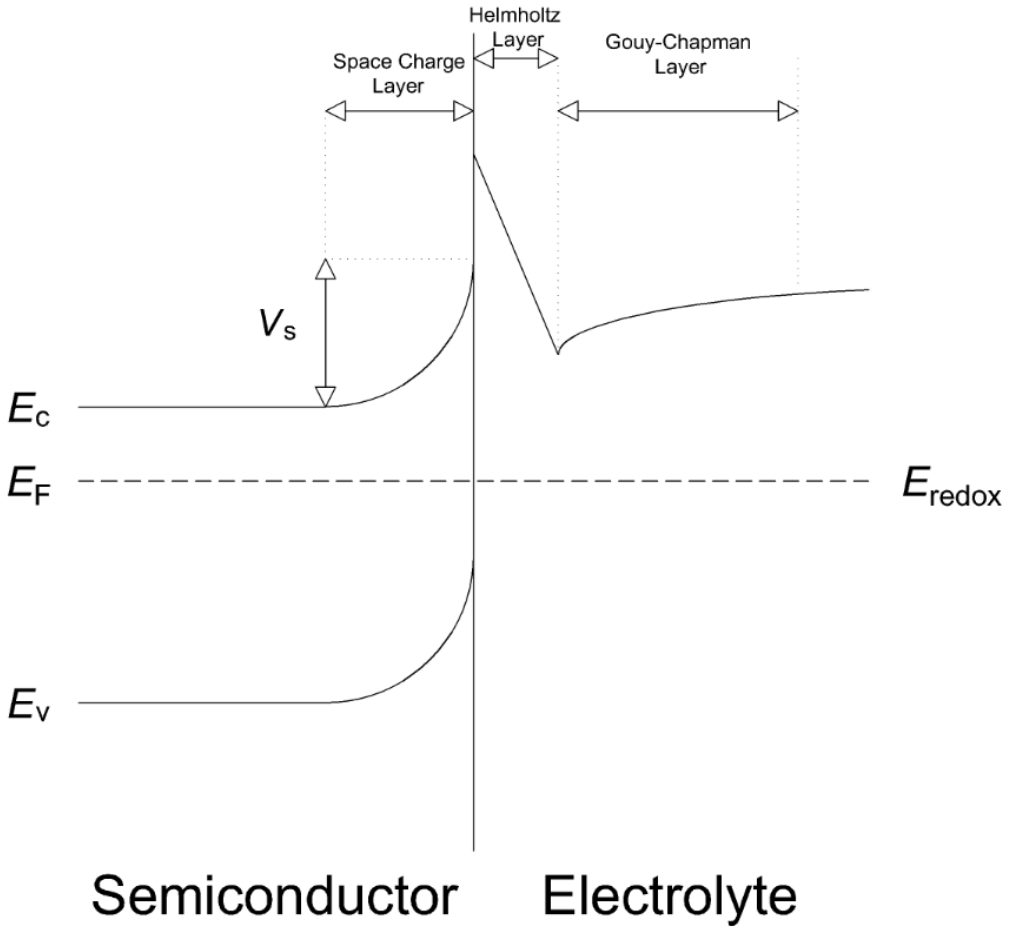

Figure 3.4 - Semiconductor-electrolyte junction after contact is made and equilibrium is reached ($E_F = E_{redox}$). The edge of the conduction and valence band are bent. The Helmholtz and Gouy-Chapman layers are displayed.

According to Ambridge and Faktor [26], the capacitance of the depletion layer C, is given by:

$$C = \left(\frac{qn\varepsilon_0\varepsilon}{2\psi}\right)^{\frac{1}{2}} A \tag{2}$$

where q is the electronic charge, n the net donor concentration, ε_0 the permittivity of free space, ε the relative permittivity of the semiconductor, ψ the barrier height potential, defined as the potential difference between the Fermi Level and the edge of the band where the majority carriers reside and A the area.

The width of the depletion layer (W_{D}) is:

$$W_{\mathrm{D}} = \frac{\varepsilon_0 \varepsilon A}{C} \tag{3}$$

With these equations the average value of the carrier concentration can be calculated from a capacitance measurement. Nevertheless, the accuracy and depth resolution can be higher through the application of a modulation technique [26].

Through the modulation technique, the net donor concentration is given by:

$$n = 2\frac{\varepsilon_0 \varepsilon}{q}\frac{dV}{d(W_{\mathrm{d}}^2)} \tag{4}$$

where dV is the modulation of ψ. [26]

The depth of the etched surface is given by the addition of the depletion layer depth W_D, calculated through equation (2) and the thickness of the material W_{R}, removed through dissolution. W_{R} is determined by the time integration of the dissolution current in Faraday's Law of Electrolysis:

$$W_{\mathrm{R}} = \frac{M}{NFDA} \times \int I\, dt \tag{5}$$

where M is the molecular weight of the semiconductor, N the number of charged carriers which are transferred per molecule of material dissolved, D the density of the semiconductor, A the area and F the Faraday's Constant. [26]

The technique studied in this dissertation is ECV. The usage of this technique is justified by the lower building and operation costs and the measurement of electrically active dopants, instead of the overall dopant concentration like in SIMS.

4. ECV System Development

The designed systems were drawn using the AutoCAD® 3D computer-assisted design software. Four systems were drawn. The designed components were the electrochemical cell, the vacuum chuck, a system to ensure that the sample does not move during the experiments, henceforth called the piston, and a chamber for the electrochemical cell and the input and waste reservoirs.

4.1. The ECV system

The ECV system is composed of four main parts: the electrodes, the lighting system, the sample, and electrochemical cell. A schematic of this system is shown in Figure 4.1.

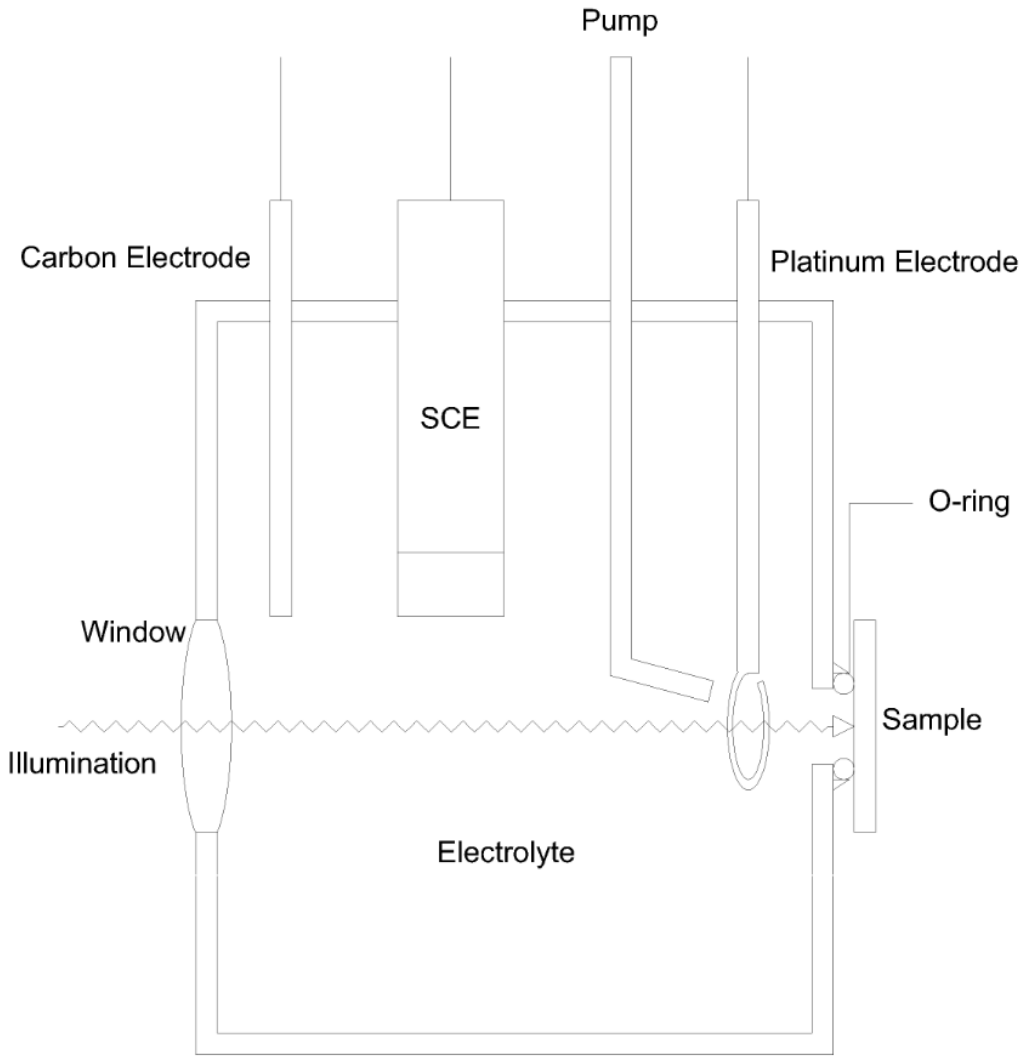

Figure 4.1 - The electrochemical cell consists in a politetrafluoroethylene (PTFE) container, where the eletrolyte is introduced. On the top, the eletrodes are connected, which will perform the measurements. On the left side there is a window for illumination. On the right side, there is a small hole with the o-ring where the sample is placed for the chemical etching.

In the electrochemical capacitance-voltage, three electrodes are used: a carbon (C) electrode, a Saturated Calomel electrode (SCE), and a platinum (Pt) wire. The etching and measuring conditions are controlled by the potential through the cell, which is established by passing a DC current across the semiconductor and the carbon electrode. The current is used to maintain the overpotential necessary which is measured with the potentiostat according to the SCE, which serves as the reference. The Pt wire is used to measure the capacitance and reduces the effect of the series impedance of the electrolyte to an insignificant level. It also alternates between the etching and measuring part of the technique, by passing an AC current. These electrodes are connected to a potentiostat which is used to maintain a constant anodic dissolution potential [26][27][28].

The lighting system consists of a lamp on the side of the electrochemical cell. The lamp is needed to perform the anodic dissolution in n-type semiconductors, since n-type wafers have low positive charge carriers. Sharpe in 1980 [29] and Leong in 1985 [30] used 150 W halogen lamps with a copper sulphate infra-red (IR) filters. Leong [30] achieved an energy intensity of 6 mW/cm^2, for maximum illumination setting. Another lighting system used is with UV lamps. Wolff in 2004 [31] used a 100 W high pressure

mercury lamp with a fused silica filter, while Saraei in 2018 [32] used a ultraviolet (UV) lamp at 60% of maximum intensity.

The sample consists of the wafer on which the measurements are performed. In this dissertation, the wafer will consist of n- and p-doped silicon. The wafer has a connection to the potentiostat through ohmic contacts such as InGa eutectic alloy. The wafer is placed in a vacuum chuck, which will be described later.

The most important part of the ECV system is the electrochemical cell. The electrochemical cell has several openings for the different parts of the ECV system to be connected. The electrochemical cell is a polytetrafluoroethylene (PTFE) reservoir where the electrolyte is introduced. PTFE is used for this part, because of its high compatibility with various chemicals, including HF.

The electrolyte is a substance that, when dissolved in a solvent, produces a solution which can conduct electricity. This type of solution is neutral, but when an electrical potential is introduced, the cations are attracted to the electrode with an abundance of negative charges, while the anions are drawn to the electrodes with a lack of electrons.

Some of the most common electrolytes used for doping profiling are $NH_4F{\cdot}HF$ and $NaF{\cdot}H_2SO_4$. Other not so common electrolytes are potassium hydroxide (KOH), used by Ambridge and Faktor [26], or Tiron[2], used by Saraei [32] and Yakovlev [33].

For the electrolyte to be considered adequate for the ECV, it must satisfy the following 2 conditions[34]:

- It must form a near ideal Schottky contact with the sample.
- The etching must be uniform with a reasonable etch rate.

The etch rate (E_r) can be determined through the equation:

$$E_r = \frac{dm}{dt} \tag{6}$$

where m is the mass of dissolved semiconductor and t the immersion time [35].

In 1992, Peiner [36] detected that the dissolution rate was different according to the concentration of the electrolyte. Liu [37], in 2014, determined that the etch depth reached saturation at a depth of 43 nm.

In Table 4-1 some etching characteristics can be found. Hu and Kerr [38] determined that the etch rate depends on the concentration of the OH^- ion. They achieved an etch rate of 1.8 $nm{\cdot}h^{-1}$ for (48%) HF, and 4.68 $nm{\cdot}h^{-1}$ for a solution of 96 cm^3 H_2O + 2 cm^3 (48%) HF + 4.3 g NaF. Peiner [36] achieved an etch rate between 2 and 4 $\mu m\ h^{-1}$, for a solution of 1 part of 1 M NaF/0.05 M H_2SO_4 diluted in 0.57 parts of water. A more complete version of this table can be found in the Annex. A complete table with etch rates achieved in silicon wafers, using different etchants, can be found in the book Electrochemistry of Silicon and its Oxide [25].

Table 4-1 - Etching characteristics for some experiments. It shows the etch rate depending on the characteristics of the electrolyte and the wafer used. Peiner achieved different etch rates, depending on the concentration of electrolyte.

Author	Wafer	Electrolyte	Illumination	Wafer Doping	Etch Rate

[2] $C_6H_4N_2O_8S_2$ [60]

Hu and Kerr [38]	n-type Silicon	(48%) HF H_2O+(48%) HF + NaF	None	Not mentioned	1.8 nm·h^{-1} 4.68 nm·h^{-1}
Leong [30]	n and p-type Silicon	1 M NaF/0.05 M H_2SO_4 diluted in x parts of DI H_2O	150 W halogen lamp w/ copper sulphate infra-red filter	Antimony	0.8 µm h^{-1} for x=0.75
Peiner [36]	n and p-type Silicon	0.1 M $NH_4F{\cdot}HF$	150 W quartz halogen lamp w/ 480 nm blue filter	Boron or Phosphorus	2-4 µm h^{-1} for x=0.57 0.2-0.5 µm h^{-1} for x=0.28
Liu [37]	p-type Silicon	HF 40ºC 5% (weight percent)	None	Phosphorus	48 nm h^{-1} for $N > 3 \times 10^{20}$ cm^{-3} 1.2 nm h^{-1} for $N < 3 \times 10^{20}$ cm^{-3}

Another important part of the electrochemical cell is the sealing ring, which will determine the contact area between the electrolyte and the sample. This contact area must be very carefully measured because both the capacitance and the etched depth depend on it. Therefore, a sealing ring with the correct characteristics is necessary. The sealing ring must be soft enough so it does not damage the sample, but hard enough so that it can maintain its shape during the experimental procedure. A possibility for the material of this O-ring is PTFE or PVC.

To measure the etch depth, profilometry will be used. The most common profilometry system is the stylus profilometer. In this system, a stylus moves over a surface and detects height variations in said surface. The movements of the z-axis of the stylus through the surface are converted into electrical signals by a transducer. Depending on the size and shape of the stylus tip, the lateral resolution can vary. For the optimum tip, a lateral resolution of 0.05-0.15 µm can be achieved. But depending on the tip of the stylus it can cause problems to the surface or to the stylus. A higher slope can dent the stylus, or the stylus can scratch the surface. The vertical resolution is influenced by several factors, including noise from the parts of the system. The noise has been measured to be as small as 0.05 nm under optimum conditions [39]. In the ECV, what is to be measured is the etch depth, therefore the results needed from the profilometer is the absolute variation of height in the semiconductor surface.

Etching

Chemical etching consists in a chemical reaction in which a material is dissolved in a liquid solvent. The etching process can have more than one chemical reaction. Some of these reactions can be oxidation-reduction, redox, of which electrochemical etching is a special case. Redox reactions can

happen by use of an oxidizing agent, or through an electrochemical cell, where the etched material is the anode, when an external electromotive force is applied. During the electrochemical etching, complex formations can occur in conjunction with the redox reaction. This means that the ligand groups bond with the etched species to form a molecule which is soluble in the etchant.

When a silicon wafer is doped, the I-V curve of the wafer is altered. For p-type silicon, the anodic current in the wafer is high. For n-type silicon, the current is very low, being limited by the low hole concentration. For a n-type silicon wafer under illumination, the i-V curve has similar characteristics to the p-type silicon. These variations of the i-V curve are demonstrated in Figure 4.2.

Depending on the voltage applied during the etching, the resulting surface is different. For voltages between 1 and 5 V, the silicon surface is relatively rough. When the applied voltage is higher than 5 V, then the surface is brightly smooth.

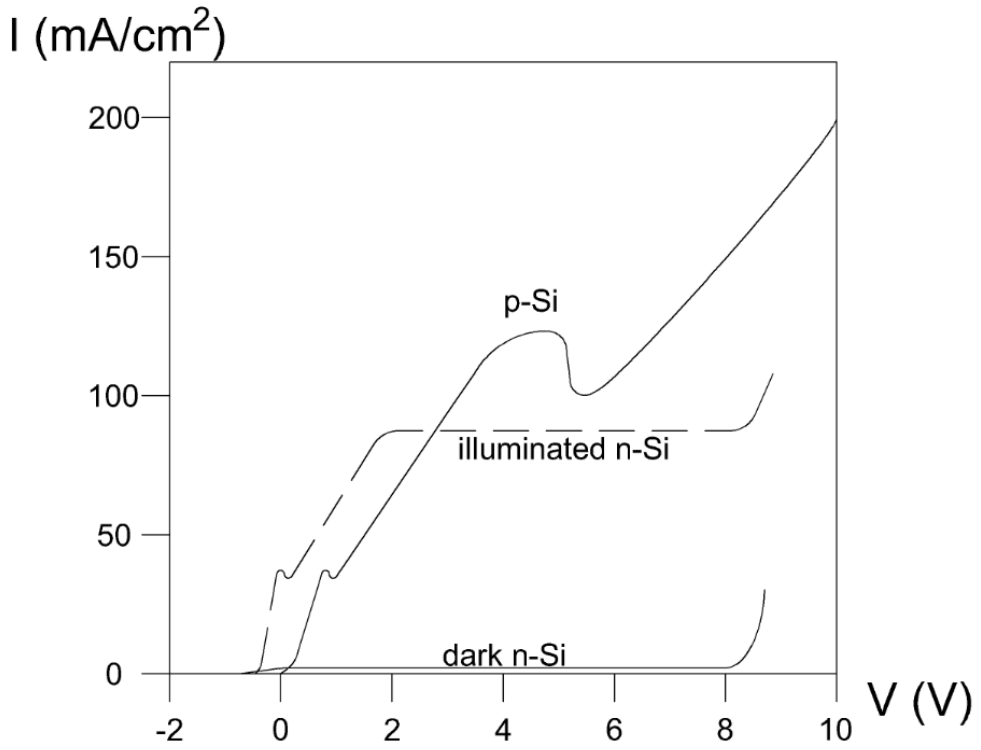

Figure 4.2 - IV curves for p-type Si (top full line), dark n-type Si (bottom full line) and illuminated n-type Si (dashed line) in a 2.5 wt% HF solution. The i-V curve for dark n-type is caracterized by a very small current, up to ~8 V, where the current increasses. The illuminated n-type presents a similar behaviour as the p-type SI, until ~1.5 V, where the current stays constant up to ~8 V. In the p-type Si, the current increases with the voltage, except between 5-6 V. Image based on the Current-potential curves available in Zhang [40].

The conduction of charge carriers across the depletion layer differs according to the doping of silicon. In the conduction band, the conduction is due to the injection of electrons, while in the valence band, conduction is due to the capture of holes. The conduction of charge carriers depends not only in the doping of silicon, but also in illumination and electrode potential.

For p-type silicon, the anodic reactions occur in the valence band. On the other hand, for n-type silicon, the anodic reactions occur in the conduction band, but if illuminated, the reactions occur also in the valence band. The intensity of illumination influences the participation of each band.

The conduction of charge carriers also varies according to the dopant concentration. For low doped p-type, the transfer process over the barrier is by thermal emission. For low doped n-type silicon, the charge transfer is limited by the minority charges, meaning that dissolution only happens if enough holes are being generated by illumination. In HF solutions, the current can be high enough due to tunnelling effects. For both high doped p- and n-type silicon, charge transfer is due to Zener tunnelling [41].

Etching takes place in sequential steps. The kinetics vary according to the rate-limiting step. If the chemical reactivity of the species is the limiting step, then the process is said to be activation limited. If the limiting rate is determined by the fresh etchant renovation, then the process is diffusion limited. Therefore, if multiple materials, in a diffusion limited process, are etched by the same solution, the etch rate is the same for all materials.

The etching process is influenced by various factors. The concentration of the etchant, in which a low concentration etching process can be diffusion limited, while for a high concentration etchant the process can be activation limited. The temperature of the solution can alter the etching kinematics. If a catalytic species is present in the solution, the etch rate can be influenced. Through the agitation of the solution the limitations of diffusion processes can be minimized. The pH of the solution also has an effect in the etch rate [42].

Some adsorption effects can occur during the etching. A substance can be adsorbed into the substrate which influences the etching. If the adsorbed substance is a reactant, it can facilitate the process. On the other hand, if the substance does not react with the substrate, then it can slow down the etching or even stop it completely. [43]

The liquid etching of silicon can be done with different electrolytes, among them, aqueous solutions of $NaF{\cdot}H_2SO_4$, $NH_4F{\cdot}HF$, or HF, in different concentrations. Hu and Kerr [38] determined that the etching of silicon with HF happens with an etch rate of 0.3 Å/min, but has a faster reaction in the presence of water, with an etch rate of 0.4 Å/min. This is due to the oxidation of silicon by the hydroxyl ions, which are formed during the autoionization of water. Matsumura and Fukidome [42] demonstrated the effect of pH in the etch rate with fluorine solution. The etch rate has a peak at pH of 6.4, and it is near zero at pH of 8.5.

According to Memming [44], the reactions during the etching of silicon changes according to the concentration of HF present in the electrolyte. For high concentrations (10 M), the etching reactions are:

$$\mathrm{Si} + 2\,\mathrm{HF} + \lambda\,\mathrm{h} \rightarrow \mathrm{SiF_2} + 2\,\mathrm{H^+} + (2-\lambda)\,\mathrm{e^-} \tag{1}$$

$$\mathrm{SiF_2} \xrightarrow{\text{rapid}} \mathrm{a-Si} + \mathrm{SiF_4} \tag{2}$$

$$\mathrm{a-Si} + 2\,\mathrm{H_2O} \xrightarrow{\text{slow}} \mathrm{SiO_2} + 2\,\mathrm{H_2} \tag{3}$$

$$\mathrm{SiO_2} + 6\,\mathrm{HF} \xrightarrow{\text{rapid}} \mathrm{H_2SiF_6} + 2\,\mathrm{H_2O} \tag{4}$$

$$\mathrm{SiF_4} + 2\,\mathrm{HF} \xrightarrow{\text{rapid}} \mathrm{H_2SiF_6} \tag{5}$$

Equation (1) corresponds to an electrochemical reaction, where $\lambda\ h$ are the needed holes for the reactions and $(2-\lambda)\ e^-$ are the released electrons.

Furthermore, the hexafluorosilicic acid (H_2SiF_6) produced during the etching, can later be used to synthesize ammonium bifluoride ($NH_4F{\cdot}HF$ or NH_4HF_2), with the addition of ammonia (NH_3) described

in [45]. The resulting ammonium bifluoride can be used as an etchant for silicon, due to the presence of hydrofluoric acid.

In $NH_4F{\cdot}HF$ solutions, the concentration of each substance has an effect in the etch rate. For constant concentration of NH_4F, the etch rate is lower for higher concentrations of HF. On the other hand, for constant concentration of HF, the etch rate is higher with higher concentration of NH_4F.

The ECV technique uses an electrolyte for the measurements. This permits an alternation between CV measurements and etching. By etching the surface, the doping profile can be made to any depth [46].

Vacuum system

At atmospheric pressure, particles are numerous and collide with surfaces and other particles, creating a pressure in the surfaces. By decreasing the number of particles, the pressure in a chamber also diminishes, creating a vacuum.

A vacuum system is a system that combine pumps, valves, and pipes to create a lower pressure zone. This system can be as simple as an aspirator, to a complex system as an underground particle accelerator.

To remove air from a chamber at atmospheric pressure, a displacement pump is normally used. This type of pump has low-pressure limits ranging from 10^{-1} to 10^{-3} Pa [47].

The vacuum chucking of wafers is made through the creation of partial vacuum on the back side of the wafer, through an array of holes in the vacuum chuck surface [48]. Since there is a small pressure on the back of the wafer, the atmospheric pressure on the front side of the wafer pushes it against the chuck surface, holding it in place. A diagram of this effect is shown in Figure 4.3.

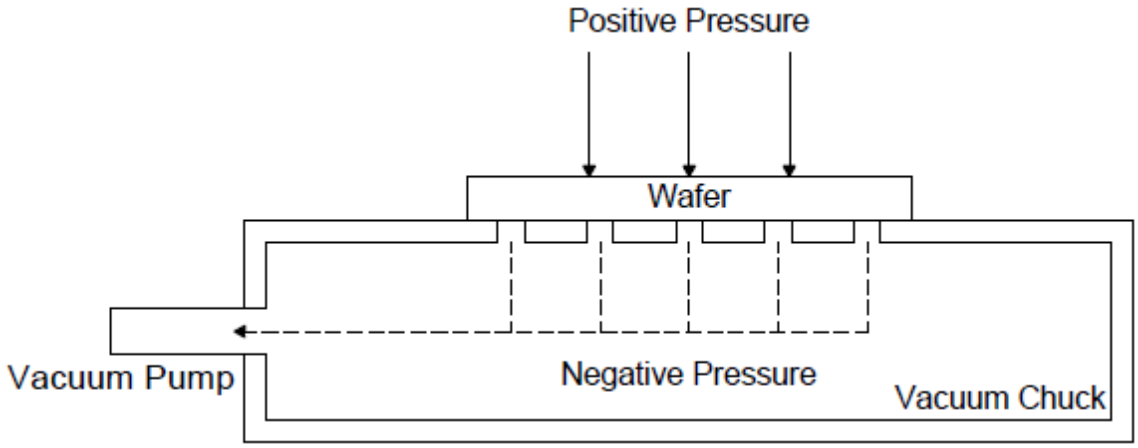

Figure 4.3 – Diagram of vacuum systems. The vacuum pump creates a region with low pressure inside the chuck. The higher pressure on top of the wafer pushes it to a place with lower pressure. The dashed line corresponds to the direction of the pumped air.

4.2. Electrochemical Cells

For the electrochemical cell, the two designs vary according to the positioning and number of electrodes. The rest of the design has two 5 mm radius holes, one in the back of the cell (1), through which the illumination of the sample can be made, and another in the bottom (2), for the removal of electrolyte. Two 2 mm radius holes, one on the top (3) for electrolyte insertion and one to connect to the sample (4). This part of the system is constructed in PTFE, due to its chemical resistance to various chemicals, including HF. The construction would start by hollowing out a slab of PTFE, leaving a reservoir without one side, and later drilling the holes in the correct place. Finally, the missing side would be screwed to the PTFE reservoir.

The first system, in Figure 4.4, has the pump (5), and is based in the needs of the technique. This means, three electrodes centred in the top of the cell (6). These holes have 1 mm radius, except for the SCE electrode, which has 2.5 mm radius.

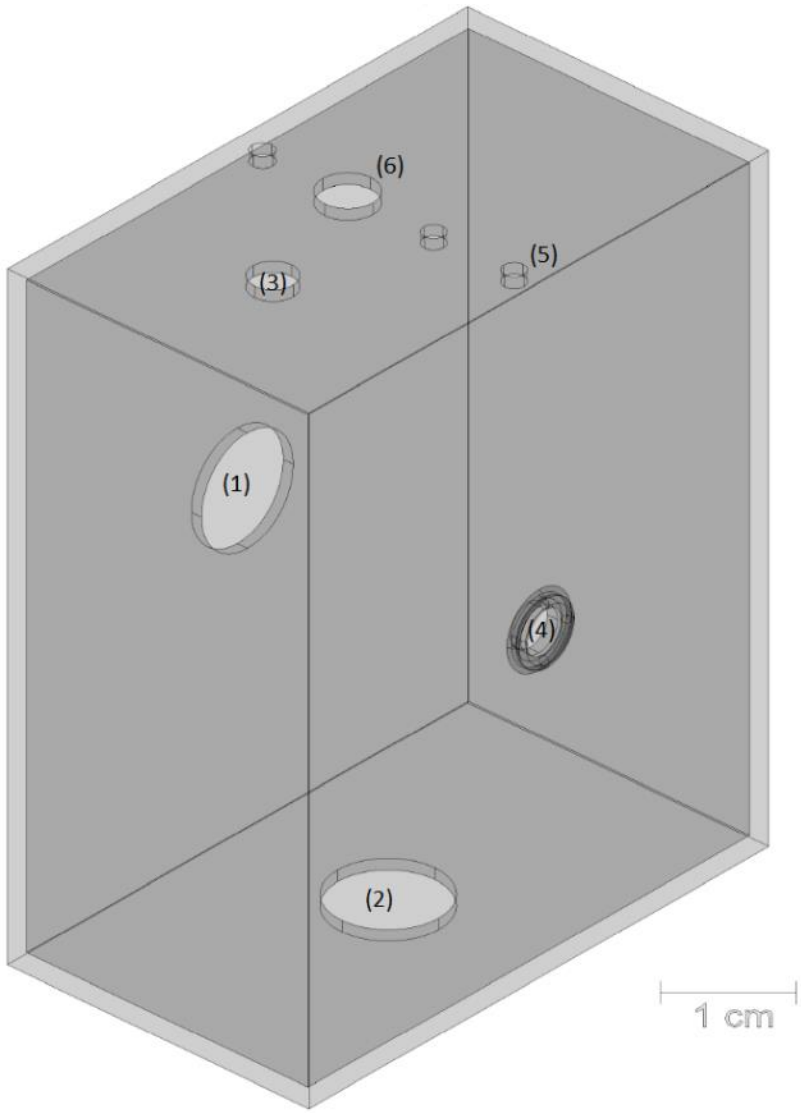

Figure 4.4 - Schematic of the three-electrode electrochemical cell. (1) corresponds to the orifice for the light needed for n-type etching. (2) the connection to the waste reservoir. (3) the connection to the input reservoir. (4) the orifice to the sample. An O-ring attachment exists here. (5) the pump orifice to prevent the buildup of hydrogen bubbles. (6) Three electrode orifices. From the light to the sample, a carbon electrode, a SCE and a platinum wire. This electrochemical cell was designed according to the needs of the ECV technique.

The diagram for the top side of the 3-electrode electrochemical cell is in Figure 4.5.

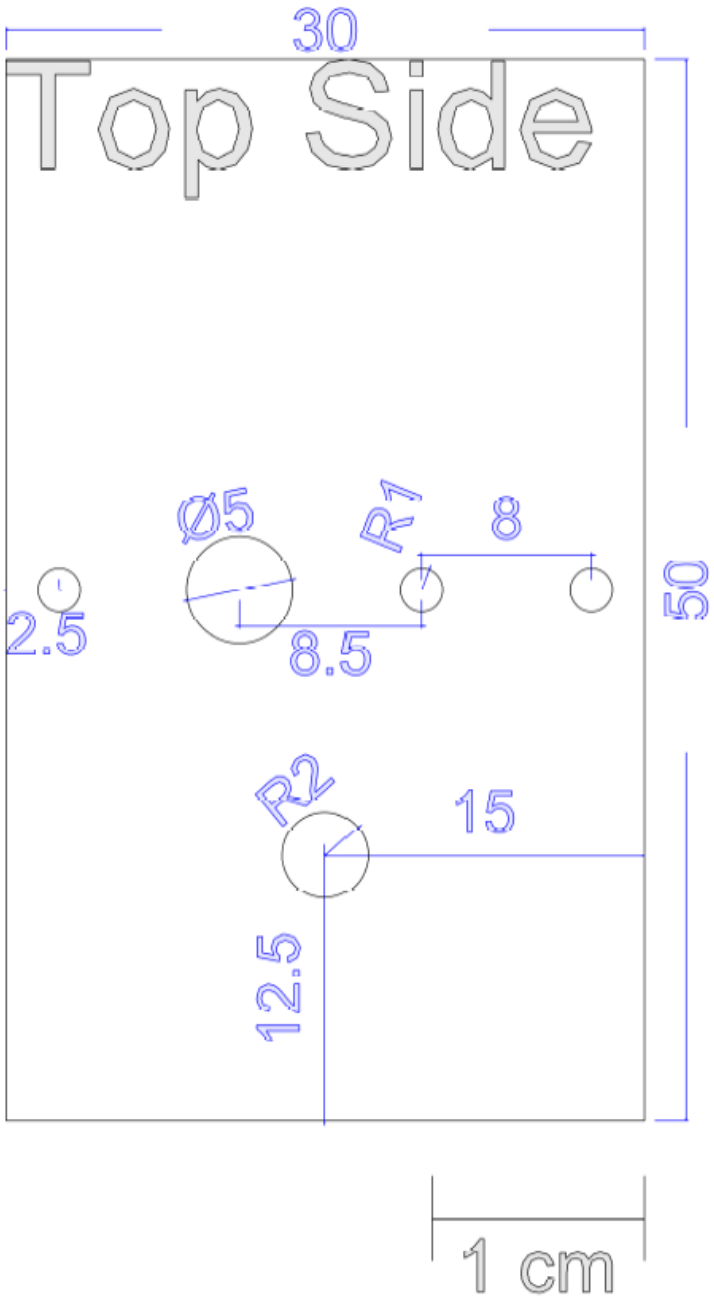

Figure 4.5 - Diagram of the top side of the electrochemical cell, based on the needs of the system. This electrochemical cell has an input orifice for the introduction of the electrolyte, a pump orifice to prevent the accumulation of hydrogen bubbles on the surface of the sample and three electrode orifices. One for the carbon electrode, one for the reference electrode and one for the platinum electrode.

The second electrochemical cell, in Figure 4.6, is based on cells in commercial ECV. It has one 1mm radius hole for the pump (5), plus six 1 mm radius holes for the electrodes (6).

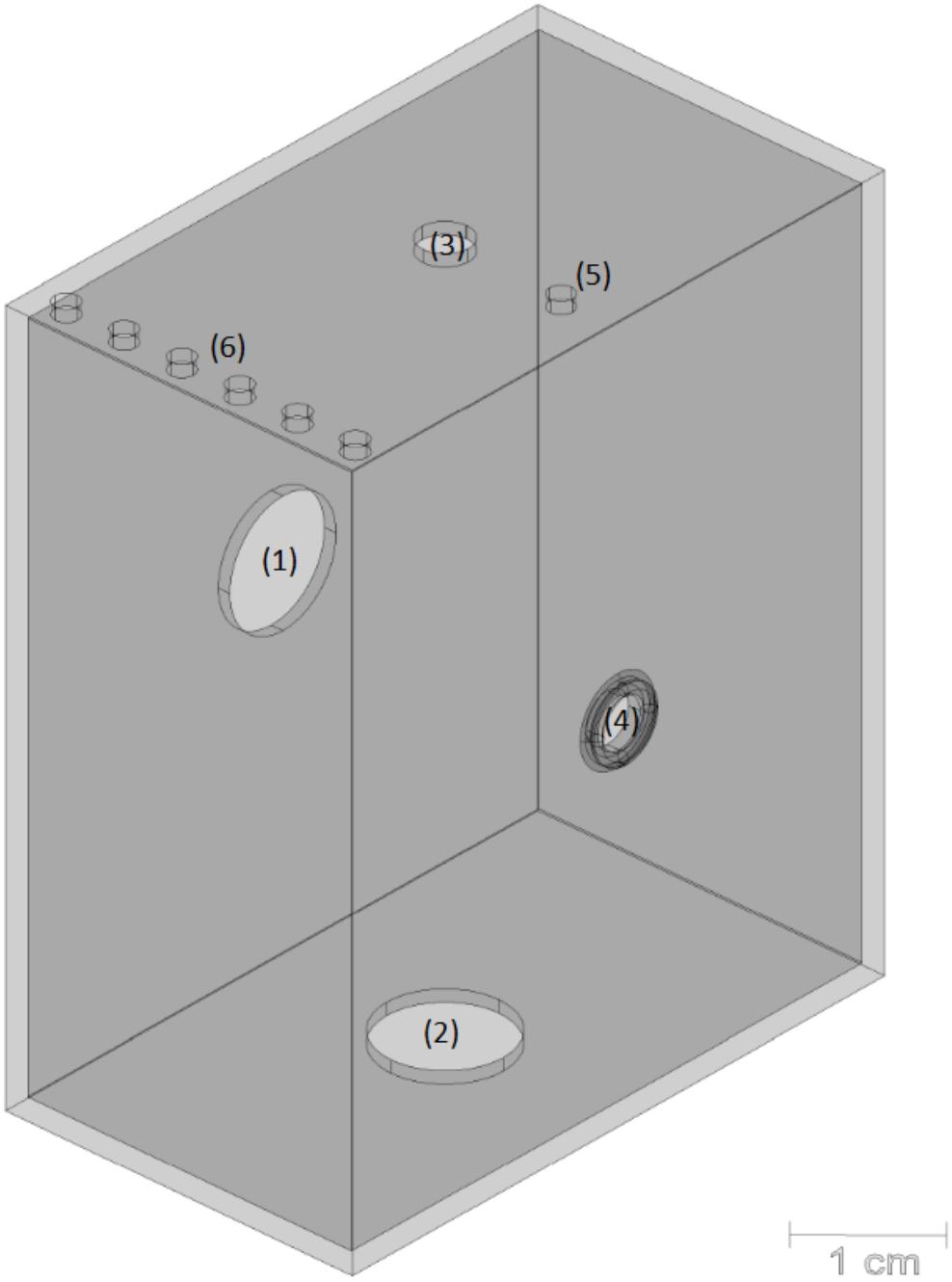

Figure 4.6 - Schematic of the six-electrode electrochemical cell. (1) corresponds to the orifice for the light needed for n-type etching. (2) the connection to the waste reservoir. (3) the connection to the input reservoir. (4) the orifice to the sample. An O-ring attachment exists here. (5) the pump orifice to prevent the buildup of hydrogen bubbles. (6) corresponds to six electrode orifices. This electrochemical cell is based on the commercial ECVs

A diagram for the top side of the 6-electrode is represented in Figure 4.7.

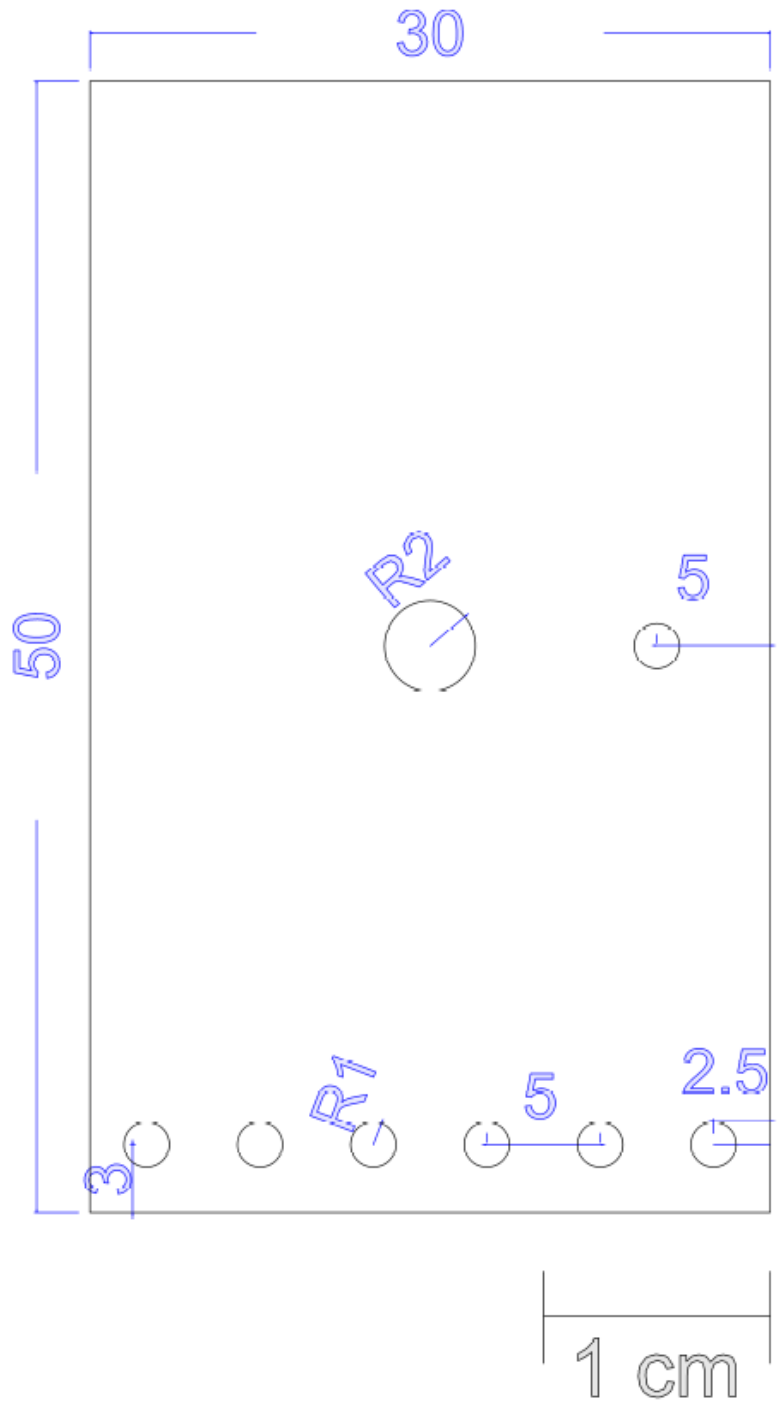

Figure 4.7 - Diagram of the top side of the commercial ECV-based electrochemical cell. It contains an input orifice to introduce the electrolyte, a pump orifice for the prevention of hydrogen bubbles on the sample, and six electrode orifices.

In the sample orifice, there exists a small attachment for the O-ring. Figure 4.8 is a close-up of this attachment with the O-ring (in cyan), and Figure 4.9 without the O-ring. The O-ring has an interior diameter of 3 mm, and a cross section of 1 mm.

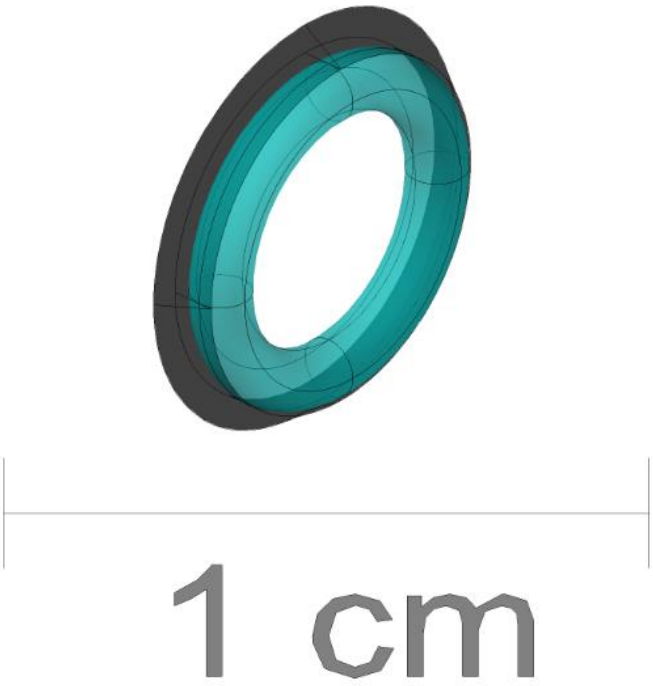

Figure 4.8 - O-ring holder with O-ring (in cyan). It is used to keep the O-ring in place during measurements.

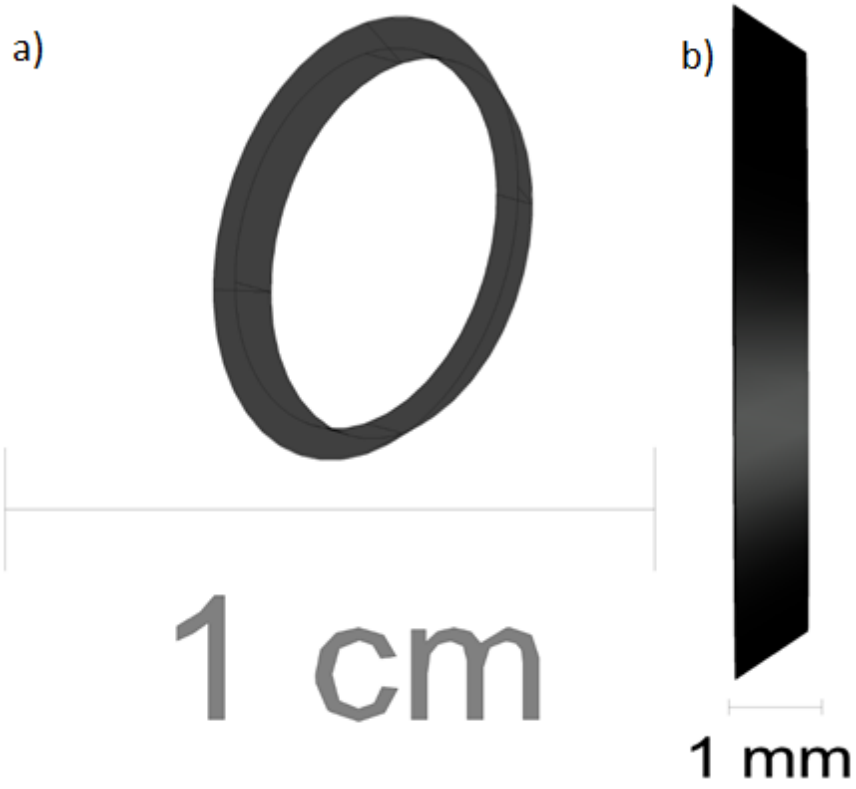

Figure 4.9 - a) O-ring holder; b) O-ring holder, side view. This piece is used to hold the O-ring in place during the measurements. Its height is 75% of the height of the O-ring, so that it does not touch the sample, but the O-ring stays inside it, and itself defines the contact area.

4.3. Vacuum Chuck

For the vacuum chuck, the main objective was to hold in place wafers of different sizes, by creating a negative pressure inside the chuck. In turn, the outside, being in higher pressure, pushes the wafer against the chuck. Therefore, two different systems were designed which removed the air (decreasing the internal pressure) in two different ways. The vacuum chucks consist of two plates, one at the top and one at the bottom. Depending on the system, the complexity of each plate is different.

The first system is called the O-ring vacuum system. The second is named the valve vacuum system. Both systems are composed of two plates of aluminium. They would be constructed separately, by drilling the holes and the airways. After the two plates are constructed, they would be joined together with screws.

The O-ring vacuum system, in Figure 4.10, was drawn with only one connection between the outside and each of the airways. Each airway connects to various holes in the top layer of the chuck, creating a negative pressure beneath the wafer. Since the pressure on top of the wafer is higher than the pressure below the wafer, the wafer stays stuck against the chuck. The O-ring vacuum system has airways connecting each sequence of holes. To prevent vacuum from being created in the wrong holes, the system would be opened, and the airway blocked with an O-ring.

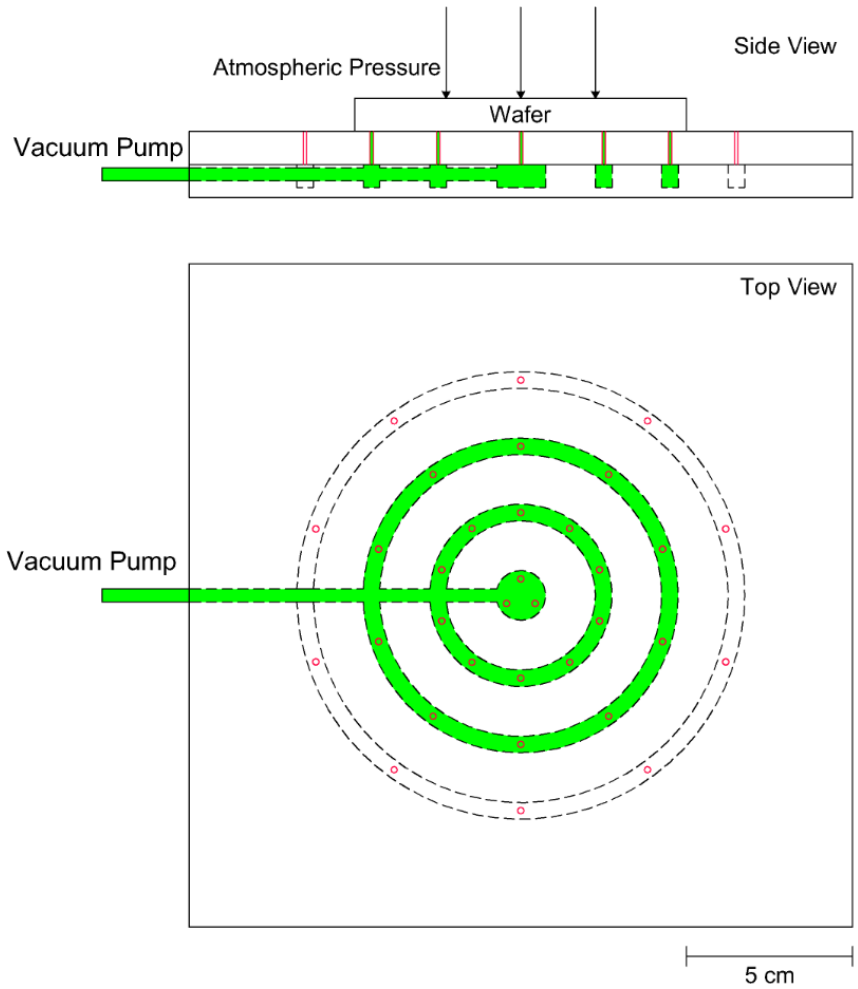

Figure 4.10 - Diagram of the O-ring vacuum chuck. The dashed lines represent the airways inside the chuck. When the vacuum pump is on, the air inside the chuck is removed, creating a negative pressure inside the it, seen in green. The red holes connect the chuck to the wafer. These are the points where the pressure is low, right beneath the wafer. Since on top of the wafer the pressure is higher, then wafer is stuck against the chuck. The blank airways are at atmospheric pressure.

The bottom plate (Figure 4.11) consists of an aluminium plate with a channel, with a radius of 2 mm and four grooves, 5 mm thick, each filled with a 5 mm thick O-ring. These O-rings are used to prevent vacuum from being made in locations where it is not needed. For example, if the wafer is not big enough to reach the last groove, then vacuum cannot be made in these holes, if an O-ring is placed on the bigger groove. The number of filled grooves depend on the size of the wafer, for bigger wafers less grooves are filled, for smaller wafers, more grooves are filled. Since the wafer is placed at the middle of the chuck, the grooves are filled with O-rings from the bigger to the smaller groove. This system has the capability to be opened, so the O-rings can be placed or removed. The top plate, which the wafer will be pushed against, has thirty-six holes, each with a radius of 1 m. The O-rings prevent vacuum in the unnecessary holes if the wafer is too small. A possible material for this O-ring is a fluorocarbon such as Viton.

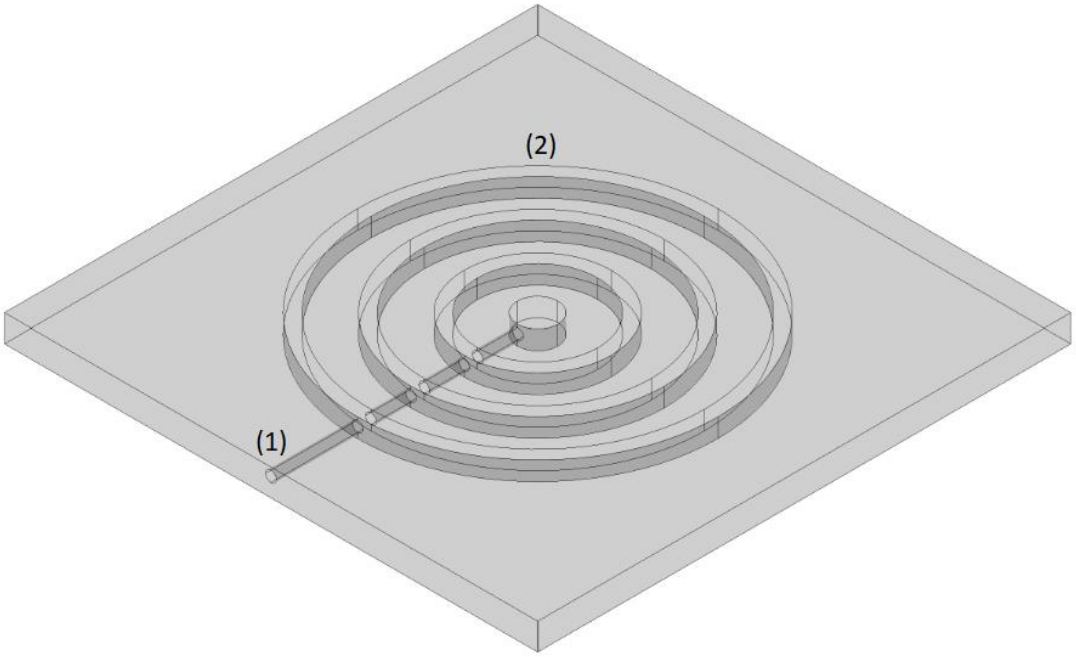

Figure 4.11 - Bottom plate of the O-rings vacuum system. It is an aluminium plate, with a tube that connects to the outside (1). This tube, then connects to four different airways (2). This plate is joined to the top plate, where the sequence of orifices match the airways in this plate.

The top part of the O-rings vacuum system depicted in Figure 4.12, consists in thirty-six orifices. These match the airways inside the bottom plate and are the places where the low pressure is in contact with the wafer.

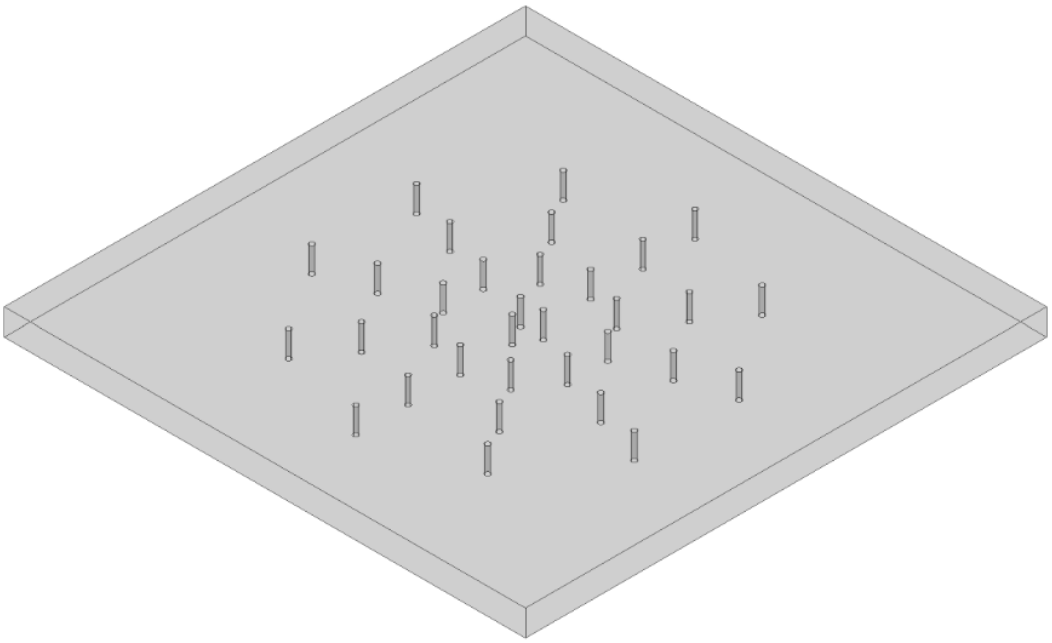

Figure 4.12 - Top plate of the O-ring vacuum system. It consists of a aluminium plate with thirty-six holes. These holes are the points of low pressure beneath the wafer.

The complete system is represented in Figure 4.13.

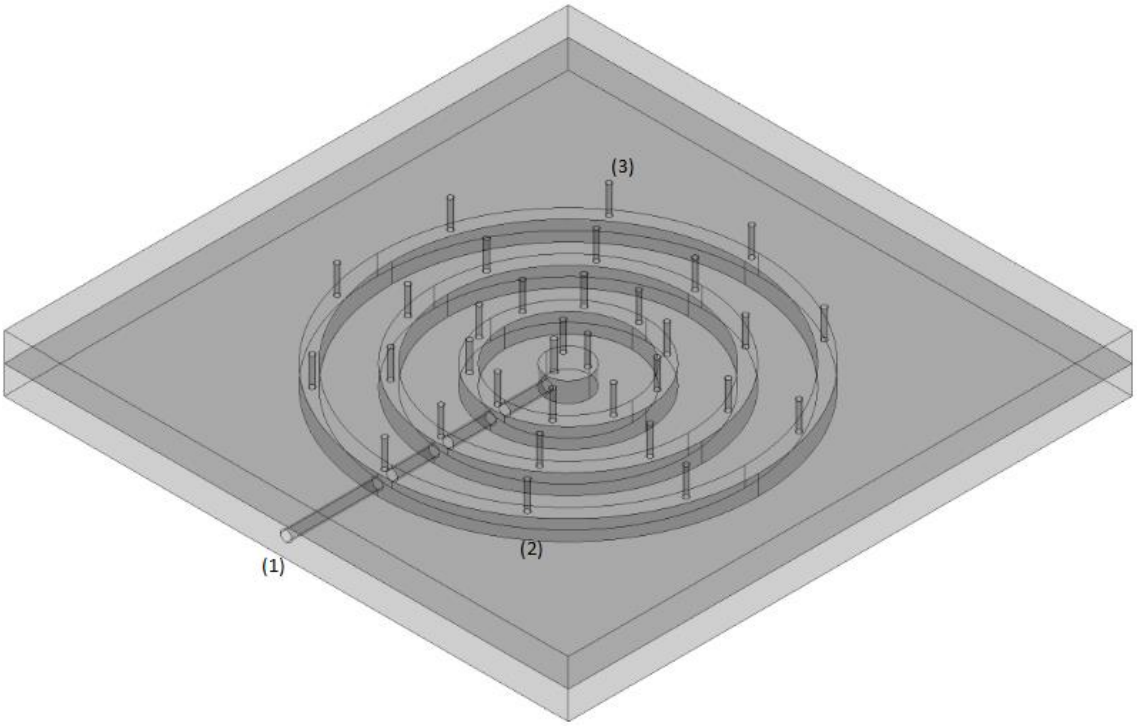

Figure 4.13 - O-ring vacuum system. (1) is the connection to the outside. (2) are the airways. According to the size of the wafer, different airways can be blocked by O-rings. (3) are thirty-six holes connecting the airways to the back of the wafer. They create a pressure differential with the front of the wafer.

The second vacuum chuck created has one connection to the outside of the chuck per airway, as seen in Figure 4.14. Each of the outside connections has a valve which prevents vacuum from being created in the unnecessary airways. Then each of the airways connects to a set of holes on the back of the wafer. Unlike the O-ring system, the valve system would stay closed. The airways would be blocked when the valve was closed. This system also includes O-ring grooves between each of the airways and the outside, preventing any leaks from occurring during the measurements.

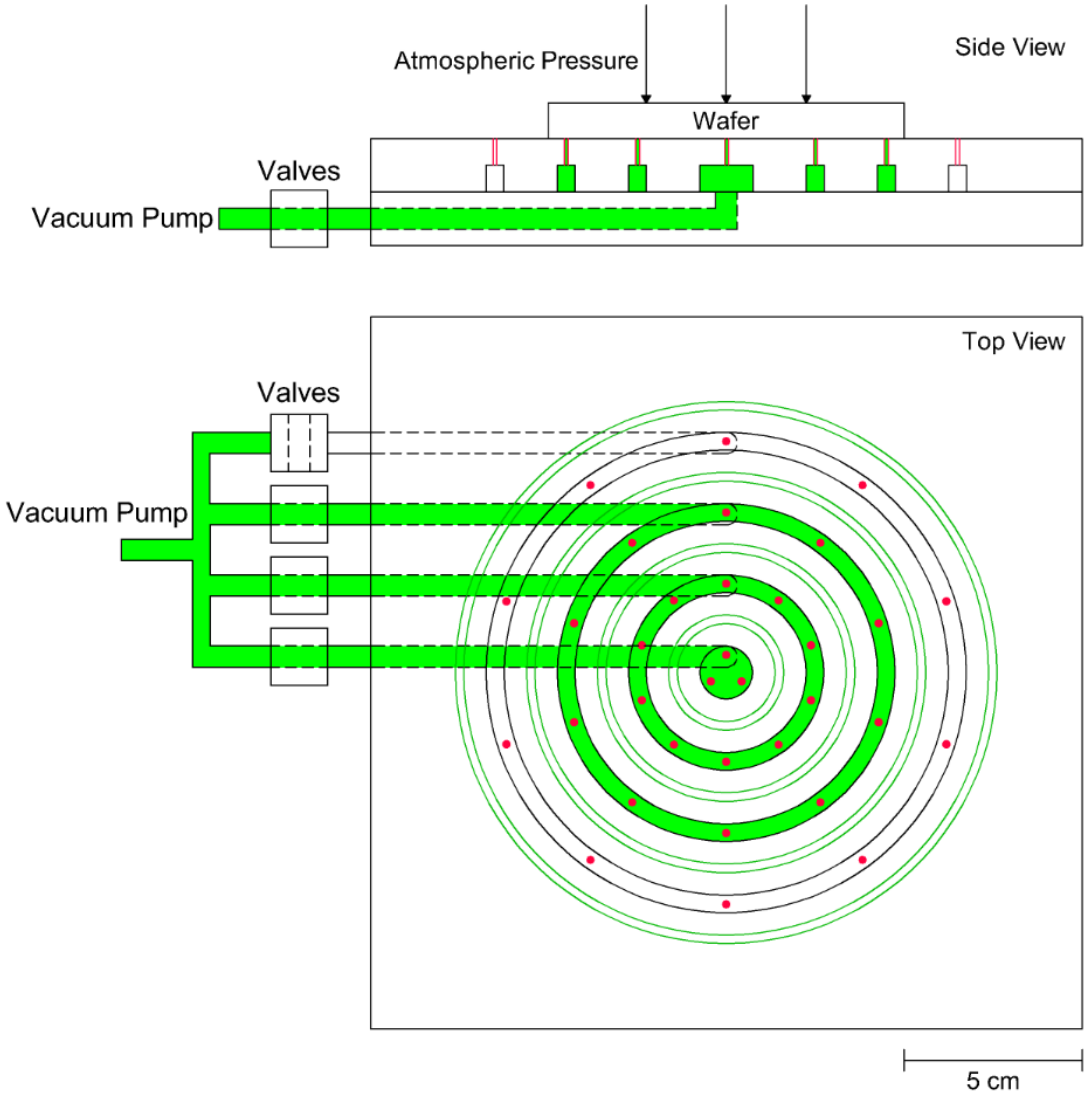

Figure 4.14 - Diagram of the valves vacuum chuck. In this one, the vacuum pump connects to four different valves. These valves will prevent vacuum from being made in unnecessary airways. The dashed lines correspond to the connections between the outside and the top layer of the vacuum chuck. Each of these connections links to an airway on the top layer. The airways, in turn, connect to the holes (in red) which create the lower pressure beneath the wafer. The dark green lines correspond to the O-rings grooves which prevent leaks during the operation.

The second system is called the valve system, Figure 4.17. Compared with the first system, it has a simpler bottom plate, but a more complex top plate. The bottom plate, in Figure 4.15, has four tubes connect the top plate with the outside (1). Four O-ring grooves (2) guarantee there are no leaks. Four the outside connections are made on the side of the wafer. The top plate (Figure 4.16) has four airways (2) which connect to thirty-six holes (1), with radius of 1 mm, to which the wafer will be pushed against.

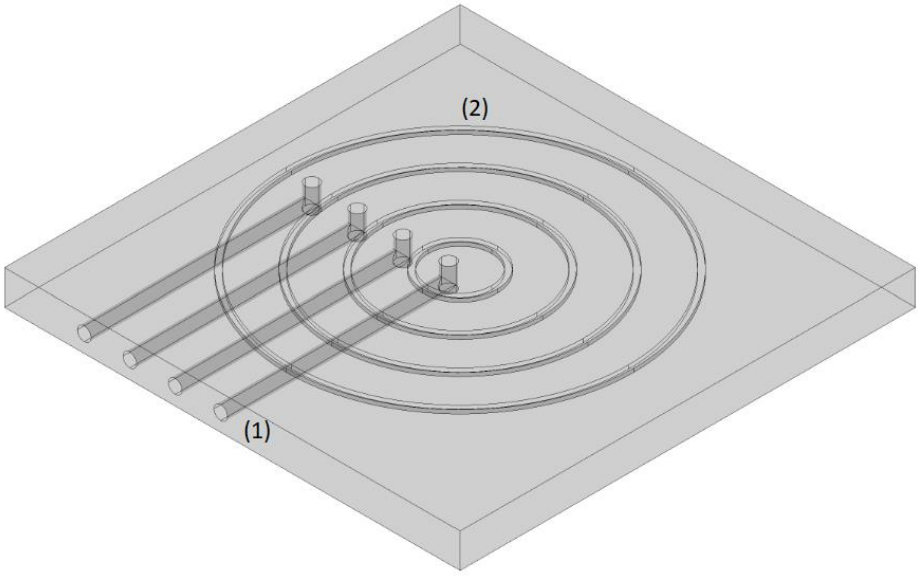

Figure 4.15 - Bottom plate of the valves vacuum system. This aluminium plate has four tubes (1) which connect the vacuum pump to the top plate. It also has four grooves (2) to place O-rings. These prevent any leaks during the measurements.

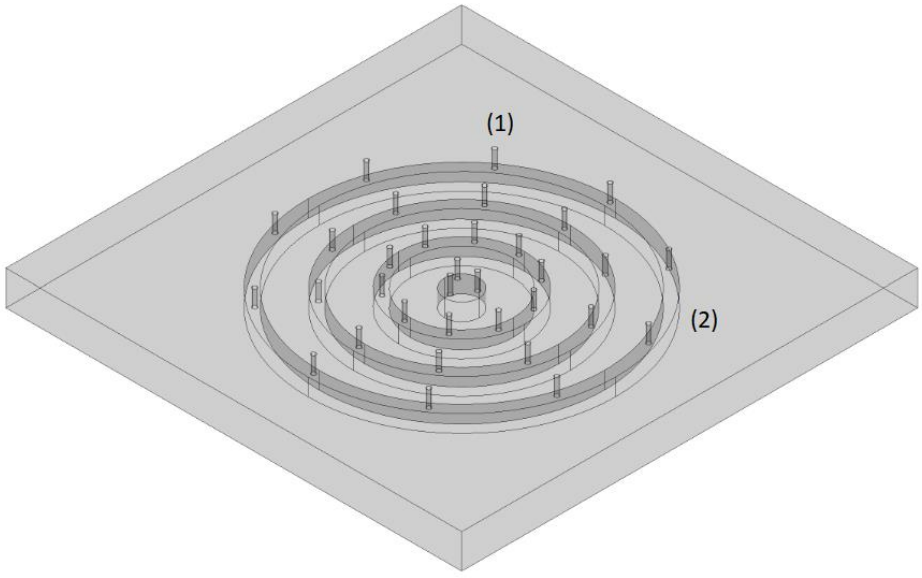

Figure 4.16 - The top part of the valves vacuum system. It has thirty-six holes (1) where the low pressure is in contact to the bottom of the wafer. Each sequence of holes is connected to an airway (2). These airways connect to the four tubes connecting to the pumpon the bottom plate.

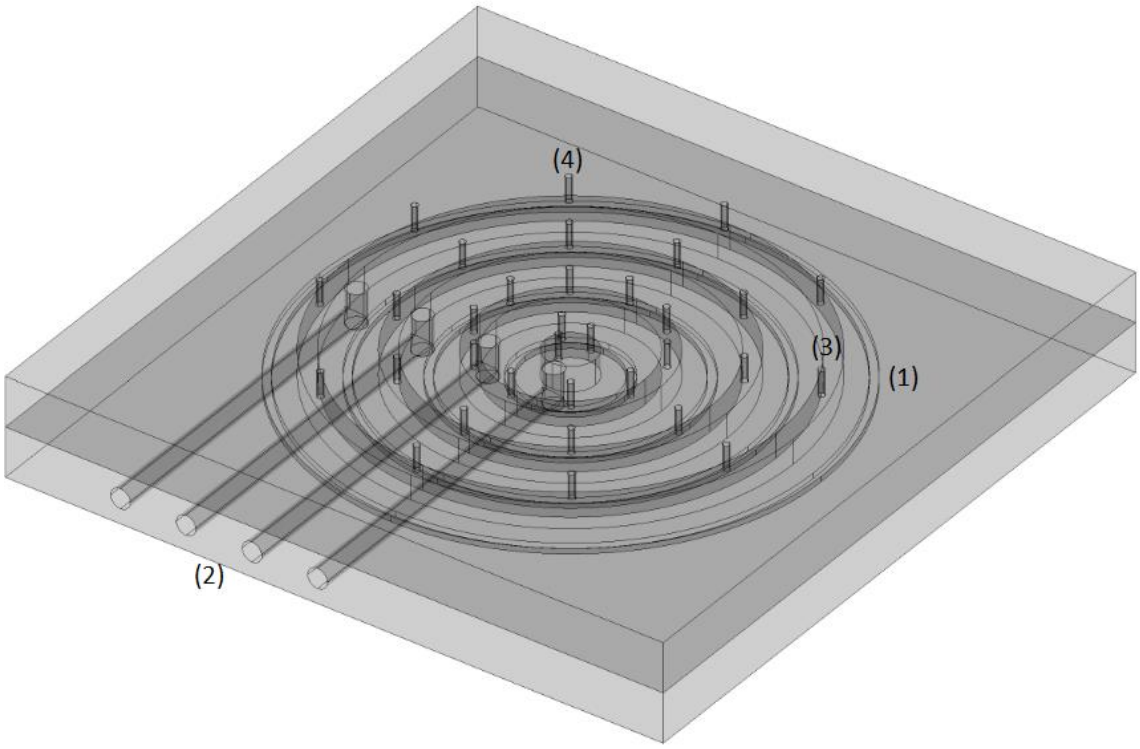

Figure 4.17 - Valves vacuum system. In this system, (1) corresponds to O-ring grooves, which prevent any leaks during operation. (2) are holes where the airways connect to the outside. Each has a ball valve, that when closed, prevents the passage of air. (3) are the airways which connect the thirty-six holes on the top (4) to the outside.

4.4. Piston

The last component designed was the piston system, Figure 4.18. This system is used to push the vacuum chuck against the electrochemical cell, so there are no problems during measurements.

The piston consists in two main parts: the stand and the shaft. The stand acts only as support and gives the appropriate height to the chuck. The shaft is the piece where the chuck will be connected. It moves horizontally to position the chuck correctly before the measurements. In the middle of the shaft exists a collar, connected to a rod, where the shaft will be placed. The chuck will be placed in the end of the shaft. A spring will be attached (5). This spring is used to maintain a constant force on the vacuum chuck. It allows for a constant compression of the O-ring on the electrochemical cell. If the compression of the O-ring is the same, then the contact area in the wafer is always the same.

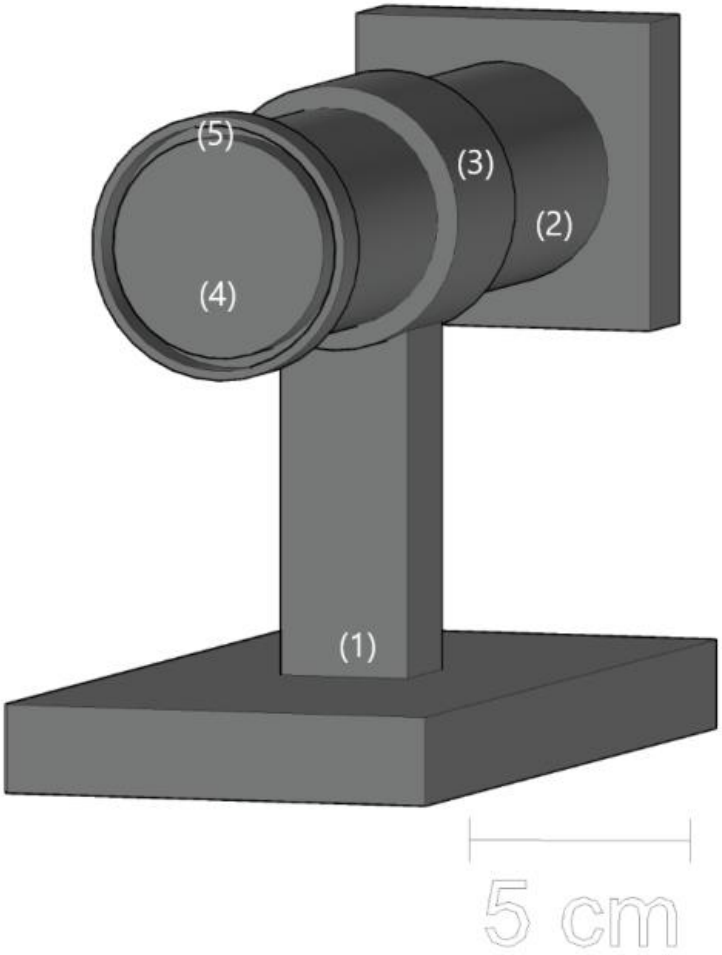

Figure 4.18 - The piston system. (1) is the stand of the piston. It gives the wafer the correct height in relation to the electrochemical cell. (2) is the shaft where the chuck connects. It can move forward and backwards to place the wafer in place. (3) is a collar, connected to a rod, where the shaft will be placed. It was a rubber ring to keep the shaft immobile during the measurements. The presence of a hinge in the back of the collar, rotates the shaft 90º. This allows for the vacuum chuck to be in a vertical position. (4) is the place where the chuck will be mounted. (5) is a small groove where a spring will be placed. It allows for a continuous force against the vacuum chuck, so that the O-ring is always compressed in the same way, keeping the contact area constant.

4.5. Complete System

The final system is shown in Figure 4.19. This figure shows the chamber with the various reservoirs (in green). In the middle of the chamber is the electrochemical cell. The O-ring holder can also be seen in the middle of the electrochemical cell. On top of the electrochemical cell, is the input reservoir where new electrolyte is introduced. Bellow the cell, is the waste reservoir, where the used electrolyte is transferred when the measurements are finished.

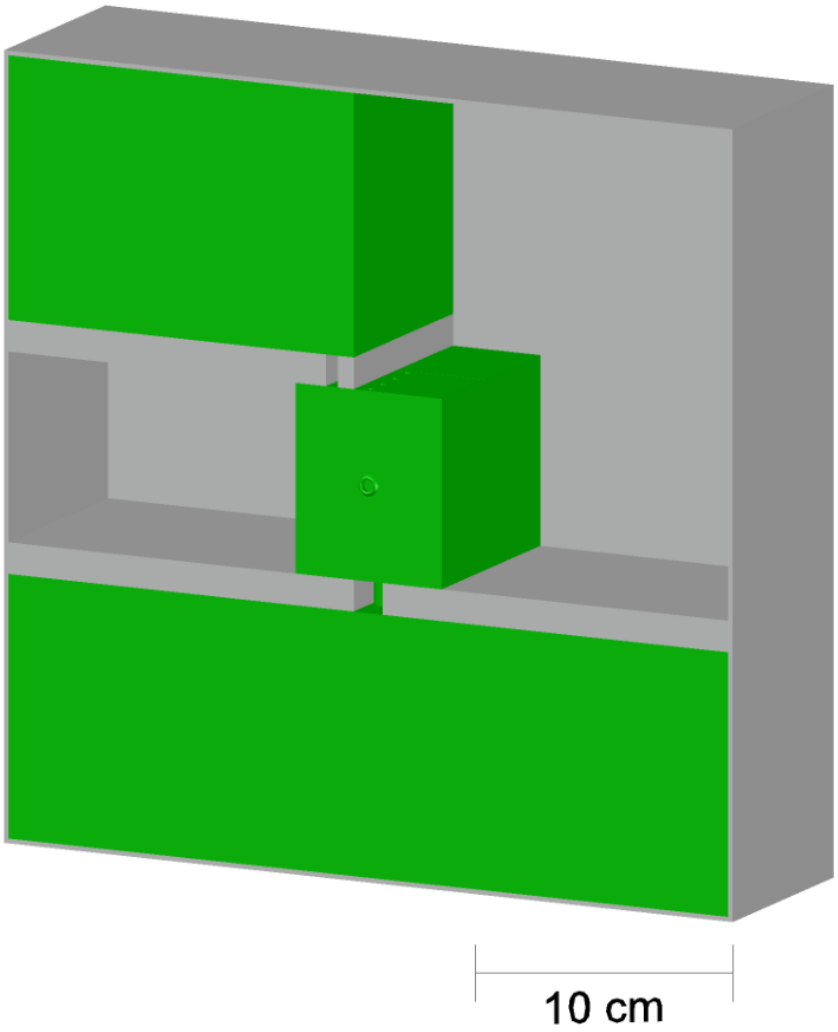

Figure 4.19 – The chamber with the various reservoirs (in green) necessary to the ECV system. In the middle, the electrochemical cell, below it the waste reservoir. Above the cell, the input reservoir.

Figure 4.20 corresponds to the vacuum chuck (in blue) attached to the piston system. The piston is the part that moves the sample closer to the electrochemical cell for the measurements. It also has a hinge in the back of the collar to rotate the shaft to a vertical position. This allows the sample to be placed horizontally on top of the vacuum chuck, before vacuum is created.

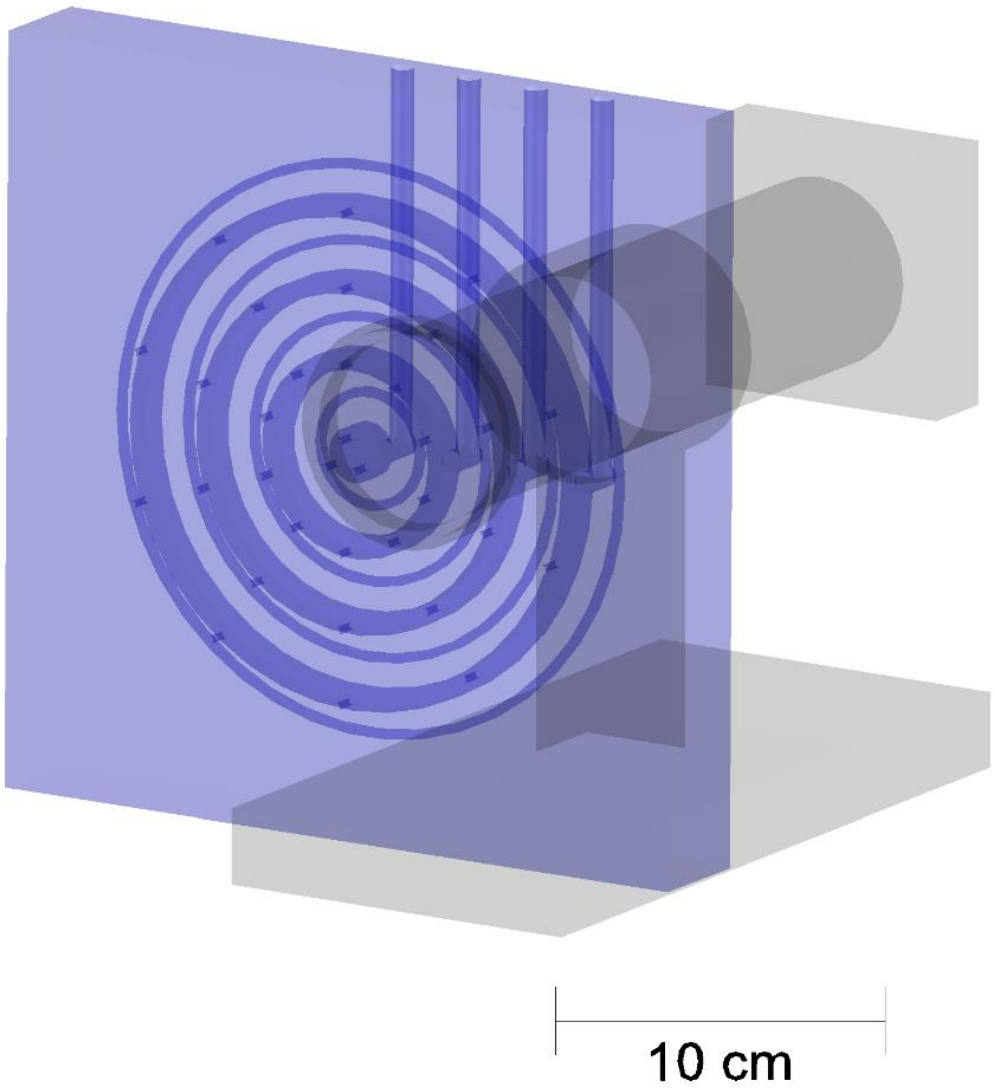

Figure 4.20 - Vacuum chuck (in blue) attached to the piston. The piston moves horizontally to bring the sample closer to the electrochemical cell.

5. Conclusion

Two different ECV systems already exist in the market today, but range from 90,000-110,000€, making it too expensive for the S- LoTTuSS research project.

The designed final system was designed to do doping profiling through electrochemical means, focusing on compatibility. The designed vacuum chuck can hold wafers with dimensions between 2.5 mm radius and 80 mm radius. When the chuck is holding smaller wafers, the necessary safety precautions have to be made, since the electrolyte is a hazardous liquid to humans.

One of the thought-out mechanisms was moving the wafer to be able to measure different places in it. One way was using an x-y moving table on the back of the chuck. A proposed method is using the vertical part of the stand in the piston to move the wafer up and down, by hollowing it out and creating a vertical rod, connected to the collar, which will enter the vertical part of the stand, and later rotating the wafer according to the location of the doped region.

The vacuum chuck to be used is probably the valves vacuum system. This system is more user friendly, because it is not necessary to open the chuck to change the usable airways. The usable airways can be changed with the attached valves. O-ring grooves were designed between the two layers of aluminium, to prevent any leaks between the two layers of aluminium.

It is also necessary to think about the materials for the different parts. The electrochemical cell is constructed of PTFE, with the O-ring between the electrochemical cell and the wafer in PVC or PTFE. Also, the vacuum chuck is made of aluminium. The material for the O-rings is not decided yet, but a fluorocarbon, such as Viton, is suggested.

After the system is constructed, some tests will be needed to guarantee that the system is adequate for the measurements. The tests are leakproof, electrical connections and etching. After the tests, calibration of the system is also required.

The leakproof test consist of introducing liquid inside of the electrochemical cell to check for any leaks. The next test is confirming that the electrodes are functioning properly. An electrolyte is introduced in the cell, the electrodes connected, and a voltage applied between the carbon and the electrode in the sample. Then, the AutoLab® potentiostat measures the current and voltage on the system. Finally, the etching test, where etching of the wafer's surface is made, while measuring the etched depth. To calibrate the system, the results from the designed ECV system are compared to the results obtained through ECV and SIMS systems in other laboratories.

To finalize the whole process, it is necessary to write the procedure manual for the system, explaining how to use the system, including any safety requirements of the system.

6. Bibliography

[1] W. Shockley and H. J. Queisser, "Detailed Balance Limit of Efficiency of p-n Junction Solar Cells," *J. Appl. Phys.*, vol. 32, no. 3, pp. 510–519, Mar. 1961, doi: 10.1063/1.1736034.

[2] A. Richter, M. Hermle, and S. W. Glunz, "Reassessment of the Limiting Efficiency for Crystalline Silicon Solar Cells," *IEEE J. Photovoltaics*, vol. 3, no. 4, pp. 1184–1191, Oct. 2013, doi: 10.1109/JPHOTOV.2013.2270351.

[3] A. Luque and S. Hegedus, *Handbook of Photovoltaic Science and Engineering*. 2011.

[4] S. Rühle, "Tabulated values of the Shockley-Queisser limit for single junction solar cells," *Sol. Energy*, vol. 130, pp. 139–147, 2016, doi: 10.1016/j.solener.2016.02.015.

[5] P. R. I. F. O. R. S. E. S. ISE, "Photovoltaics Report," no. September, 2020.

[6] M. A. Green *et al.*, "Solar cell efficiency tables (Version 53)," *Prog. Photovoltaics Res. Appl.*, vol. 27, no. 1, pp. 3–12, Jan. 2019, doi: 10.1002/pip.3102.

[7] J. Zheng *et al.*, "21.8% Efficient Monolithic Perovskite/Homo-Junction-Silicon Tandem Solar Cell on 16 cm 2," *ACS Energy Lett.*, vol. 3, no. 9, pp. 2299–2300, Sep. 2018, doi: 10.1021/acsenergylett.8b01382.

[8] Y. Deshayes and L. Béchou, "State-of-the-Art of Infrared Technology," *Reliab. Robustness Fail. Mech. LED Devices*, pp. 1–44, 2016, doi: 10.1016/b978-1-78548-152-9.50001-8.

[9] T. Mueller, J. Wong, and A. G. Aberle, "Heterojunction Silicon Wafer Solar Cells using Amorphous Silicon Suboxides for Interface Passivation," *Energy Procedia*, vol. 15, pp. 97–106, 2012, doi: 10.1016/j.egypro.2012.02.012.

[10] Gaspar G *et al.*, "Interconexão entre células solares de perovskita e silício em dispositivos monolíticos tandem de 2 terminais: Estado da arte e desenvolvimentos futuros," *CIES2020 - XVII Congr. Ibérico e XIII Congr. Ibero-americano Energ. Sol.*, pp. 413–419, 2020, doi: 10.34637/cies2020.1.2047.

[11] J. Werner *et al.*, "Efficient Near-Infrared-Transparent Perovskite Solar Cells Enabling Direct Comparison of 4-Terminal and Monolithic Perovskite/Silicon Tandem Cells," *ACS Energy Lett.*, vol. 1, no. 2, pp. 474–480, 2016, doi: 10.1021/acsenergylett.6b00254.

[12] M. Jošt, L. Kegelmann, L. Korte, and S. Albrecht, "Monolithic Perovskite Tandem Solar Cells: A Review of the Present Status and Advanced Characterization Methods Toward 30% Efficiency," *Adv. Energy Mater.*, vol. 10, no. 26, 2020, doi: 10.1002/aenm.201904102.

[13] N. N. Lal, Y. Dkhissi, W. Li, Q. Hou, Y. B. Cheng, and U. Bach, "Perovskite Tandem Solar Cells," *Adv. Energy Mater.*, vol. 7, no. 18, pp. 1–18, 2017, doi: 10.1002/aenm.201602761.

[14] D. Wang, M. Wright, N. K. Elumalai, and A. Uddin, "Stability of perovskite solar cells," *Sol. Energy Mater. Sol. Cells*, vol. 147, pp. 255–275, 2016, doi: 10.1016/j.solmat.2015.12.025.

[15] A. De Vos, "Detailed balance limit of the efficiency of tandem solar cells," *J. Phys. D. Appl. Phys.*, vol. 13, no. 5, pp. 839–846, 1980, doi: 10.1088/0022-3727/13/5/018.

[16] M. I. Hossain, W. Qarony, S. Ma, L. Zeng, D. Knipp, and Y. H. Tsang, "Perovskite/Silicon Tandem Solar Cells: From Detailed Balance Limit Calculations to Photon Management," *Nano-Micro Lett.*, vol. 11, no. 1, 2019, doi: 10.1007/s40820-019-0287-8.

[17] B. M. Kayes *et al.*, "27.6% Conversion efficiency, a new record for single-junction solar cells under 1 sun illumination," *Conf. Rec. IEEE Photovolt. Spec. Conf.*, pp. 000004–000008, 2011, doi: 10.1109/PVSC.2011.6185831.

[18] P. Colter, B. Hagar, and S. Bedair, “Tunnel junctions for III-V multijunction solar cells review,” *Crystals*, vol. 8, no. 12, 2018, doi: 10.3390/cryst8120445.

[19] L. Esaki, “New phenomenon in narrow germanium p-n junctions [3],” *Phys. Rev.*, vol. 109, no. 2, pp. 603–604, 1958, doi: 10.1103/PhysRev.109.603.

[20] K. Krane, *Modern Physics*, Third Edit., vol. 4, no. 1. John Wiley & Sons, Inc., 2012.

[21] A. F. D. Guerra, “Fabrico de junções de túnel para células solares de dupla junção de alto rendimento Afonso Filipe Diogo Guerra,” University of Liabon, 2020.

[22] S. M. Iftiquar, Y. Lee, M. Ju, N. Balaji, S. Kumar, and J. Yi, “Fabrication of Crystalline Silicon Solar Cell with Emitter Diffusion, SiNx Surface Passivation and Screen Printing of Electrode,” in *Photodiodes - From Fundamentals to Applications*, vol. 395, no. tourism, InTech, 2012, pp. 116–124.

[23] S. A. Schwarz, “Secondary Ion Mass Spectroscopy,” *Encycl. Mater. Sci. Technol.*, pp. 8283–8290, 2001, doi: 10.1016/b0-08-043152-6/01482-0.

[24] B. L. Sharma, Ed., *Metal-Semiconductor Schottky Barrier Junctions and Their Applications*. Boston, MA: Springer US, 1984.

[25] X. G. Zhang, *Electrochemistry of silicon and its oxide*. New York: Kluwer Academic Publishers, 2004.

[26] T. Ambridge and M. M. Faktor, “An automatic carrier concentration profile plotter using an electrochemical technique,” *J. Appl. Electrochem.*, vol. 5, no. 4, pp. 319–328, Nov. 1975, doi: 10.1007/BF00608796.

[27] D. K. Schroder, “Frontmatter,” in *Semiconductor Material and Device Characterization*, Hoboken, NJ, USA: John Wiley & Sons, Inc., 2005, pp. i–xv.

[28] P. Blood, “Capacitance-voltage profiling and the characterisation of III-V semiconductors using electrolyte barriers,” *Semicond. Sci. Technol.*, vol. 1, no. 1, pp. 7–27, Jul. 1986, doi: 10.1088/0268-1242/1/1/002.

[29] C. D. Sharpe, “The Electrolyte-Silicon Interface; Anodic Dissolution and Carrier Concentration Profiling,” *J. Electrochem. Soc.*, vol. 127, no. 9, p. 1918, 1980, doi: 10.1149/1.2130036.

[30] W. Y. Leong, R. A. A. Kubiak, and E. H. C. Parker, “DOPANT PROFILING OF Si-MBE MATERIAL USING THE ELECTROCHEMICAL CV TECHNIQUE.,” in *Proceedings - The Electrochemical Society*, 1985, vol. 85–7, pp. 140–149.

[31] T. Wolff, M. Rapp, and T. Rotter, “Electrochemical etching and CV-profiling of GaN,” *Phys. Status Solidi Appl. Res.*, vol. 201, no. 9, pp. 2067–2075, 2004, doi: 10.1002/pssa.200406829.

[32] A. Saraei, M. J. Eshraghi, F. Tajabadi, and A. Massoudi, “ECV Doping Profile Measurements in Silicon Using Conventional Potentiostat,” *J. Electron. Mater.*, vol. 47, no. 12, pp. 7309–7315, Dec. 2018, doi: 10.1007/s11664-018-6670-2.

[33] G. Yakovlev, V. Zubrov, A. Solomnikova, and O. Derevianko, “Electrochemical capacitance-voltage profiling of nonuniformly doped GaAs heterostructures with SQWs and MQWs for LED applications,” *TURKISH J. Phys.*, vol. 42, no. 4, pp. 433–442, Aug. 2018, doi: 10.3906/fiz-1803-23.

[34] E. Başaran, “Choice of electrolyte for doping profiling in Si by electrochemical C-V technique,” *Appl. Surf. Sci.*, vol. 172, no. 3–4, pp. 345–350, 2001, doi: 10.1016/S0169-4332(00)00871-0.

[35] A. Halimaoui, “Determination of the specific surface area of porous silicon from its etch rate in HF solutions,” *Surf. Sci.*, vol. 306, no. 1–2, 1994, doi: 10.1016/0039-6028(94)91176-2.

[36] E. Peiner, “Anodic Dissolution during Electrochemical Carrier-Concentration Profiling of Silicon,” *J. Electrochem. Soc.*, vol. 139, no. 2, p. 552, 1992, doi: 10.1149/1.2069255.

[37] L. Liu, F. Lin, M. Heinrich, A. G. Aberle, and B. Hoex, “Unexpectedly High Etching Rate of Highly Doped n-Type Crystalline Silicon in Hydrofluoric Acid,” *ECS J. Solid State Sci. Technol.*, vol. 2, no. 9, pp. P380–P383, 2013, doi: 10.1149/2.026309jss.

[38] S. M. Hu and D. R. Kerr, “Observation of Etching of n-Type Silicon in Aqueous HF Solutions,” *J. Electrochem. Soc.*, vol. 114, no. 4, p. 414, 1967, doi: 10.1149/1.2426612.

[39] “4. Real-space surface profiling techniques,” *Exp. Methods Phys. Sci.*, vol. 37, no. C, pp. 63–82, 2001, doi: 10.1016/S1079-4042(01)80059-X.

[40] X. G. Zhang, “Electrochemistry of Silicon Etching,” in *Encyclopedia of Electrochemistry*, Wiley, 2007, pp. 751–808.

[41] V. Lehmann, *Electrochemistry of Silicon*, vol. 3. Wiley, 2002.

[42] M. Matsumura and H. Fukidome, “Enhanced Etching Rate of Silicon in Fluoride Containing Solutions at pH 6.4,” *J. Electrochem. Soc.*, vol. 143, no. 8, pp. 2683–2686, Aug. 1996, doi: 10.1149/1.1837071.

[43] W. Kern and C. A. Deckert, *Chemical Etching*. ACADEMIC PRESS, INC., 1978.

[44] R. Memming and G. Schwandt, “Anodic dissolution of silicon in hydrofluoric acid solutions,” *Surf. Sci.*, vol. 4, no. 2, pp. 109–124, 1966, doi: 10.1016/0039-6028(66)90071-9.

[45] H.-J. Riedl and J. Dahmlos, “Ammonium Bifluoride,” 3005684, 2007.

[46] E. Basaran, C. P. Parry, R. A. Kubiak, T. E. Whall, and E. H. C. Parker, “Electrochemical capacitance-voltage depth profiling of heavily boron-doped silicon,” *J. Cryst. Growth*, vol. 157, no. 1–4, pp. 109–112, Dec. 1995, doi: 10.1016/0022-0248(95)00397-5.

[47] J. F. O’Hanlon, *A User’s Guide to Vacuum Technology*, vol. 40. Wiley, 2003.

[48] G. A. Wardly, “Electrostatic wafer chuck for electron beam microfabrication,” *Rev. Sci. Instrum.*, vol. 44, no. 10, pp. 1506–1509, 1973, doi: 10.1063/1.1685985.

[49] V. Lehmann and H. Föll, “Formation Mechanism and Properties of Electrochemically Etched Trenches in n-Type Silicon,” *J. Electrochem. Soc.*, vol. 137, no. 2, pp. 653–659, 1990, doi: 10.1149/1.2086525.

[50] E. Peiner, “Doping Profile Analysis in Si by Electrochemical Capacitance-Voltage Measurements,” *J. Electrochem. Soc.*, vol. 142, no. 2, p. 576, 1995, doi: 10.1149/1.2044101.

[51] R. Kinder, “Profiling of the p-n junction in silicon by the electrochemical capacitance-voltage technique,” *Phys. Status Solidi Appl. Res.*, vol. 169, no. 2, pp. 261–265, 1998, doi: 10.1002/(SICI)1521-396X(199810)169:2<261::AID-PSSA261>3.0.CO;2-Z.

[52] V. Gopal, E. H. Chen, E. P. Kvam, and J. M. Woodall, “Electrochemical capacitance voltage profiling of the narrow band gap semiconductor InAs,” *J. Electron. Mater.*, vol. 29, no. 11, pp. 1333–1339, Nov. 2000, doi: 10.1007/s11664-000-0134-0.

[53] R. Kinder, J. Breza, F. Mika, and A. Grmanov, “Communications Anodic Dissolution of Silicon By Electrochemical Carrier Concentration Profiling,” vol. 53, no. 3, pp. 97–100, 2002.

[54] R. Bock, P. P. Altermatt, and J. Schmidt, “Accurate Extraction of Doping Profiles from Electrochemical Capacitance Voltage Measurements,” *Contract*, no. September, pp. 21–24, 2008, doi: 10.4229/23rdEUPVSEC2008-2CV.4.56.

[55] H. Wu *et al.*, “Electrochemical capacitance-voltage characterization of plasma-doped ultra-shallow junctions,” *Front. Electr. Electron. Eng. China*, vol. 3, no. 1, pp. 116–119, 2008, doi: 10.1007/s11460-008-0016-4.

[56] Y. Komatsu *et al.*, “Calibration of electrochemical capacitance-voltage method on pyramid texture surface using scanning electron microscopy,” *Energy Procedia*, vol. 38, pp. 94–100, 2013, doi: 10.1016/j.egypro.2013.07.254.

[57] D. S. Frolov and V. I. Zubkov, “Frequency dispersion of capacitance–voltage characteristics in wide bandgap semiconductor-electrolyte junctions,” *Semicond. Sci. Technol.*, vol. 31, no. 12, p. 125013, Dec. 2016, doi: 10.1088/0268-1242/31/12/125013.

[58] B. Sermage *et al.*, “Electrochemical capacitance voltage measurements in highly doped silicon and silicon-germanium alloys,” *J. Appl. Phys.*, vol. 119, no. 15, p. 155703, Apr. 2016, doi: 10.1063/1.4946890.

[59] D. S. Frolov, G. E. Yakovlev, and V. I. Zubkov, “Technique for the Electrochemical Capacitance–Voltage Profiling of Heavily Doped Structures with a Sharp Doping Profile,” *Semiconductors*, vol. 53, no. 2, pp. 268–272, Feb. 2019, doi: 10.1134/S1063782619020076.

[60] PubChem, “4,5-Dinitrosobenzene-1,3-disulfonic acid.” [Online]. Available: https://pubchem.ncbi.nlm.nih.gov/compound/4_5-Dinitrosobenzene-1_3-disulfonic-acid#section=Information-Sourceshttps://pubchem.ncbi.nlm.nih.gov/compound/4_5-Dinitrosobenzene-1_3-disulfonic-acid%23section=Information-Sources.

7. Annex

7.1. Annex A

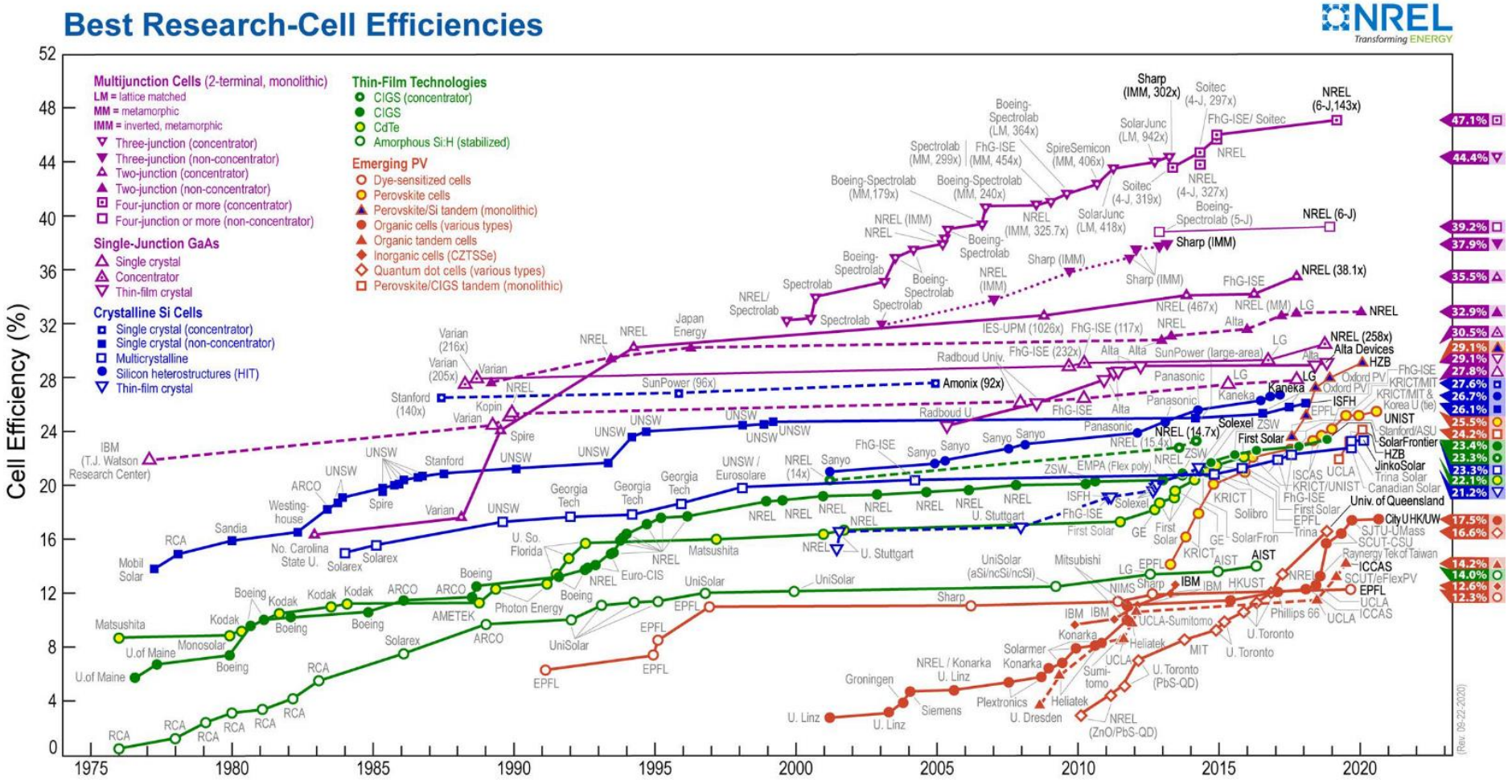

Figure 7.1 - Best Research-Cell Efficiencies. (Revision 2020-12-28 [3])

Table 7-1 - Table with experiments from different authors. It mentions the used cell, the electrolyte used during the ECV profiling, the dopants used in the wafer (if mentioned), and the etch rates (if indicated)

Reference	Cell	Electrolyte	Dopant	Etch Rate (nm/min)
Memming 1966 [44]	p and n type Si	$NH_4F{\cdot}HF$	Not mentioned	Not indicated
Hu 1967 [38]	N-type Si	HF	Not mentioned	0.03
Ambridge 1975 [26]	n-type GaAs	KOH	Not mentioned	33
Sharpe 1980 [29]	p and n-type Si	$NaF{\cdot}H_2SO_4$	Not mentioned	Not indicated
Lehmann 1990 [49]	n-type Si	HF	Not mentioned	600
Peiner 1992 [36]	p and n-type Si	$NH_4F{\cdot}HF$	Not mentioned	33-67
Basaran 1995 [46]	p-type Si	$NaF{\cdot}H_2SO_4$	Boron	Not indicated
Peiner 1995 [50]	p and n-type Si	$NH_4F{\cdot}HF$	Boron and Phosphorus	Not indicated
Kinder 1998 [51]	p and n-type Si	$NH_4F{\cdot}HF$	Not mentioned	Not indicated
Gopal 2000 [52]	p and n-type InAs	EDTA+NaOH+ED	Beryllium and Silicon	Not indicated
Basaran 2001 [34]	p-type Si	$NH_4F{\cdot}HF$ $NaF{\cdot}H_2SO_4$	Not mentioned	Not indicated
Kinder 2002 [53]	p-type Si	$NH_4F{\cdot}HF$	Boron	Not indicated
Wolff 2004 [31]	p and n-type GaN	KOH	Not mentioned	47
Bock 2008 [54]	p and n-type Si	$NH_4F{\cdot}HF$	Boron and Phosphorus	Not indicated
Wu 2008 [55]	p and n-type Si	$NaF{\cdot}H_2SO_4$	Not mentioned	Not indicated

Liu 2013 [37]	p-type Si	HF	Phosphorus	1.2
Komatsu 2013 [56]	p and n-type Si	$NH_4F{\cdot}HF$	Boron	Not indicated
Frolov 2016 [57]	p and n-type SiC p and n-type GaN p-type semiconductor diamond	$NH_4F{\cdot}HF$	SiC – alluminium GaN – Magnesium Diamond - Boron	Not indicated
Sermage 2016 [58]	SiGe – n-type Si, Ge epitaixally grown n-type Si	50% $NH_4F{\cdot}HF$ + 50% HCl	Boron	Not indicated
Saraei 2018 [32]	p-type Si	NH_4F	Phosphorus	5.5-10
Yakovlev 2018 [33]	p-type GaAs	Tiron	Not mentioned	Not indicated
Frolov 2019 [59]	p-type Si n-type GaAs	Si - $NH_4F{\cdot}HF$ GaAs - Tiron	Not mentioned	Not indicated

7.2. Annex B – ECV cell

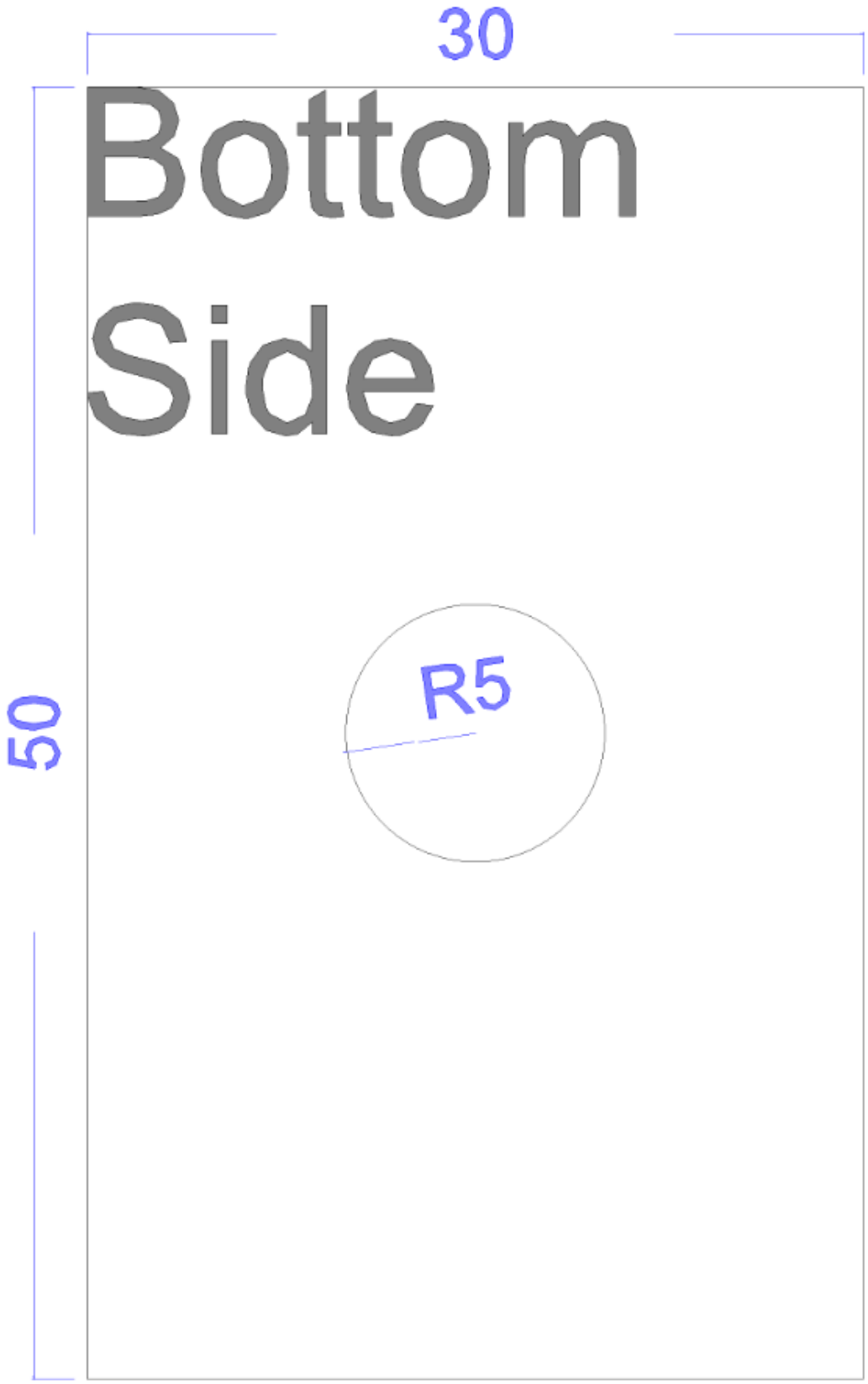

Figure 7.2 - Bottom side of the electrochemical cell. It has a 5 mm radius orifice in the middle to remove the electrolyte, after the measurements are done. The electrolyte must be removed before separating the sample from the electrochemical cell.

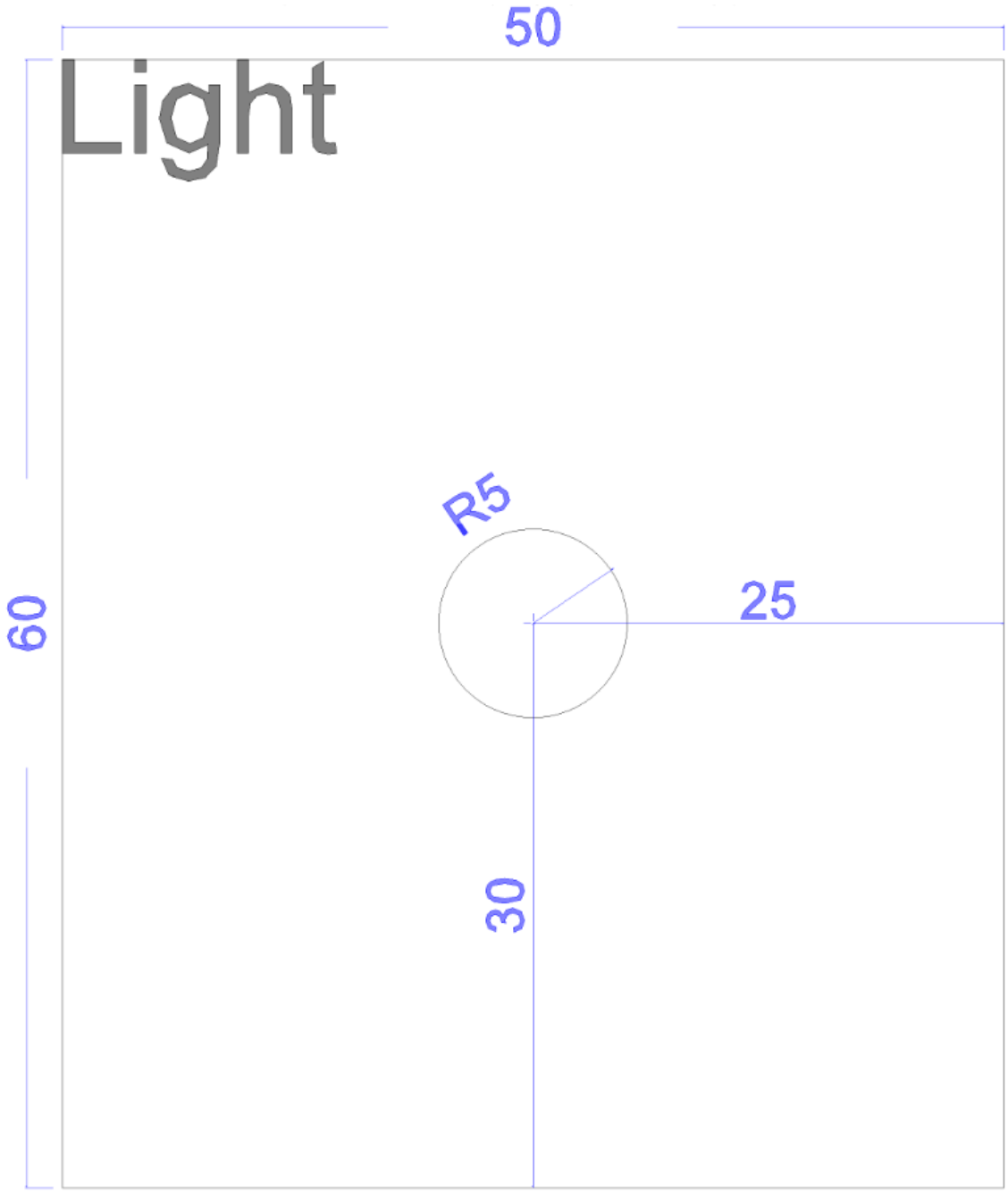

Figure 7.3 - Light side of the electrochemical cell. It has a 5 mm radius orifice, where light enters to illuminate the sample during n-type etching.

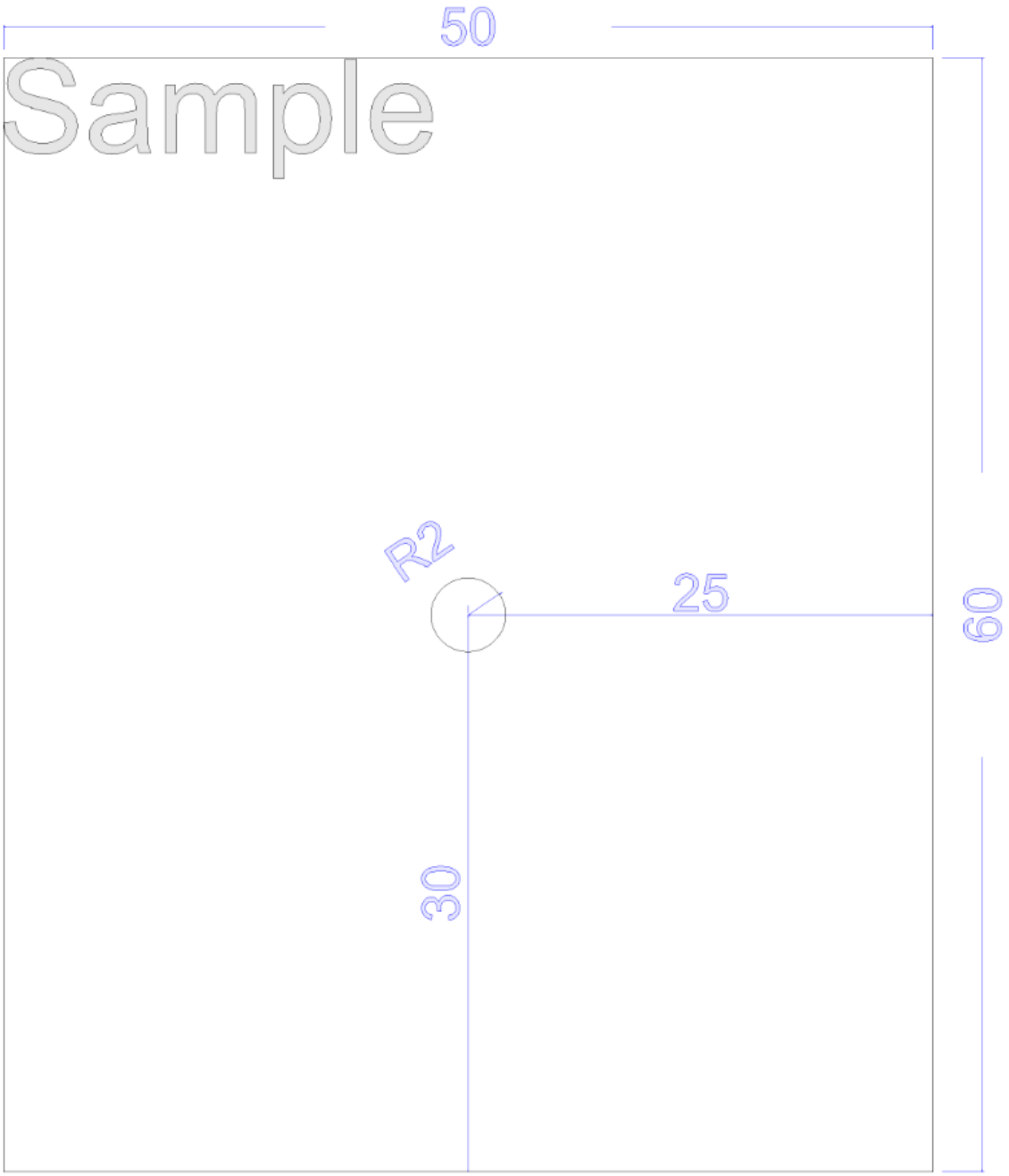

Figure 7.4 - Sample side of the electrochemical cell. The orifice in the middle has a radius of 2 mm. It has an attachment with an O-ring that defines the contact area.

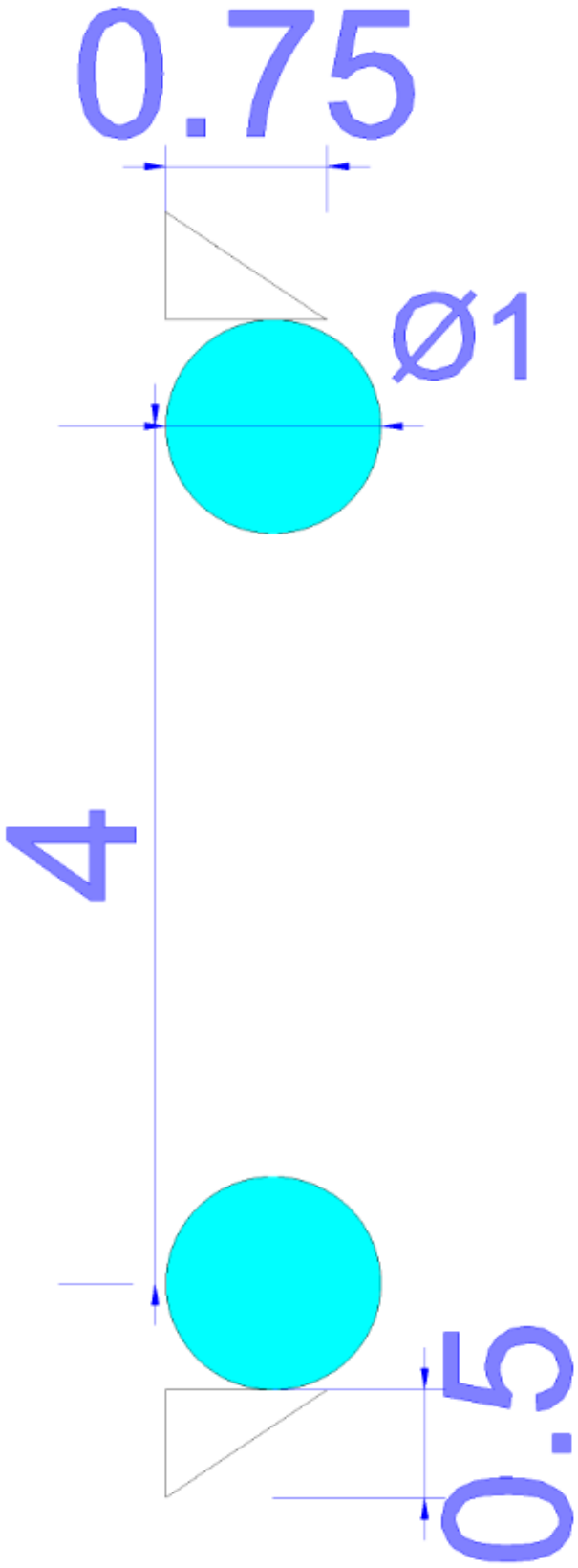

Figure 7.5 - O-ring attachment. O-ring in cyan. The desired contact area is 4 mm. The O-ring has a 3 mm inside diameter and a 1 mm cross section. The attachment has a height of 75% of the O-ring's cross section, to prevent the O-ring from moving.

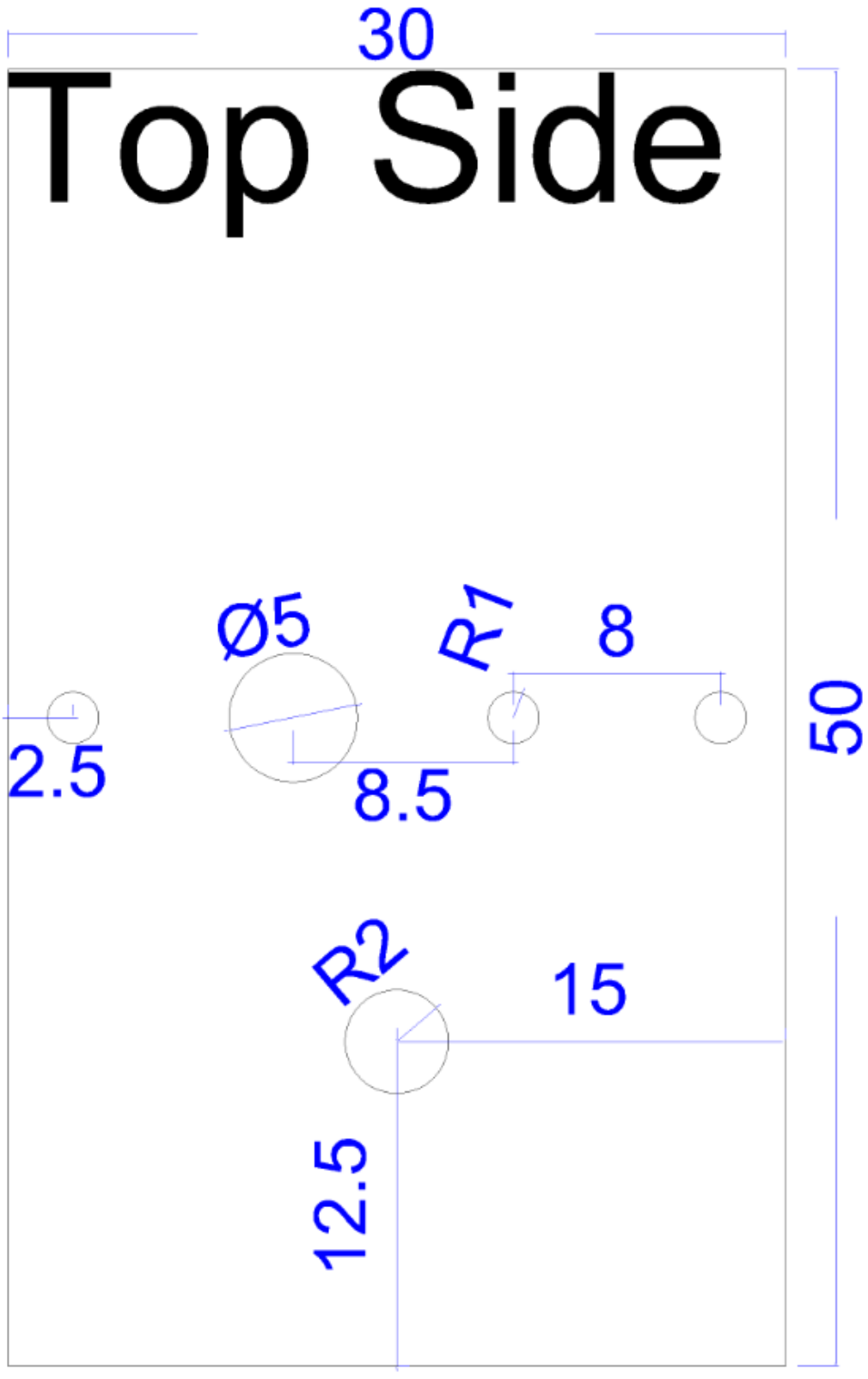

Figure 7.6 - Top of the three electrode electrochemical cell. In the middle exists four orifices 8.5 mm apart and 2.5 mm from the sides. Three for the electrodes and one four pump. The orifice bellow, with 2 mm radius, is to fill the electrochemical cell with the electrolyte. This part was based in the needs of the electrochemical cell, one carbon electrode, one reference electrode and a platinum electrode.

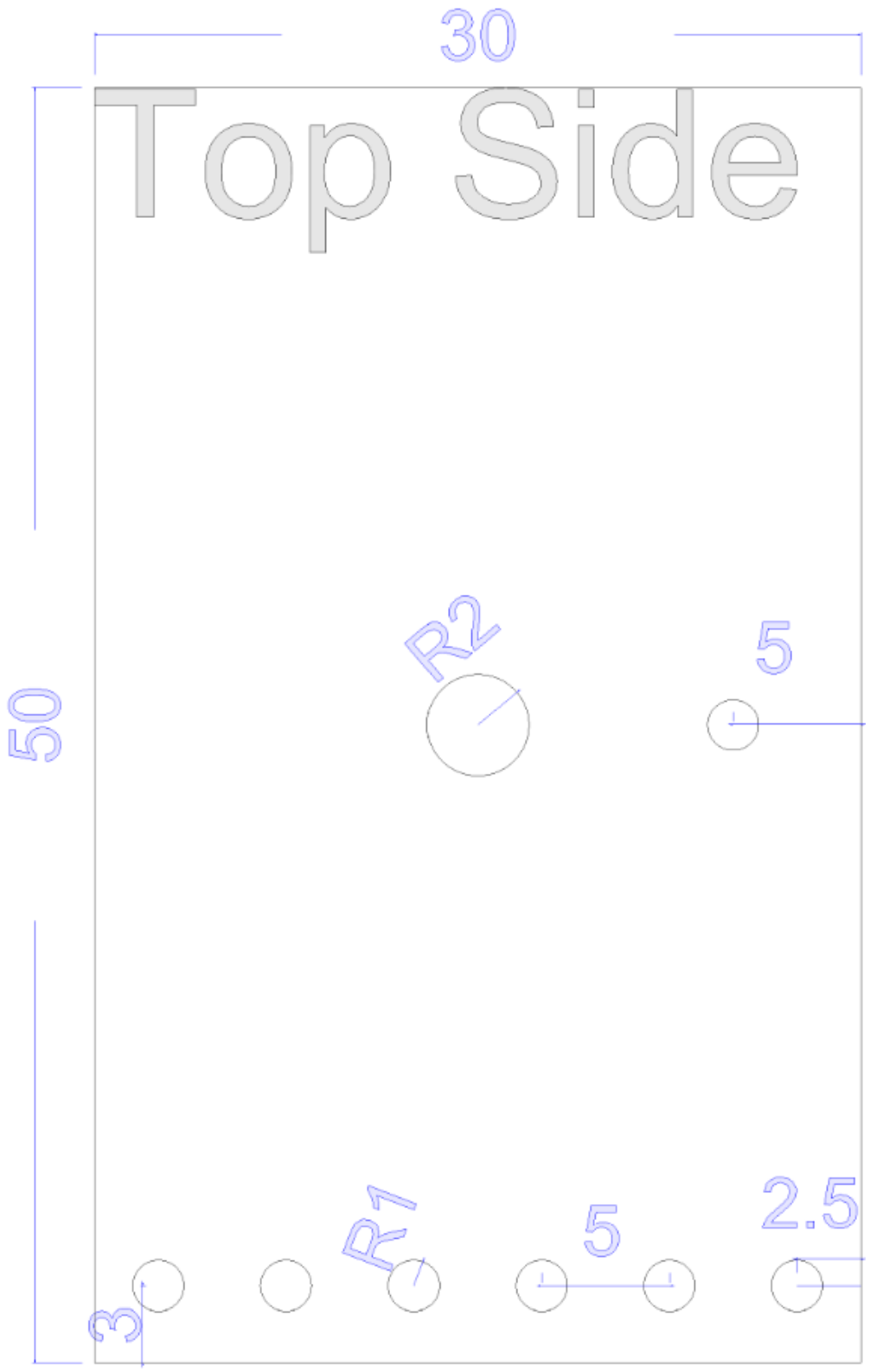

Figure 7.7 - Top of the six-electrode electrochemical cell. In the middle a 2 mm radius orifice, for the filing of the electrochemical cell exists. An orifice for the pump exists, 5 mm away from the side, in the middle right side. In the lower part of the figure, 3 mm from the side, are six orifices, with 1 mm radius, 5 mm apart. This part was based in the commercial electrochemical cell, existing today.

7.3. Annex C – Vacuum chuck

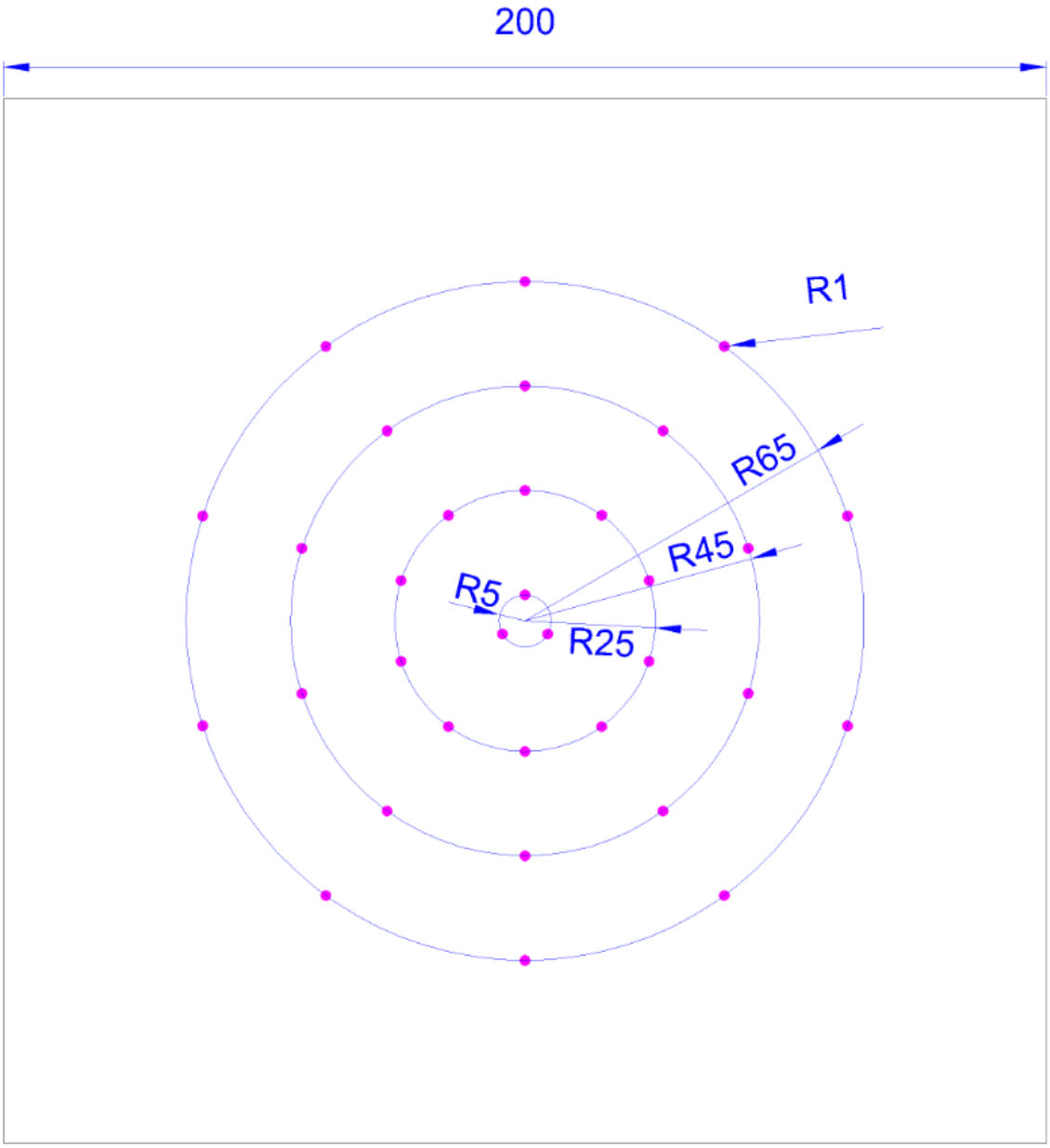

Figure 7.8 - Top layer of the O-ring vacuum chuck. Consist of a 200 mm x 200 mm square with thirty-six orifices (in pink). Each orifice has a 1 mm radius, where the sample will be pushed against. Each of the sequences of holes are 20 mm apart, starting at 5 mm from the centre of the layer.

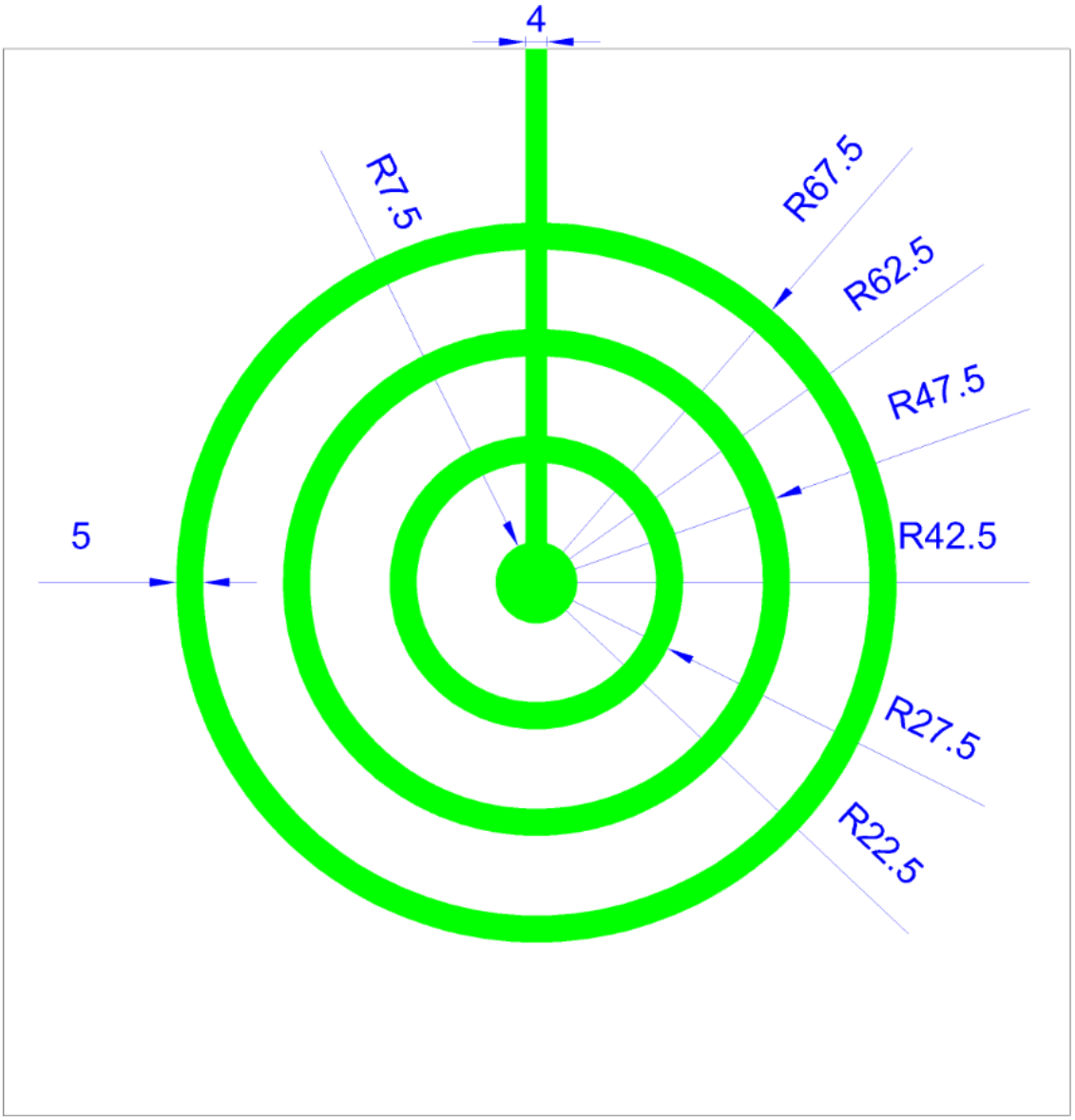

Figure 7.9 - Bottom layer of the O-ring vacuum system. Three grooves are designed with 5 mm thickness spread apart 20 mm, starting 7.5 mm from the centre. The connecting groove to the outside has 4 mm thickness.

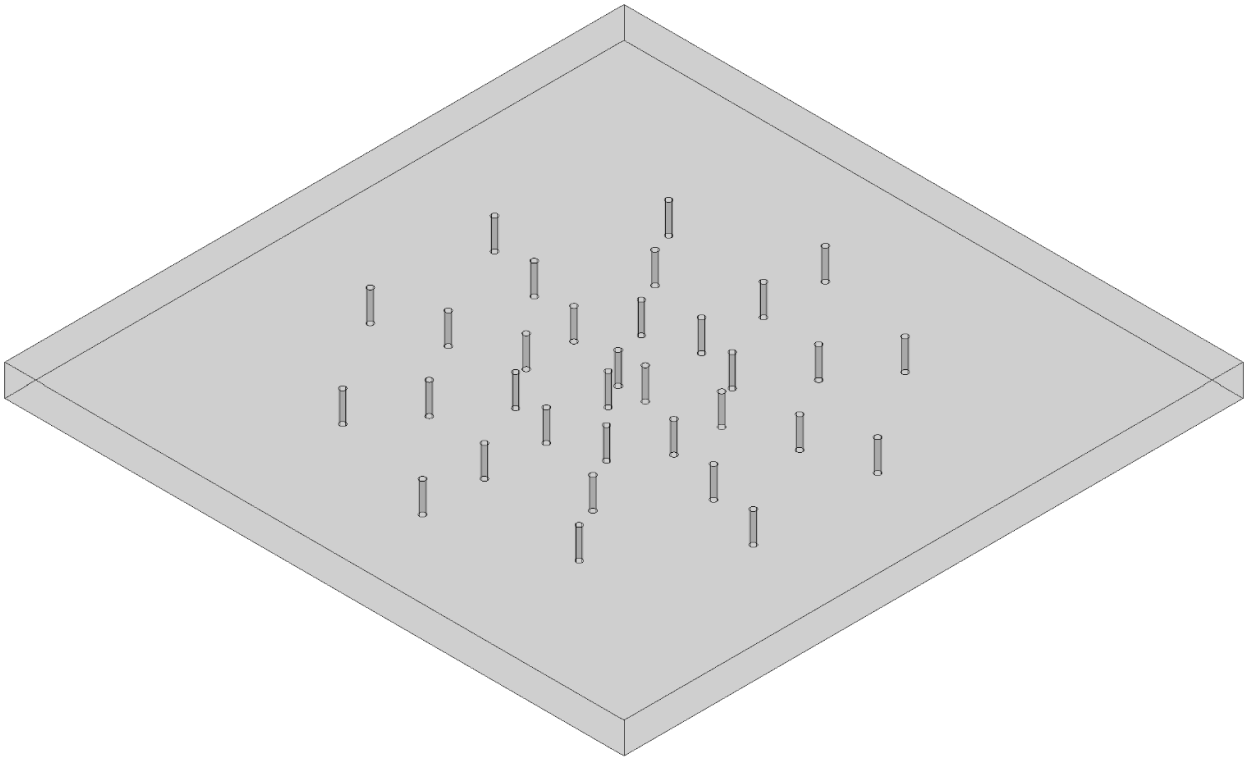

Figure 7.10 - 3D version of the top of the O-ring vacuum system.

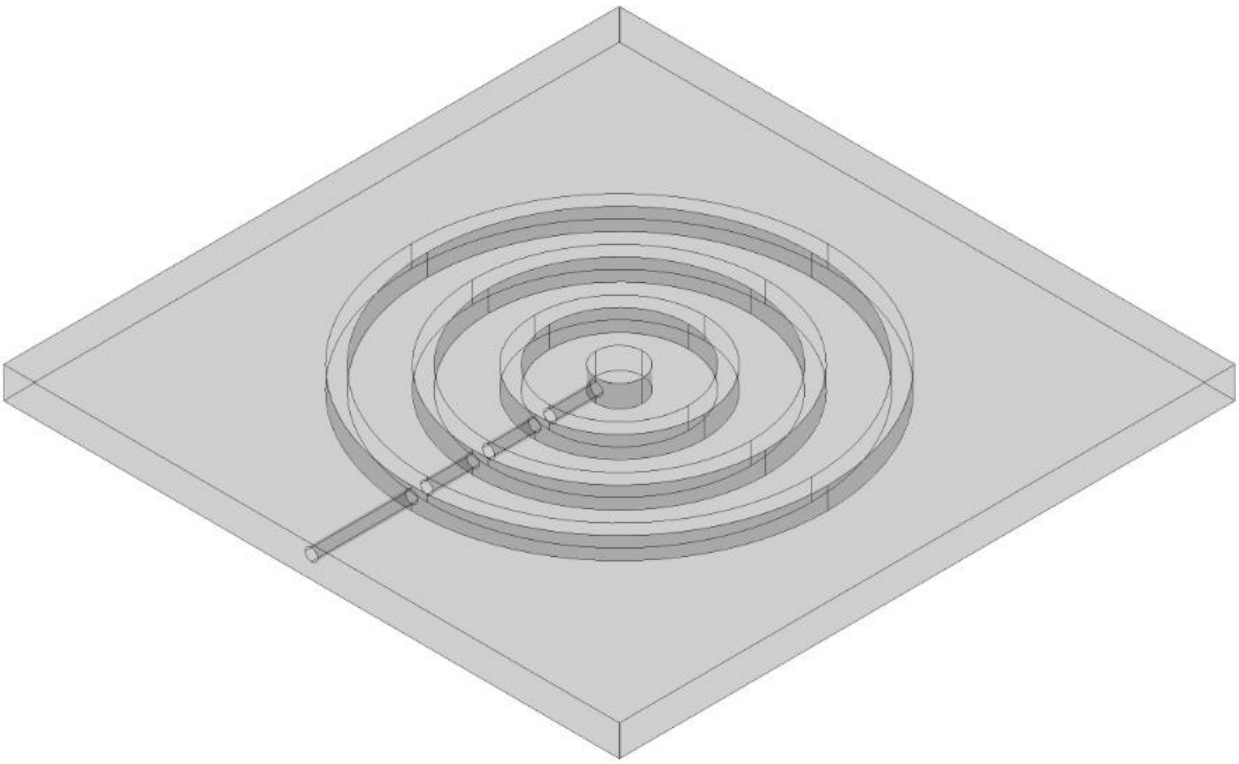

Figure 7.11 - 3D version of the bottom layer of the O-ring vacuum system.

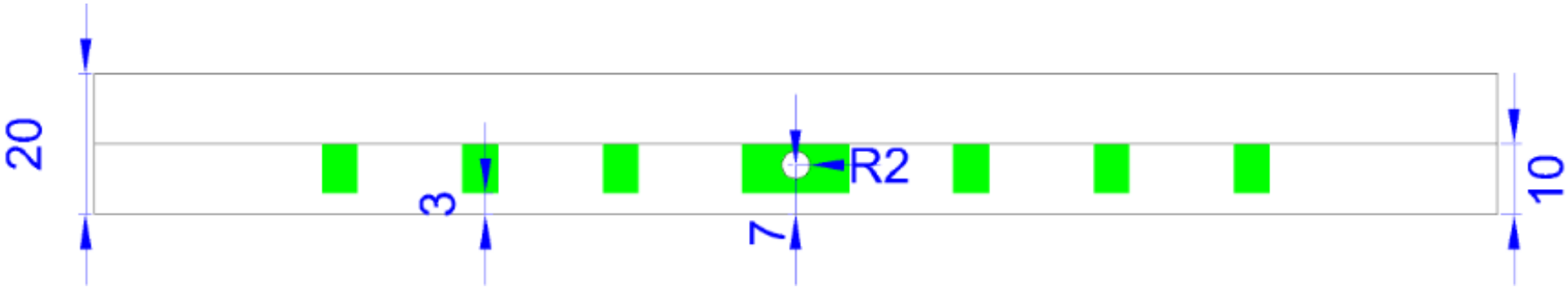

Figure 7.12 - O-ring vacuum system from the side. Each layer is 10 mm thick. In green are the grooves, 7 mm deep. The outside connecting groove is 7 mm above the bottom of the layer.

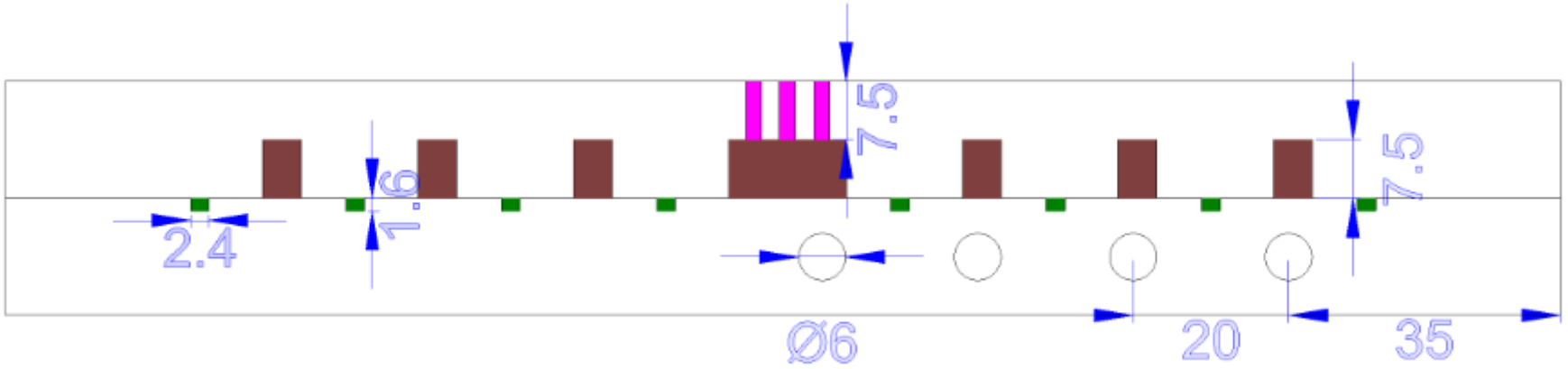

Figure 7.13 - Valve vacuum system from the side. Each layer is 15 mm thick. In dark green are the O-ring grooves to prevent leaks, these are 2.4x1.6 mm, values corrected for 20% compression. In brown, the air grooves, 7.5 mm thick. The opening for valves, with 3 mm radius, 35 mm from the side and 20 mm apart. Lastly, in pink at the top, three of the thirty-six holes, also 7.5 mm thick.

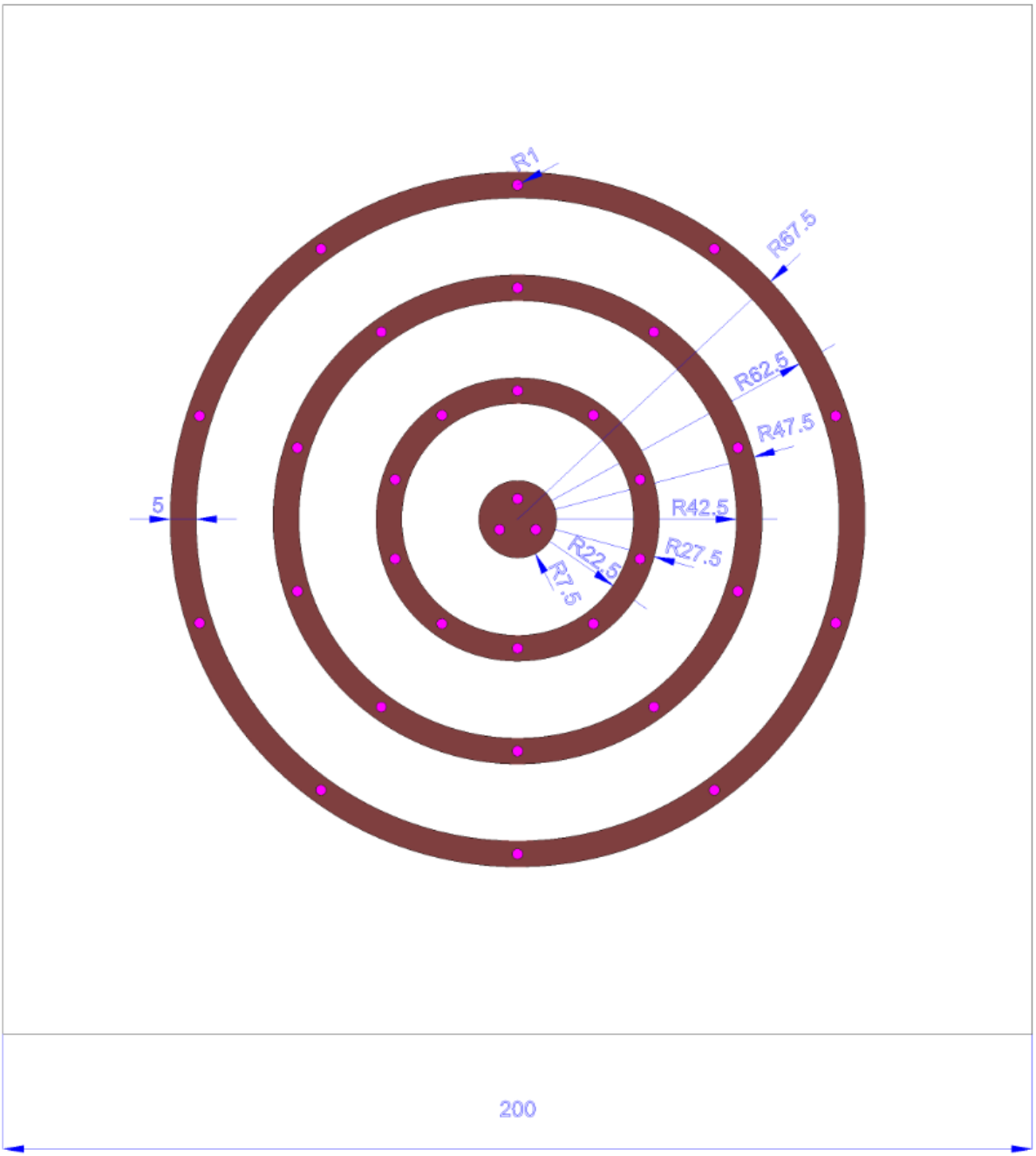

Figure 7.14 - Top layer of the valves vacuum system. In brown, the air grooves, with 5 mm thickness. The grooves are 20 mm apart, starting 7.5 mm from the centre.

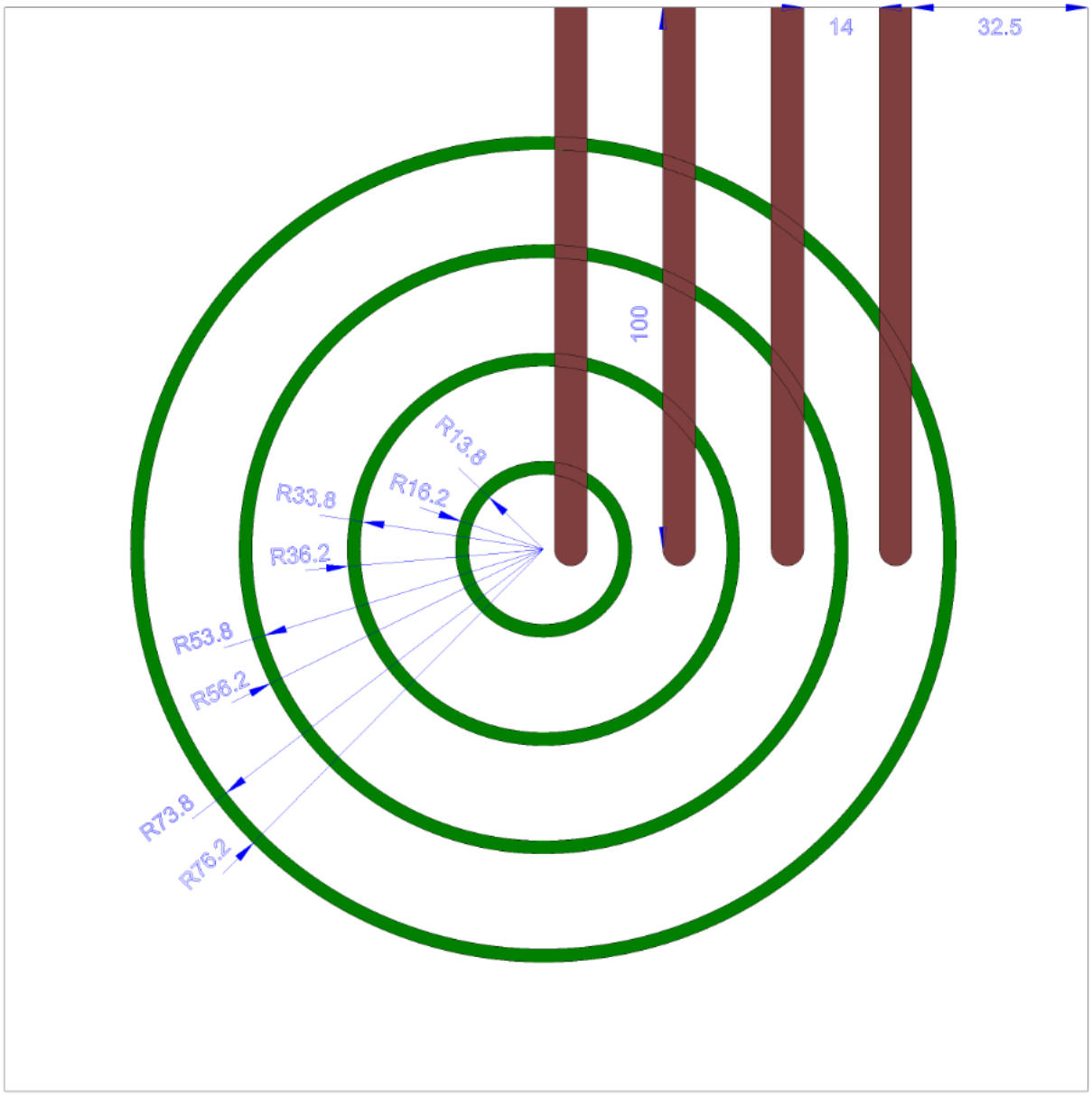

Figure 7.15 - Bottom layer of the valves vacuum system. In brown are the air grooves, starting 32 mm from the side, 14 mm apart, 100 mm depp. In dark green, the O-ring grooves, as described in the side figure, 20 mm apart.

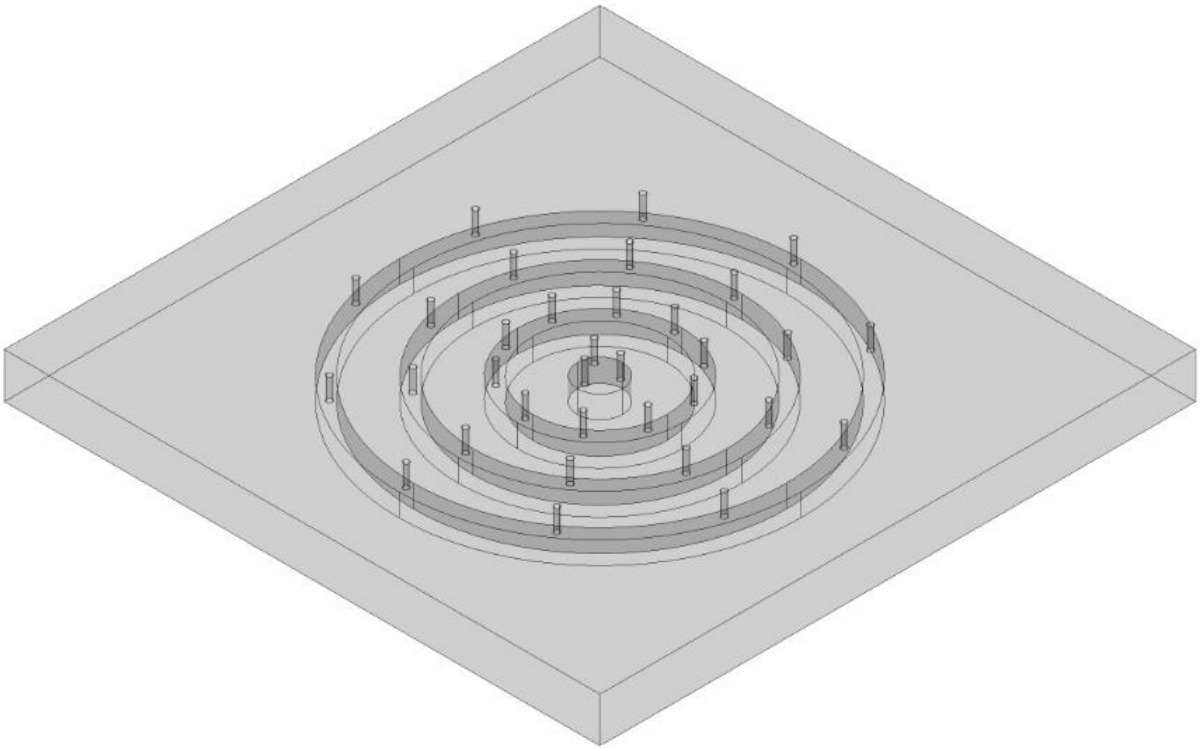

Figure 7.16 - 3D version of the top layer of the valves vacuum system.

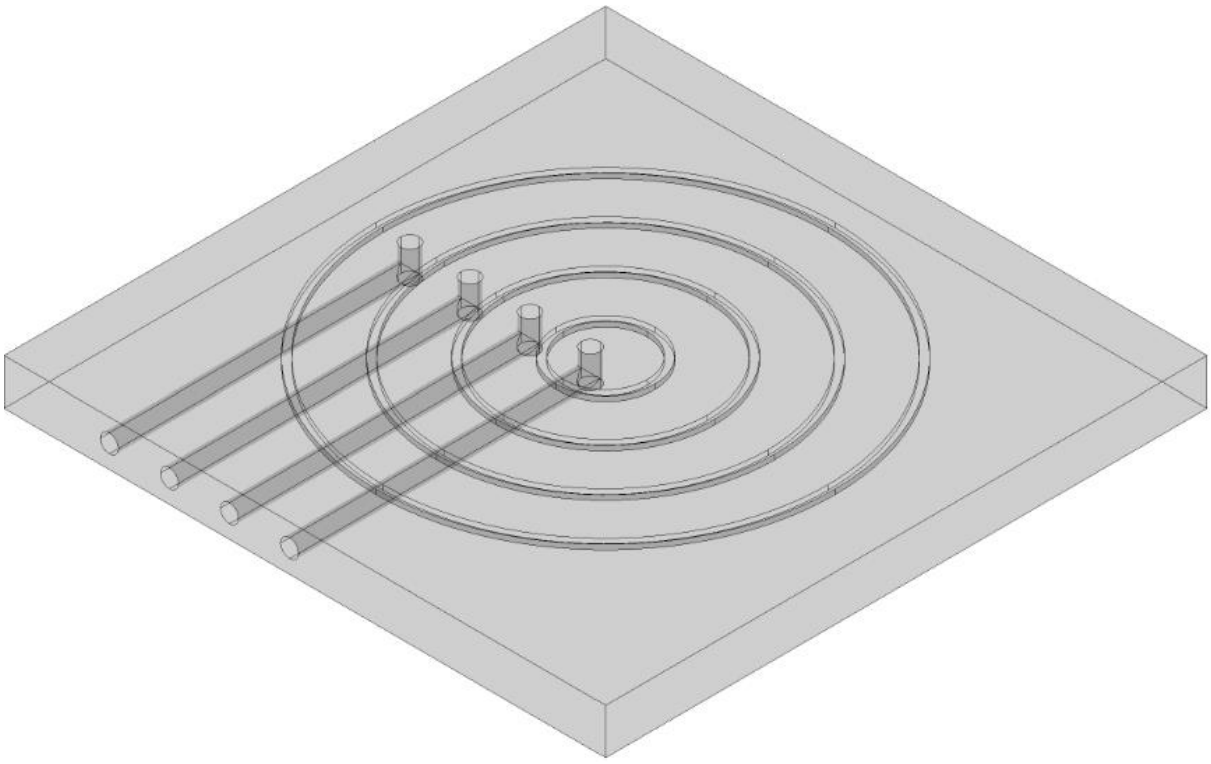

Figure 7.17 - 3D version of the bottom layer of the valves vacuum system.

7.4. Annex D – Piston system

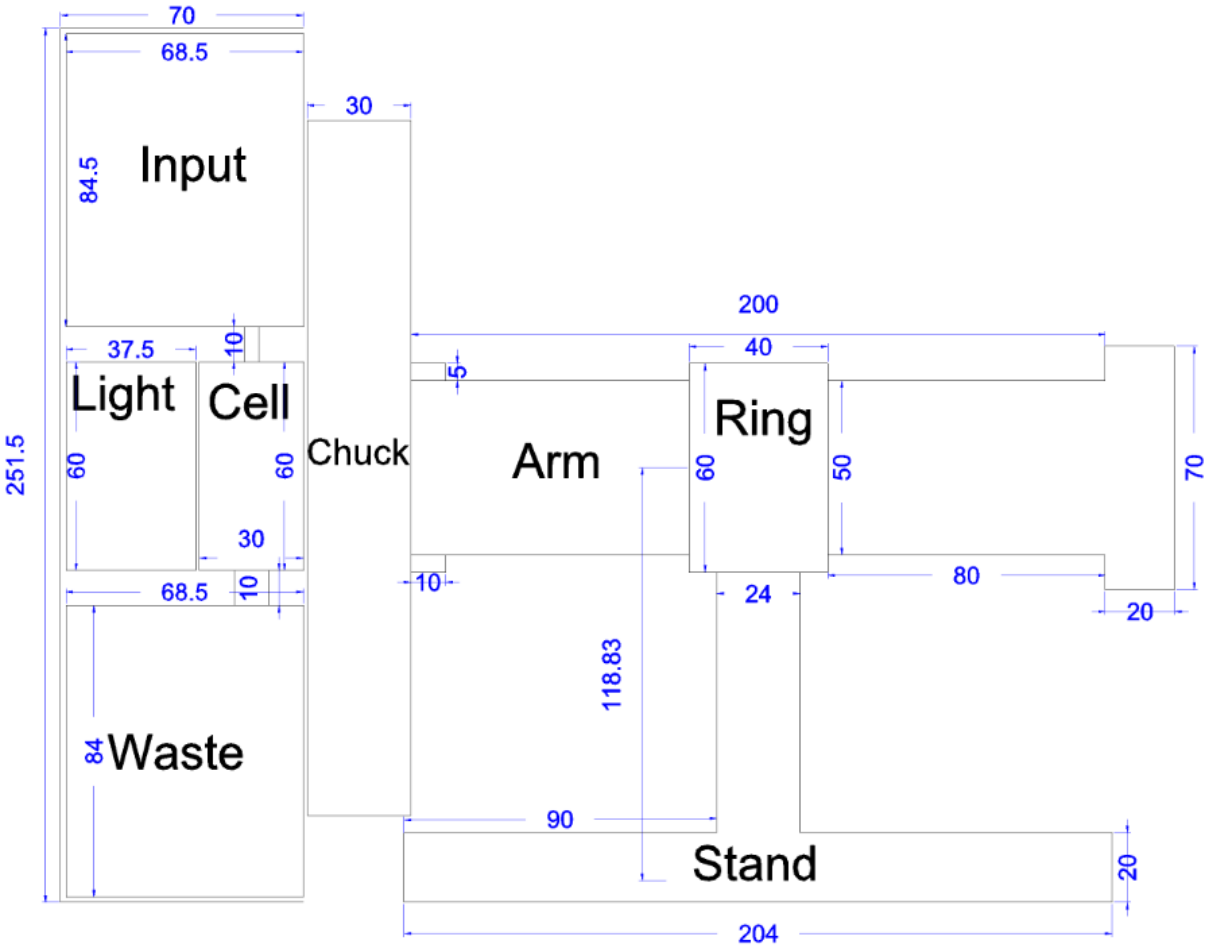

Figure 7.18 - Piston system with chuck and ECV system. In the left, the necessary parts for the ECV system, inside a cell chamber. An input reservoir, filled with electrolyte, on the top, connected to the electrochemical cell by a valve. Bellow the cell, a waste reservoir for the extraction of the electrolyte, also connected by a valve. To the left of the cell, the lighting system, needed to etch the n-type wafers. In the right, the piston system with the vacuum chuck attached. Left of the chuck, an shaft, which moves forward and backwards. In the shaft, next to the chuck, a spring pushes the chuck against the O-ring in the cell. In the middle of the shaft, a ring, with a rubber ring inside to prevent movement of the shaft during the measurements. Beneath, a stand places the middle of the chuck at the correct height.

7.5. Annex E – Cell chamber

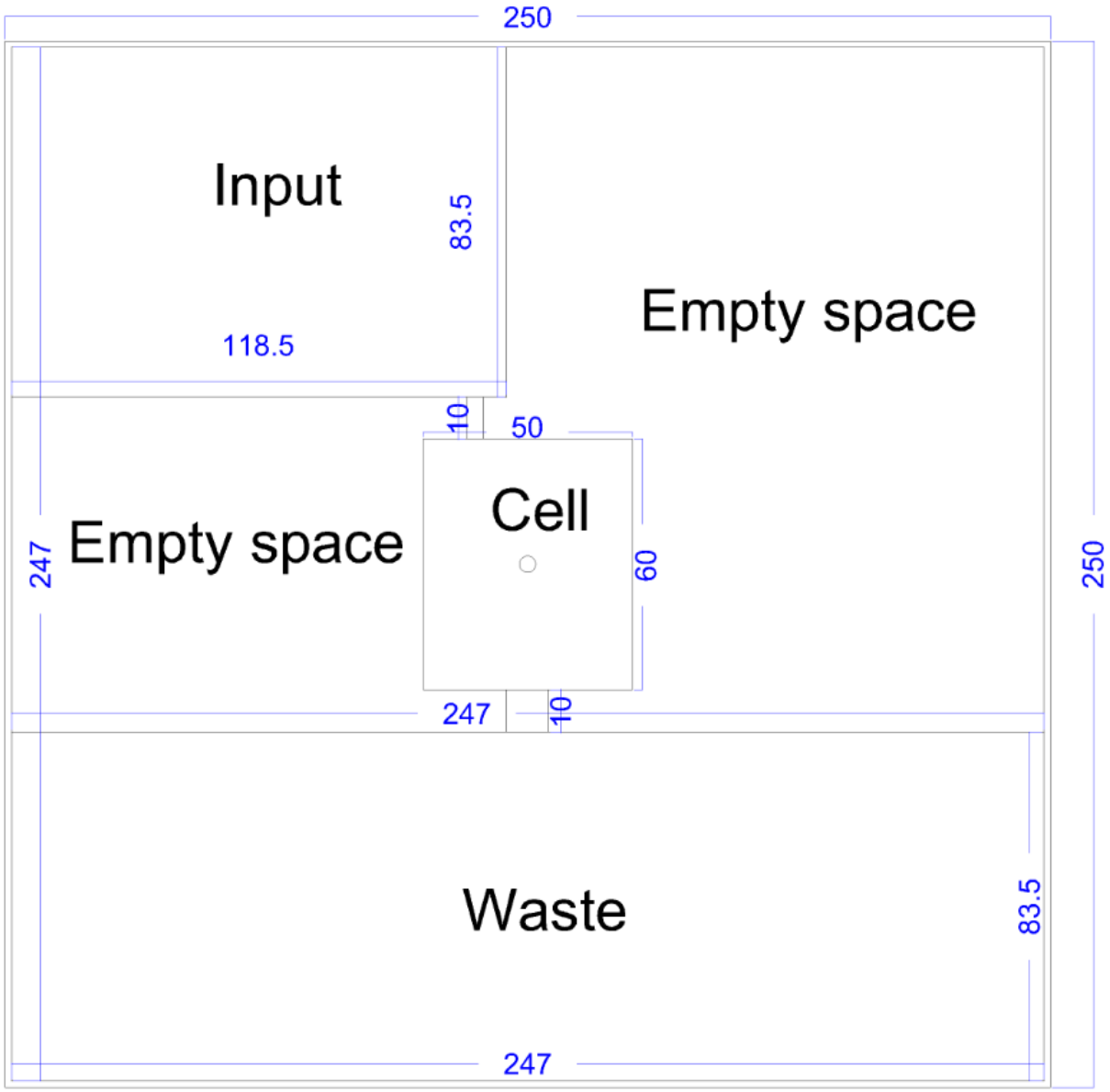

Figure 7.19 - The cell chamber. It has the electrochemical cell in the middle. On the top left, an input reservoir. Bellow the cell, a waste reservoir for the used electrolyte.